PUB 93-92

Tau Polarization from Angular Correlations [1]

Ricard Alemany Pantebre

Universitat Autònoma de Barcelona

Institut de Física d'Altes Energies

Edifici C E-08193 Bellaterra (Barcelona) Spain

May 1993

[1] Ph.D. Dissertation

N'Enrique Fernàndez Sànchez, Catedràtic de Física de la Universitat Autònoma de Barcelona,

CERTIFICA : Que la present memòria, que porta per títol *"Tau polarization from angular correlations "*, ha estat realitzada sota la seva direcció per en Ricard Alemany Pantebre i que constitueix la seva Tesi per a optar al Grau de Doctor en Ciències, Secció Física, per la Universitat Autònoma de Barcelona.

Enrique Fernàndez Sànchez

Bellaterra, 28 de Maig de 1993.

On Sunday at 12:30

Topant de cap en una i altra soca,
avançant d'esma pel camí de l'aigua,
se'n ve la vaca tota sola. És cega.
D'un cop de roc llançat amb massa traça,
el vailet va buidar-li un ull, i en l'altre
se li ha posat un tel: la vaca és cega.
Ve a abeurar-se a la font com ans solia,
més no amb el ferm posat d'altres vegades
ni amb ses companyes, no: ve tota sola.
Ses companyes, pels cingles, per les comes,
pel silenci dels prats i en la ribera,
fan dringar l'esquellot, mentres pasturen
l'herba fresca a l'atzar... Ella cauria.
Topa de morro en l'esmolada pica
i recula afrontada... Però torna,
i baixa el cap a l'aigua, i beu calmosa.
Beu poc, sens gaire set. Després aixeca
al cel, enorme, l'embanyada testa
amb un gran gesto tràgic; parpelleja
damunt les mortes nines, i se'n torna
orfe de llum sota del sol que crema,
vacil·lant pels camins inoblidables
brandant llanguidament la llarga cua.

Joan Maragall, 1893

Abstract

A new method to measure the electron and tau neutral current couplings from the acollinearity distribution of the tau pair decay products in $Z^0 \to \tau^+\tau^-$ events is presented. The extraction of the couplings from different sets of observables of interest is analyzed and discussed for the 11.2 pb^{-1} of data collected in 1990 and 1991 with the ALEPH detector at the Z^0 resonance. From the measurement of the acollinearity distribution of the cross section and from the forward-backward asymmetry as a function of the acollinearity angle, the parameter $\mathcal{A} = 2g_V g_A/[g_V^2 + g_A^2]$ are extracted for electrons and taus. The values $\mathcal{A}_e = 0.130 \pm 0.063$ (stat) ± 0.002 (sys) and $\mathcal{A}_\tau = 0.162 \pm 0.052$ (stat) ± 0.014 (sys) are found to be consistent with the hypothesis of electron-tau universality. With this hypothesis, the value of $\mathcal{A}_{e-\tau} = 0.148 \pm 0.035$ (stat) ± 0.009 (sys) is found. The corresponding value of $\sin^2\theta_W^{\rm eff} = 0.2314 \pm 0.0046$ is obtained.

Resum

Un nou mètode és presentat per a mesurar els acoblaments dels electrons i taus en els corrents febles neutres a partir de les distribucions d'acol·linearitat de les desintegracions de parelles de taus en els successos $Z^0 \to \tau^+\tau^-$. L'extracció d'aquests acoblaments a partir de diferents observables que presenten interès és analitzada en els 11.2 pb^{-1} de dades recollides entre els anys 1990 i 1991 pel detector ALEPH a la ressonància del Z^0. A partir de la mesura de la distribució d'acol·linearitat de la secció eficaç i de la seva asimetria, el paràmetre $\mathcal{A} = 2g_V g_A/[g_V^2 + g_A^2]$ és obtingut per electrons i per taus. Els valors $\mathcal{A}_e = 0.130 \pm 0.063$ (estadístic) ± 0.002 (sistemàtic) i $\mathcal{A}_\tau = 0.162 \pm 0.052$ (estadístic) ± 0.014 (sistemàtic) han estat mesurats mostrant consistència pel que fa referència a la hipòtesi d'universalitat d'electró-tau. Amb aquesta hipòtesi, el valor de $\mathcal{A}_{e-\tau} = 0.148 \pm 0.035$ (estadístic) ± 0.009 (sistemàtic) és obtingut. El corresponent valor de $\sin^2\theta_W^{\mathrm{eff}} = 0.2314$ ± 0.0046 n'és derivat.

Acknowledgements

During the time this thesis was developed I had the opportunity to work with many people from several groups. I would like to express my gratitude to all of them.

First, I want to express my indebtedness to J. Gómez who introduced me to the acollinearity world. His many comments on the experimental side, sometimes in the middle of the cold winter in Thoiry, were of great value.

I wish to thank T. Pich for many useful discussions explaining the acollinearities from the theoretical point of view, and for guiding and encouraging me about the difficult points. I would also like to give special thanks to J. Bernabéu and N. Rius for the fruitful discussions we had about the theoretical part.

In the course of this analysis, I have benefited from many suggestions and valuable help from M. Delfino, to whom I manifest my gratitude. He always patiently heard my thoughts even late in the night, cheering me on.

This thesis has benefited from many sharp comments from T. Mattison. His help in critical moments has been precious. In addition, he has carefully read and corrected the first *supposedly English* versions of this thesis. I appreciate very much all of his efforts.

I would like to take this opportunity to express my thanks to P. Mató for many discussions in the on-line environment, specially concerning luminosity measurements; and for the enthusiastic encouragement I received from him and his family. I appreciate very much all he taught me.

Writing an ALEPH paper following all the liturgical steps, where different analyses and results have to be gathered together, has been a very interesting experience in learning a bit of the art of physics and politics. I want to thank the members of University of Wisconsin and the members of the Ecole Polytechnique involved in tau physics for many discussions and suggestions during my work, specially J. Conway, J. Harton, A. Rougé, M. Schmitt, and H. Videau.

My fellow colleagues and friends S. Adlung, F. Ariztizabal, P. Berlich, M. Chmeissani, P. Comas, M. Devant, I. Efthymiopoulos, V. Gaitan, C. Padilla, A. Pacheco,

A. Pascual, L. Passalacqua, F. Teubert and P. Zemp are also acknowledged for experimental discussions and their amity.

I want to thank M. Martínez for *radiative* discussions and R. Miquel, L. Mir and J. Perlas for their friendliness and help.

I am grateful to M. Cavalli-Sforza for useful discussions; he always showed a good disposition and interest whenever I bothered him.

For their friendship and the pleasant working atmosphere, I thank all the members of the Institut de Física d'Altes Energies in Barcelona. Most of the paperwork for this thesis and many other administrative matters have been very efficiently managed by C. Cárdenas whom I also thank.

I offer my heartfelt thanks to the Borau, Devant and Pardo families for the hospitality they offered me these years.

More than anyone else, I am specially indebted to my advisor E. Fernández, not only for accepting me as a member of the Institut and for trusting me with several responsibilities, but also for always finding time to answer my questions and to deal with the crucial parts of my work. His help and encouragement has been decisive in carrying this thesis through. I enormously appreciate all the time we spent working together. Despite his other responsibilities, he made great efforts advising me that are gratefully acknowledged.

Contents

1 Introduction **1**

2 Polarization in the Standard Model **3**

2.1 The Standard Model 3

2.2 Electroweak Mixing Angle 6

2.3 Polarization and Other Observables 8

2.4 The Process $e^-e^+ \to \tau^-\tau^+$ 10

2.5 Correlated Decay Distributions 16

2.5.1 Tau Decay 17

2.5.2 The Process $e^-e^+ \to \tau^-\tau^+ \to x_1^- x_2^+ + \ldots$ 19

2.5.3 Angular Correlations 22

2.5.4 Energy-Energy Correlations 24

3 The ALEPH Detector **29**

3.1 LEP Storage Ring 29

3.2 The ALEPH Detector 31

3.2.1 Tracking Detectors 33

3.2.2 Calorimeter Detectors 39

3.2.3 Luminosity Detectors 43

3.3 Trigger and Data Acquisition System 45

3.4 Event Reconstruction and Simulation 46

3.5 Charged Track Reconstruction 47

4 Selection of events **51**

4.1 Preselection 51

4.2 Particle Identification 54

4.3 Channel Classification 56

4.3.1 Electron Channel Classification 58

4.3.2 Muon Channel Classification 58

4.3.3 Pion Channel Classification 59

4.4 Semi-Inclusive Categories 60

4.5 Acollinearity Event Classification 61

5 Measurement of the Electron and Tau Couplings **67**

5.1 Observables Based on the Acollinearity 67

5.2 Corrections to the Data Samples 71

5.3 The Acollinearity Distribution and its Forward-Backward Asymmetry 73

5.3.1 Extracting $\mathcal{A}_\tau$ from $\frac{d\sigma}{d\varepsilon}$ 74

5.3.2 Extracting $\mathcal{A}_{e-\tau}$ from $A_{FB}(\varepsilon)$ 76

5.3.3 Extracting $\mathcal{A}_\tau$, $\mathcal{A}_e$ and $\mathcal{A}_{e-\tau}$ simultaneously from $\frac{d\sigma}{d\varepsilon}$ and $A_{FB}(\varepsilon)$ 80

5.3.4 The Forward and Backward Acollinearity Distributions . . . 82

6 Systematic Errors **87**

6.1 Selection and Acceptance 88

6.2 Background 94

6.2.1 Tau Background 94

6.2.2 Non-Tau Background 95

6.3 Tracking Uncertainties 101

6.4 Branching Ratios and Theoretical Uncertainties 103

6.5 Summary of Main Systematic Errors 104

7 Electroweak Parameter Results **107**

7.1 Including Single-Tau Method Results 107

7.1.1 Results from Single-Tau Method 107

7.1.2 Correlation between Single-Tau and Acollinearity Results . . 108

7.1.3 Combined Results 110

7.2 Electroweak Parameters 111

7.2.1 Electroweak Parameters from Acollinearity 111

7.2.2 Electroweak Parameters from Combined Results 112

8 Conclusions **117**

A Phase Space Integration in Q Functions **120**

B Covariance Matrix for the Forward-Backward Asymmetry **126**

List of Figures

2.1 Families in the Standard Model. 4
2.2 The $SU(2)$ representation of quarks and leptons. 5
2.3 Tree level diagrams that contribute to tau production from e^-e^+. . 10
2.4 Possible helicity state configurations for the process $e^+e^- \to \tau^+\tau^-$. . 11
2.5 Coordinate system in the laboratory frame. 13
2.6 Functions $Q_{ij}(\varepsilon)$ for the $\pi^-\pi^+$ decay channel. 24
2.7 Functions $Q_{ij}(\varepsilon)$ for the $e^-\mu^+$ decay channel. 25
2.8 Functions $Q_{ij}(\varepsilon)$ for the $e^-\rho^+$ decay channel. 26

3.1 Scheme of the LEP injectors and accelerators. 30
3.2 Overall view of the ALEPH detector. 32
3.3 ITC drift cells. 34
3.4 View of the TPC. 36
3.5 View of a TPC wire chamber. 38
3.6 View of the ECAL detector. 40
3.7 View of an ECAL layer. 42
3.8 View of the HCAL detector. 43

4.1 Typical tau event as seen in the ALEPH detector. 53
4.2 Acollinearity distributions for the selected events for inclusive pions and leptons. 62

4.3 Efficiencies as a function of the acollinearity angle for inclusive pions and leptons. 64

4.4 Backgrounds as a function of the acollinearity angle for inclusive pions and leptons. 65

4.5 Correlation between energy and acollinearity for the lepton sample. 66

5.1 F and G functions for inclusive pions. 68

5.2 F and G functions for inclusive leptons. 69

5.3 Resolution matrix G_{ij} applied for inclusive lepton sample. 73

5.4 Correction coefficients for inclusive pions and leptons as a function of the acollinearity. 74

5.5 Observed and corrected distributions integrated over the whole acceptance range for pions and leptons. 75

5.6 Result of the fit to the acollinearity distribution of the cross section. 77

5.7 Result of the fit to the forward-backward asymmetry as a function of the acollinearity. 78

5.8 Predicted forward-backward asymmetry as a function of the acollinearity for a $\pm$ 0.5 polarization for inclusive pions and leptons. 79

5.9 Observed and corrected distributions integrated over the forward and backward hemispheres for pions and leptons. 82

5.10 Result of the fit to the normalized forward and backward acollinearity distributions. 83

5.11 Comparison of the fitted values with two different set of observables. 86

6.1 Ratio of 1991 data and Monte Carlo neural network identification efficiency for kinematically identified electrons, muons and pions as a function of the acollinearity. 92

6.2 Ratio of the Monte Carlo and data efficiencies as a function of the polar angle for Bhabha electrons, muon pairs and pions. 93

6.3 Acollinearity distribution for identified pions with zero, one, two and more reconstructed photons. 94

6.4 Acollinearity distribution for identified leptons with zero, one, two and more reconstructed photons. 96

6.5 Acollinearity distribution for Monte Carlo and data of two-photon events. 97

6.6 Acollinearity distributions for Bhabha and dimuon events. 98

6.7 Acollinearity distributions of electrons identified as pions and muons identified as pions for Monte Carlo and data. 100

6.8 Projection of the difference of the azimuthal angles for muon pairs. 101

7.1 Contours of constant χ^2 for $g_V(M_Z^2)$ and $g_A(M_Z^2)$ from the tau polarization and the partial widths. 114

7.2 Results of ALEPH measurements of the weak mixing angle from asymmetries and tau polarization. 115

A.1 Allowed angular region for a given acollinearity angle. 123

List of Tables

2.1 Isospin and hypercharge for quarks and leptons. 5

2.2 Contributions to the functions appearing in the differential cross section. 14

3.1 Main LEP parameters. 31

4.1 Efficiency of the neural network particle identification for Monte Carlo lepton pair events. 55

4.2 Performance of channel classification and background rejection. . . 60

4.3 Integrated luminosities per year and mean energy for data sets. . . 63

4.4 Summary of the efficiencies and backgrounds for the selected acollinearity sample. 63

5.1 Polarisation parameters extracted from the acollinearity distribution of the cross section. 76

5.2 Polarisation parameters extracted from the forward-backward asymmetry as a function of the acollinearity. 76

5.3 Polarisation parameters extracted from the acollinearity distribution of the cross section and its forward backward asymmetry. 81

5.4 Measured polarization as a function of polar angle, for the acollinearity method. 84

5.5 Polarization parameters extracted from polar angle dependence of the acollinearity distribution. 85

6.1 Systematic errors on polarization from the particle identification in $d\sigma/d\varepsilon$. 91

6.2 Systematic errors on polarization from the particle identification in $A_{FB}(\varepsilon)$. 91

6.3 Number of events with zero, one, two and more reconstructed photons for the inclusive pions and leptons for Monte Carlo and data. . 95

6.4 Systematic errors on polarization from background sources. 99

6.5 Systematic errors on polarization from tracking. 102

6.6 Systematic errors on polarization from the theoretical uncertainties. 103

6.7 Summary of systematic errors on polarization from the acollinearity method. 105

6.8 Summary of systematic errors on polarization from the forward-backward asymmetry as a function of the acollinearity. 106

6.9 Final systematic errors on polarization parameters from combined analysis. 106

7.1 Corrected polarization parameters extracted from polar angle fit single-tau methods with their statistical and systematic errors. 108

7.2 Summary of systematic errors on P_τ for each decay channel, for the single-tau method. 108

7.3 Polarization parameters extracted from polar angle dependence, combining the single-tau method results with that of the acollinearity method. 111

A.1 Limits of integration. 124

Chapter 1

Introduction

One of the main physics goals of the experiments at LEP is to perform high precision tests of the Standard Model; this implies the careful determination of the free parameters of the theory and the search for possible indications of departures from it.

One of those important parameters in the Standard Model is the weak mixing angle. Several methods and techniques have been developed recently to produce a measurement of this quantity at LEP. In fact, the LEP experiments have already achieved an impressive level of precision for the Z^0 mass and width [1], while the precise determination of other quantities needs more effort.

A well known method which is very sensitive to measure the weak mixing angle is the tau polarization [2]. In the Standard Model, the parity violations in the weak interactions lead to the fact that collisions of unpolarized electron beams at LEP produce polarized taus. The inequality of the vector and axial vector coupling constants of the electron leads to a polarization of the Z^0, measured with respect to the axis defined by the incoming fermions. The subsequent Z^0 decay yields a polarized pair of fermions, in this case tau leptons. Since they decay promptly, and their decay depends on their spin, the decay products can be used as polarization analyzers.

The tau polarization has been usually measured from the energy spectra of the tau decay products. Due to helicity conservation, both taus have opposite helicities in an event, so they are completely correlated. However, when the tau decay products of a tau pair event are analyzed independently, the correlation

information is lost. In this thesis a new method has been developed to measure the tau polarization from correlated angular distributions, through the acollinearity angle of the event.

The interest of the method proposed here lies, first, in the possibility of reducing the overall error in the measurement of the tau polarization, since the angular correlations provide additional information of this quantity which can be combined with other results, and secondly, in the fact that the systematics associated with angular measurements should be largely independent from those associated with the measurement of the energy distributions of the tau decay products, which are used at present. Futhermore, the most recent measurements on the tau polarization [3] using the conventional method reveals that the most sensitive channels have reached the systematic error limit.

The outline of this thesis is as follows. Chapter 2 is dedicated to describe the structure of the Standard Model as a framework to present the theoretical development on which the correlated angular distributions of the tau decay products is based. Chapter 3 is devoted to a brief description of the LEP accelerator and the ALEPH detector, giving more emphasis to the relevant subdetectors on which the angular measurements rely. An explanation of the ALEPH reconstruction and off-line software is also added.

The method used to select the tau events and identify the decay channels is explained in chapter 4. The efficiencies and backgrounds are discussed as well. In chapter 5, the observed acollinearity distributions for the samples considered are presented, and the procedure to fit the data with the theoretical prediction at tree level is explained. The measurements of the acollinearity distributions from different sets of observables are discussed in detail. The study of the main sources of systematic error in those measurements is described in chapter 6.

The results obtained from the ALEPH collaboration measuring the tau polarization using the energy spectra are presented, and its combination with the acollinearity method is given in chapter 7. Finally, in chapter 8, the conclusions of this work are presented.

Chapter 2

Polarization in the Standard Model

2.1 The Standard Model

The Glashow-Weinberg-Salam theory is a non-abelian gauge theory with spontaneous symmetry breaking in which the vector bosons acquire masses by mean of the Higgs mechanism. The Glashow-Weinberg-Salam theory is gauge invariant under the $SU(2)_T \otimes U(1)_Y$ group of weak isospin T and hypercharge Y. The lagrangian for this theory gives masses to the fermions and to the gauge bosons by the introduction of a new scalar field, the Higgs field, with a non vanishing vacuum expectation value. The strong interactions are described by including a new gauge field theory called Quantum Chromodynamics, which is invariant under the $SU(3)_C$ group of color.

The Glashow-Weinberg-Salam model together with the Quantum Chromodynamics theory are known as the Standard Model, which so far has indeed met with a good degree of success in describing most of the experimental results in high energy physics.

The Standard Model contains the three following types of fields:

- Fermion matter fields,
- Gauge fields, and
- Higgs scalar fields.

Fermion fields

The basic unit of the fermion matter fields is a family, that contains quarks and leptons consisting of two-component complex spinor fields. The quarks are massive fermions with fractional charge and three possible colors. The leptons have no color. The electron, muon and tau are massive particles with unit charge. The corresponding neutrinos are very light (or massless) and are neutral. Both quarks and leptons have their corresponding antiparticles, that have the same masses but opposite quantum numbers.

Up to now, all the known quarks and leptons are grouped in three families, as figure 2.1 shows. The first family is composed by the electron and its neutrino, and the up and down quarks. The second is composed by the muon, its neutrino and the charm and strange quarks, whereas the third corresponds to the tau and its neutrino, with the bottom and top quarks.

The $SU(2)$ representation of quarks and leptons is given for the first family in figure 2.2. Left handed fermions come in as $SU(2)_T$ isospin doublets and right handed fermions as isospin singlets. In addition, quarks transform as $SU(3)_C$ color triplets, whereas leptons as color singlets.

Assigning the quantum numbers $\vec{T}$ and Y, the weak isospin and the weak hypercharge respectively, defines the fermion transformation properties under the gauge group considered. The assignment of those quantum numbers is shown in table 2.1.

FAMILIES

$$\begin{pmatrix} \nu_e \\ e \end{pmatrix} \quad \begin{pmatrix} \nu_\mu \\ \mu \end{pmatrix} \quad \begin{pmatrix} \nu_\tau \\ \tau \end{pmatrix}$$

$$\begin{pmatrix} u \\ d \end{pmatrix} \quad \begin{pmatrix} d \\ s \end{pmatrix} \quad \begin{pmatrix} b \\ t \end{pmatrix}$$

Figure 2.1: *Families in the Standard Model.*

particle	T	T_3	Y
$(\nu_e,\ \nu_\mu,\ \nu_\tau)_L$	1/2	1/2	-1/2
$(e,\ \mu,\ \tau)_L$	1/2	-1/2	-1/2
$(e,\ \mu,\ \tau)_R$	0	0	-1
$(u,\ c,\ t)_L$	1/2	1/2	1/6
$(d,\ s,\ b)_L$	1/2	-1/2	1/6
$(u,\ c,\ t)_R$	0	0	2/3
$(d,\ s,\ b)_R$	0	0	-1/3

Table 2.1: *Isospin and hypercharge for quarks and leptons.*

Gauge fields

The gauge fields are the mediators of the interactions between quarks and leptons. The massive Z^0 and $W^{\pm}$ bosons mediate the weak interaction. The electromagnetic interaction is mediated by one massless and chargeless boson, the photon. Finally, there are eight massless boson gluons which are associated

FAMILY COMPONENTS

$$\begin{pmatrix} \nu_{eL} \\ e_L \end{pmatrix} \quad \begin{pmatrix} u_L \\ d_L \end{pmatrix}_b \quad \begin{pmatrix} u_L \\ d_L \end{pmatrix}_g \quad \begin{pmatrix} u_L \\ d_L \end{pmatrix}_r$$

$$\begin{pmatrix} e_R \end{pmatrix} \quad \begin{pmatrix} u_R \end{pmatrix}_b \quad \begin{pmatrix} u_R \end{pmatrix}_g \quad \begin{pmatrix} u_R \end{pmatrix}_r$$

$$\begin{pmatrix} d_R \end{pmatrix}_b \quad \begin{pmatrix} d_R \end{pmatrix}_g \quad \begin{pmatrix} d_R \end{pmatrix}_r$$

Figure 2.2: *The $SU(2)$ representation of leptons, and $SU(2)$ and $SU(3)$ representation of quarks. The labels L and R denotes left-handed and right-handed states. The labels b, g, r stands for the blue, green and red colors, respectively.*

with the strong interactions.

Higgs fields

The electroweak gauge group $SU(2)_T \otimes U(1)_Y$ can be represented by an $SU(2)_T$ triplet of vector gauge fields $\vec{W}_\mu$ with coupling constant g, and a $U(1)_Y$ scalar gauge field B_μ with coupling constant g'. In principle, if the gauge symmetry were unbroken, the theory would yield massless bosons. In order to provide massive gauge fields, in the Standard Model it is introduced a doublet of complex scalar fields (the Higgs fields), that with their non-zero vacuum expectation values break the gauge symmetry spontaneously, and thus provide masses to the fermions and to three gauge fields (or a combination of three of them).

2.2 Electroweak Mixing Angle

The weak mass eigenstates are related to the gauge fields $\vec{W}_\mu$ and B_μ by

$$W_\mu^\pm = \frac{1}{\sqrt{2}}(W_\mu^1 \mp iW_\mu^2) \tag{2.1}$$

$$Z_\mu = -\cos\theta_W W_\mu^3 + \sin\theta_W B_\mu \tag{2.2}$$

$$A_\mu = \sin\theta_W W_\mu^3 + \cos\theta_W B_\mu, \tag{2.3}$$

where θ_W is called the Weinberg angle or weak angle given by

$$\tan\theta_W \equiv \frac{g'}{g}\,. \tag{2.4}$$

The bosons A_μ and Z_μ are electrically neutral because the bosons W_μ^3 and B_μ connect fermions with themselves, so they do not carry any electrical charge. In addition, the boson A_μ is a massless field with coupling constant e, the electron charge, which is related to the couplings g and g' according to

$$e = \frac{gg'}{\sqrt{g'^2 + g^2}} = g\sin\theta_W\,. \tag{2.5}$$

The massive gauge fields Z_μ and $W_\mu^\pm$ are responsible for the neutral and charged current of the weak interactions, and their masses are related to the weak angle in

lowest order by

$$M_W = M_Z \cos\theta_W \ . \tag{2.6}$$

It is tempting to speculate, because of the presence of several parameters and the pattern of the fermion masses, that a more highly unified theory can be formulated. Presently, for the Glashow-Weinberg-Salam theory the number of free parameters that need to be introduced in the gauge boson and scalar sector in the most general expression of the lagrangian are

$$e,\ \theta_W,\ G_F,\ M_H\ ,$$

or combinations of them.

Up to now, the electron charge e and the Fermi constant G_F are measured with great precision. The Higgs mass M_H is unknown, although some theoretical and some phenomenological bounds exist. Finally, the weak mixing angle θ_W is already measured by several experiments, and its precision is considerably improved in the LEP experiments. The next sections will focus on describing the procedure used to perform a measurement of this quantity, through the tau leptons and their decays.

The most relevant terms of the lagrangian to carry on this study within the Standard Model are the terms describing the coupling of the fermion fields to vector bosons after the spontaneous symmetry breaking, given by

$$\begin{aligned}\mathcal{L} = \ & - \frac{g}{2\sqrt{2}}\sum_f \overline{\psi}_f\gamma^\mu(1-\gamma^5)(T^+W_\mu^+ + T^-W_\mu^-)\psi_f \\ & - \frac{g}{2\cos\theta_W}\sum_f \overline{\psi}_f\gamma^\mu(v_f - a_f\gamma^5)\psi_f Z_\mu \\ & - e\sum_f Q_f\overline{\psi}_f\gamma^\mu\psi_f A_\mu\ ,\end{aligned} \tag{2.7}$$

where ψ_f and $\overline{\psi}_f$ are the quark or lepton fermionic fields, and T^+ and T^- are two of the weak isospin generators of the group $SU(2)$, which raise and lower the third component of T_3 by one unit. This implies an increment of the same sign in the charge Q, because of the relation

$$Q = T_3 + Y\ . \tag{2.8}$$

The first term of this electroweak lagrangian corresponds to the charged current weak interactions coupled by $W^{\pm}$ gauge bosons. The second term corresponds to the weak neutral current interaction coupled by the neutral gauge boson. The last term corresponds to the electromagnetic interaction mediated by a photon. Other terms in the lagrangian such as those responsible for the couplings between the Higgs and either the leptons, gauge bosons or the Higgs itself are needed in the calculation of radiative corrections but are not explicitly written in equation 2.7.

The parameters v_f and a_f are the vector and axial couplings of the neutral boson Z^0 to the fermion f, that in principle can be measured separately. These are the parameters that will concern us in this thesis. In the Standard Model, the v_f and a_f couplings are given by

$$v_f = T_3^f - 2Q_f \sin^2\theta_W \tag{2.9}$$

$$a_f = T_3^f \,, \tag{2.10}$$

where Q_f and T_3^f are the charge and the third isospin component of the fermion f, as given in table 2.1.

2.3 Polarization and Other Observables

At LEP the most precise determination of $\sin^2\theta_W$ is provided by several asymmetries to be determined on the Z^0 peak [4, 5]. These include the forward-backward charge asymmetry, the final state polarization, the forward-backward polarization asymmetry and the left-right cross-section asymmetry for a longitudinally polarized beam.

The forward-backward charge asymmetry has been measured for quarks and leptons with good accuracy at LEP experiments. In particular for muons and taus, this asymmetry is extracted from a fit to the angular distribution given by

$$\frac{d\sigma}{d\cos\theta} = C\,(1 + \cos^2\theta + \frac{8}{3}A_{FB}\cos\theta)\,, \tag{2.11}$$

where C is a normalization constant, θ is the scattering angle between the incoming e^- and the negative outgoing fermion in the centre of mass, and A_{FB} is the forward-backward charge asymmetry, which will be discussed further in the next

section. The angular distribution is more complex for electrons due to the t-channel contributions.

The final state polarization and the forward-backward polarization asymmetry are experimentally accessible in tau pair production, i.e. $e^+e^- \to \tau^-\tau^+$, because tau particles promptly decay, unlike muons or electrons. In particular, the tau particles decay via weak charged currents where parity is maximally violated, therefore the kinematical distributions of the decay products depends strongly on the spin orientation of the tau. The use of tau decays as polarization analyzers of its spin state has been considered extensively by several authors in the literature [6, 7].

The polarization of the tau, for instance, can be measured from the energy distribution of a given decay product. The sensitivity of the decay channel to the longitudinal tau polarization depends on the spin of the product whose spectrum is measured. The most sensitive decay is the pion channel $\tau \to \pi\nu_\tau$, because the pion is a pseudo-scalar. Consider for the sake of simplicity, $\tau^- \to \pi^-\nu_\tau$, in the case where the angle between the tau line of flight and the pion is zero. Since this decay is a two body decay, in the tau rest frame the ν_τ and the π^- are going out back to back, and the orbital angular momentum along the direction of the ν_τ is zero. Assuming that the tau decays via the V − A interaction, then as the ν_τ has negative helicity, it prefers to be emitted opposite to the direction of the spin of the τ^- to conserve the total angular momentum. Therefore, the π^- prefers to be emitted in the same direction of the spin of the τ^-. So, for a tau with positive (negative) helicity the resulting pion tend to be more (less) energetic.

For the spin one decay products such as in the ρ and a_1 channels, more possibilities can occur, and thus in principle those channels are less sensitive. However, the loss of sensitivity with respect to the $\tau \to \pi\nu_\tau$ channel can partially be recovered [8, 9, 10] by measuring the helicity of these systems from the subsequent $\rho \to \pi\pi$ and $a_1 \to \pi\pi\pi$ decays. In the leptonic channels $\tau \to e\nu_e\nu_\tau$ and $\tau \to \mu\nu_\mu\nu_\tau$ the sensitivity is still worse because the spin can be distributed to all three bodies.

In this thesis our main interest is to extract the tau polarization from angular correlations of the decay products of both taus produced at the Z^0 peak at LEP. The potential of the correlated distributions as analyzers of the tau properties covers an ample range, which includes not only information on the spin state of a single tau but also on the spin correlations between both parent taus [11, 12, 13] and on the

parameters of the charged-current tau decay processes [14].

In terms of the acollinearity angle between the two decay products, the acollinearity distribution of both the cross-section and the forward-backward asymmetry are presented as the observables of interest, although other observables as a function of the acollinearity are also discussed. Assuming a Standard Model description of the tau decay, these measurable quantities depend only on the tau and electron couplings.

2.4 The Process $e^-e^+ \to \tau^-\tau^+$

In perturbation theory to the lowest order in the Standard Model, the amplitude of the process

$$e^-(k_1) + e^+(k_2) \to \tau^-(p_1, s_1) + \tau^+(p_2, s_2)$$

where k_i and s_i (i=1,2) are the four-momenta and four-spin vectors respectively, is given by the sum of the contributions associated with γ- and Z^0-exchanges. Both diagrams are represented in figure 2.3. The dominant electroweak radiative corrections around the Z^0 resonance can be included in the improved Born approximation [15].

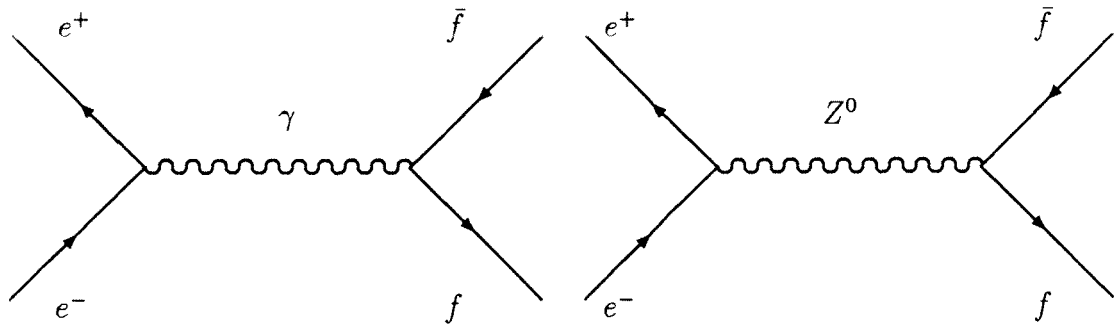

Figure 2.3: *Tree level diagrams that contribute to tau production from* e^-e^+.

As can be inferred from the Feynman rules associated to the lagrangian of equation 2.7, the amplitude for the photon exchange, T_0^γ, and for the Z^0 exchange, T_0^Z,

are given by

$$T_0^\gamma = i\, e^2\, \frac{Q_e Q_f}{s}\, \overline{v}(k_2)\gamma_\mu u(k_1)\, \overline{u}(p_1)\gamma^\mu v(p_2) \tag{2.12}$$

$$T_0^Z = i\, \frac{e^2}{4 \sin\theta_W^2 \cos\theta_W^2}\, \chi_0(s)\ \times \tag{2.13}$$
$$\overline{v}(k_2)\gamma_\mu(v_e - a_e\gamma_5)u(k_1)\, \overline{u}(p_1)\gamma^\mu(v_f - a_f\gamma_5)v(p_2)\ ,$$

where s = $(k_1 + k_2)^2$, and, up to small non-universal vertex corrections, the couplings of the Z^0 boson with the leptons v_l and a_l ($l = e,\ f$) are already defined in expressions 2.9 and 2.10. The propagator of the Z^0 boson, $\chi_0(s)$, in the Breit-Wigner approximation may be written

$$\chi_0(s) = \frac{1}{s - M_Z^2 + iM_Z\Gamma_Z^0}\ , \tag{2.14}$$

where Γ_Z^0 is given by

$$\Gamma_Z^0 = \sum_f N_C^f\, \frac{\alpha}{3}\, \frac{M_Z}{4\sin^2\theta_W^2 \cos^2\theta_W^2}(v_f^2 + a_f^2)\ , \tag{2.15}$$

and N_C^f is the color factor, with value 1 for leptons and 3 for quarks.

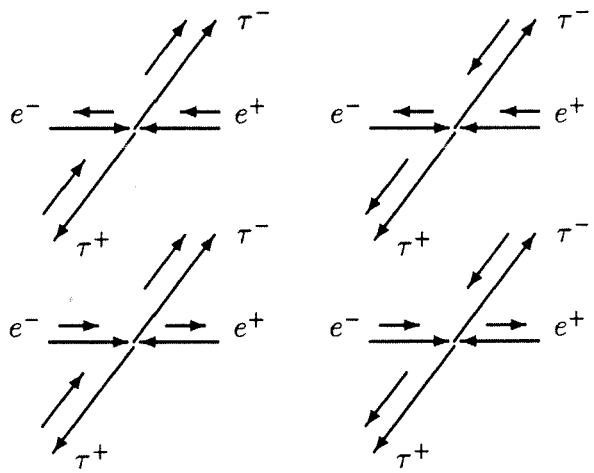

Figure 2.4: *Possible helicity state configurations for the process* $e^+e^- \to \tau^+\tau^-$.

It may be pointed out that according to the structure of the Standard Model the contributions of the amplitudes 2.12 and 2.13 in terms of the left and right

handed states, when the fermion energies are large with respect to its masses, can be formulated by mean of the following projectors

$$u_L = \frac{(1-\gamma_5)}{2}u \quad , \quad u_R = \frac{(1+\gamma_5)}{2}u \; , \tag{2.16}$$

where γ_5 is the Dirac chirality operator. These operators project out the helicity of a spinor.

It can be shown that when ignoring corrections $\mathcal{O}(m_\tau^2/M_Z^2)$, that is, in the limit of high energy, the helicity is conserved in weak current interactions, and therefore both fermions will be in opposite helicity states. In the case of annihilation of an electron and a positron, only the $e_R^+e_L^-$ and $e_L^+e_R^-$ combinations, where both states have opposite helicities, will be found. The same argument is also valid for the final fermion states. In other words, in the centre of mass, the scattering proceeds from a initial state with angular momentum $\pm$ 1 along the coming e^- direction to a final state again with $\pm$ 1 angular momentum along the outgoing τ^- direction. The four possible helicity state configurations are shown in figure 2.4.

In order to compute the differential cross section for $\tau^+\tau^-$ production with the spin of τ^- in an arbitrary direction s_1^* and with the spin of τ^+ in an arbitrary direction s_2^*, where s_1^* and s_2^* are unitary vectors of four components defined in the rest frame of the τ^- and the τ^+, respectively, the coordinate system of figure 2.5 is employed.

Using this reference system, where in the laboratory system the z-axis is along the τ^--direction whereas the y-axis is defined by $\vec{p_1} \times \vec{k_1}$, the four-vectors of the process $e^+e^- \to \tau^+\tau^-$ take the following form

$$k_1^\mu = k(1, \sin\theta, 0, \cos\theta) \tag{2.17}$$

$$k_2^\mu = k(1, -\sin\theta, 0, -\cos\theta) \tag{2.18}$$

$$p_1^\mu = (E, 0, 0, p) \tag{2.19}$$

$$p_2^\mu = (E, 0, 0, -p) \tag{2.20}$$

$$s_1^\mu = (\beta\gamma s_{1z}^*, s_{1x}^*, s_{1y}^*, \gamma s_{1z}^*) \tag{2.21}$$

$$s_2^\mu = (-\beta\gamma s_{2z}^*, s_{2x}^*, s_{2y}^*, \gamma s_{2z}^*) \; , \tag{2.22}$$

where the components of s_1^* and s_2^* are at the tau rest frame of the τ^- and the τ^+, and where the mass of the electron has been neglected.

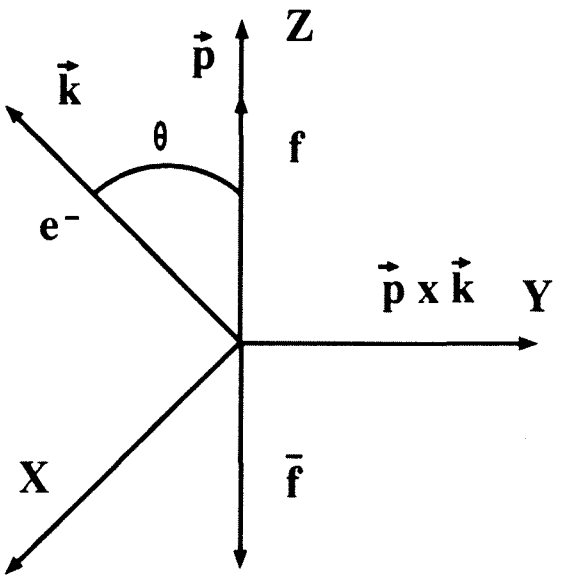

Figure 2.5: *Coordinate system in the laboratory frame.*

From the amplitudes 2.12 and 2.13, the differential cross section for the $\tau^-\tau^+$ production with polarization vectors s_1 and s_2, respectively, may be written neglecting the electron mass as

$$\begin{aligned}\frac{d\sigma}{d\Omega}(s_1,s_2) &= \frac{1}{16s}\{(1+s_{1z}^*s_{2z}^*)[F_0(s)(1+\cos^2\theta)+F_1(s)2\cos\theta] \\ &- (s_{1z}^*+s_{2z}^*)[G_0(s)(1+\cos^2\theta)+G_1(s)2\cos\theta] \\ &+ [(s_{1y}^*s_{2y}^*-s_{1x}^*s_{2x}^*)F_2(s)+(s_{1y}^*s_{2x}^*+s_{1x}^*s_{2y}^*)G_2(s)]\sin^2\theta\}\ ,\end{aligned} \tag{2.23}$$

where s^* designates the polarization vector in the rest frame of the tau [1].

The functions $F_i(s)$ $(i = 0,1,2)$ are associated with parity conserving terms, whereas $G_i(s)$ $(i = 0,1,2)$ correspond to parity violating observables. The functions $F_i(s)$ and $G_i(s)$ contain all the dynamic information of the theory, so they only depend on the coupling constants and on the propagator of the Z^0 boson. They are

[1] s in the argument of F_i and G_i functions is the squared center of mass energy.

	γ	γZ^0	Z^0
$F_0(s)$	$\alpha^2(M_Z^2)$	$2\alpha(M_Z^2)v_e v_\tau \mathrm{Re}H(s)$	$C_0\|H(s)\|^2$
$F_1(s)$		$2\alpha(M_Z^2)a_e a_\tau \mathrm{Re}H(s)$	$C_1\|H(s)\|^2$
$F_2(s)$	$-\alpha^2(M_Z^2)$	$-2\alpha(M_Z^2)v_e v_\tau \mathrm{Re}H(s)$	$C_2\|H(s)\|^2$
$G_0(s)$		$2\alpha(M_Z^2)v_e a_\tau \mathrm{Re}H(s)$	$D_0\|H(s)\|^2$
$G_1(s)$		$2\alpha(M_Z^2)a_e v_\tau \mathrm{Re}H(s)$	$D_1\|H(s)\|^2$
$G_2(s)$		$2\alpha(M_Z^2)v_e a_\tau \mathrm{Im}H(s)$	$D_2\|H(s)\|^2$

Table 2.2: *Contributions to the functions appearing in the differential cross section, equation 2.22, from γ-exchange, Z^0-exchange and their interference.*

given in table 2.2, where the contributions from γ-exchange, Z^0-exchange and their interference are shown separately. The following notation has been introduced:

$$H(s) = \frac{\alpha}{4\sin^2\theta_W \cos^2\theta_W}\, s\, \chi_0(s)\ , \tag{2.24}$$

and

$$\begin{aligned} C_0 &= (|v_e|^2 + |a_e|^2)(|v_\tau|^2 + |a_\tau|^2) \\ C_1 &= 4\mathrm{Re}(v_e a_e^*)\ \mathrm{Re}(v_\tau a_\tau^*) \\ C_2 &= (|v_e|^2 + |a_e|^2)(|a_\tau|^2 - |v_\tau|^2) \\ D_0 &= (|v_e|^2 + |a_e|^2)\ 2\mathrm{Re}(v_\tau a_\tau^*) \\ D_1 &= 2\mathrm{Re}(v_e a_e^*)(|v_\tau|^2 + |a_\tau|^2) \\ D_2 &= -(|v_e|^2 + |a_e|^2)\ 2\mathrm{Im}(v_\tau a_\tau^*)\ . \end{aligned} \tag{2.25}$$

The differential cross section given by equation 2.23 contains terms coming from the interference between the diagrams of photon and Z^0 exchange, which are proportional to the real part of the Z^0 propagator and therefore vanish for $s = M_Z^2$. Thus, at the Z^0 peak these terms cancel out. In other words, the several observables

at the Z^0 resonance can be written in terms of the constants C_i and D_i defined in equations 2.25, except for a small contribution from the photon exchange that will be discussed in chapter 5.

From the $\frac{d\sigma}{d\Omega}(s_1, s_2)$, expression 2.23, it is possible to identify the different asymmetries and polarization observables mentioned in the previous section.

The longitudinal polarization of the tau lepton, $P_\tau(\cos\theta)$, is a parity-violating observable, defined as

$$P_\tau(\cos\theta) = \frac{N^+(\cos\theta) \; - \; N^-(\cos\theta)}{N^+(\cos\theta) \; + \; N^-(\cos\theta)} \; , \tag{2.26}$$

where $N^\pm(\cos\theta)$ are the number of events with $\pm$ helicity, and whose angular distribution is deduced from equation 2.23 to be

$$P_\tau(\cos\theta) = -\frac{G_0(s)(1+\cos^2\theta) + G_1(s)\; 2\cos\theta}{F_0(s)(1+\cos^2\theta) + F_1(s)\; 2\cos\theta} \; . \tag{2.27}$$

As a consequence of the assumed helicity-conserving vertex, it can be seen that $P_{\tau+} = P_{\tau-}$, and the longitudinal spin correlation is equal to one.

With only the Z^0-exchange term, the distribution (2.27) can be written as:

$$P_\tau(\cos\theta) = -\frac{\mathcal{A}_\tau + \mathcal{A}_e \; 2\cos\theta/(1+\cos^2\theta)}{1 + \mathcal{A}_\tau\mathcal{A}_e \; 2\cos\theta/(1+\cos^2\theta)} \; , \tag{2.28}$$

where $\mathcal{A}_\tau$ is the tau polarization averaged over all tau production angles

$$\mathcal{A}_\tau = -P_\tau = - < P_\tau(\cos\theta) > = \frac{D_0}{C_0} = \frac{2\mathrm{Re}(v_\tau a_\tau^*)}{(|v_\tau|^2 + |a_\tau|^2)} \; , \tag{2.29}$$

and $\mathcal{A}_e$ is the polarization of the Z^0, also called the forward-backward polarization asymmetry, given by

$$\mathcal{A}_e = -P_Z = \frac{D_1}{C_0} = \frac{2\mathrm{Re}(v_e a_e^*)}{(|v_e|^2 + |a_e|^2)} \; . \tag{2.30}$$

It should be noticed that the angular dependence of the longitudinal polarization is seen in equation 2.27 to be mainly controlled by the factor $G_1(s)/F_0(s)$. At the peak of the Z^0 resonance, and when disregarding the γ-exchange term, $\mathcal{A}_e$ becomes the polarization of the Z^0.

The forward-backward charge asymmetry of the event distribution, when the final polarizations are not observed, can be obtained by

$$A_{FB} = \frac{\int_{\cos\theta>0} \frac{d\sigma}{d\cos\theta} - \int_{\cos\theta<0} \frac{d\sigma}{d\cos\theta}}{\int_{\cos\theta>0} \frac{d\sigma}{d\cos\theta} + \int_{\cos\theta<0} \frac{d\sigma}{d\cos\theta}} \quad , \tag{2.31}$$

which can be shown to be

$$A_{FB} = \frac{3}{4} \mathcal{A}_e \mathcal{A}_\tau \ . \tag{2.32}$$

Furthermore, the differential equation 2.23 can be used to analyze correlations between the tau pairs. The transverse spin correlations lead to aplanarities of the decay products. The expected value of the product of the transverse components, which coincides with the expected value of the product of the normal components in the Standard Model, is mainly sensitive to $\frac{C_2}{C_0}$. On the other hand, the correlation between the normal and transverse component leads to a sensitivity modulated by a term proportional to $\frac{G_2}{F_0}$. These correlations have been studied in detail in reference [11, 16], and are not discussed any further here.

2.5 Correlated Decay Distributions

In this section the cross section for the production and decay of tau pairs is explicitly calculated as a function of quantities that depend on both taus simultaneously. Of those correlated distributions we will concentrate on those relating to angles, in particular on the differential distribution as a function of the acollinearity angle of the one-prong decay products. In order to derive the correlated distributions, it can be stressed that these distributions cannot be measured as functions of variables that depend on the tau direction because the neutrinos escape detection.

The correlated distributions have already been proved [17, 18, 19] to be interesting in order to measure the tau Michel parameters and to determine the electroweak couplings associated to the tau production and its decay. In the following development, the V − A structure of the weak charged current is taken from the prediction of the Standard Model and no attempt is done for possible further studies.

2.5.1 Tau Decay

To compute the correlated distributions depending on observable quantities consider the 1-prong decay process where the tau has an arbitrary polarization s^* in its rest frame and x is a charged particle with four-momentum q

$$\tau^{\pm}(s^*) \to x^{\pm}(q) + \ldots$$

The decay distribution in the tau rest frame may be written in a general form as

$$d\Gamma^{\pm}(s^*, q) = \Gamma(\tau \to \nu_\tau + x_i + \ldots)\ [A_1^{(i)} \mp \alpha_i\ \vec{q}_i^{\,*} \cdot \vec{s}^{\,*}\ A_2^{(i)}]\ d^3q_i^* \ , \qquad (2.33)$$

where the symbol * is used to represent variables in the tau rest frame [20]. The decay distribution functions $A_1^{(i)}$ and $A_2^{(i)}$, and the polarization parameters α_i depend on the particular decay channel under consideration.

Leptonic channels

For the purely leptonic processes, the most general matrix element for the tau decay is given by

$$T = \frac{G_\mu}{\sqrt{2}} \sum_n (\bar{\tau}\sigma^n\nu_\tau)[g_n(\bar{\nu}_l\sigma_n l) + g_n^5(\bar{\nu}_l\sigma_n\gamma_5 l)] \ , \qquad (2.34)$$

where G_μ is the Fermi constant, the index n stands for the kind of interaction to be considered, that is scalar, pseudo-scalar, vector, axial and tensor and σ designates the appropriate combinations of Dirac matrices. In the Standard Model the only non zero couplings are

$$g_v = -g_a = -g_v^5 = g_a^5 = 1 \ . \qquad (2.35)$$

In terms of the so-called Michel parameters [21], the Standard Model prediction is

$$\rho_i = \delta_i = \frac{3}{4} \qquad \eta_i = 0 \qquad \xi_i = 1 \ , \qquad (2.36)$$

where the α_i parameter can be identified as

$$\alpha_i = -\frac{\xi_i}{3} \ . \qquad (2.37)$$

So, for purely leptonic processes, $\alpha_i = -\frac{1}{3}$ $(i = e, \mu)$ and the corresponding decay distribution functions derived from 2.34 may be written as [20]

$$A_1^{(i)} = \frac{a_1^{(i)}}{4\pi\lambda_i E_i^*} \qquad A_2^{(i)} = \frac{a_2^{(i)}}{4\pi\lambda_i E_i^*} , \tag{2.38}$$

which in the standard theory for the charged current weak interactions are [2]

$$a_1^{(i)} = -\frac{m_i^2}{6} + \frac{W_i}{2}E_i^* - \frac{1}{3}E_i^{*2} \tag{2.39}$$

$$a_2^{(i)} = -W_i + \frac{P_i}{2} + E_i^* , \tag{2.40}$$

where W_i (P_i) is the maximal energy (momentum) of the leptons in the tau rest frame

$$W_i = \frac{m_\tau^2 + m_i^2}{2m_\tau} \qquad P_i = \frac{m_\tau^2 - m_i^2}{2m_\tau} . \tag{2.41}$$

The normalization factor λ_i turns out to be

$$\begin{aligned} \lambda_i &= \int_0^{P_i} \frac{a_1^{(i)}}{E_i^*} q_i^{*2} dq_i^* \\ &= \frac{1}{12}P_i^3 W_i - \frac{1}{8}m_i^2 P_i W_i + \frac{1}{8}m_i^4 \ln\frac{m_\tau}{m_i} . \end{aligned} \tag{2.42}$$

Hadronic channels

For the hadronic processes, a matrix element similar to that of expression 2.34 can be written including, however, the usual parameterization for the charged hadronic current.

Then, for two-body decay processes $(x_i = \pi, \rho, a_1)$, the polarization analyzers are

$$\alpha_\pi = \xi = 1 , \tag{2.43}$$

for spin 0 particles, and

$$\alpha_i = \frac{m_\tau^2 - 2m_i^2}{m_\tau^2 + 2m_i^2}\,\xi \quad (i = \rho, a_1) , \tag{2.44}$$

[2] More details on $a_1^{(i)}$ and $a_2^{(i)}$ can be found in appendix A.

for spin 1 particles. Using the nominal values for the masses of ρ, a_1 and τ [22], yields $\alpha_\rho \simeq 0.46$ and $\alpha_{a_1} \simeq 0.12$. The momentum distributions [20] are given by

$$A_1^{(i)} = P_i A_2^{(i)} = \frac{1}{4\pi} \frac{\delta(q_i^* - P_i)}{P_i^2} \,. \tag{2.45}$$

2.5.2 The Process $e^-e^+ \to \tau^-\tau^+ \to x_1^- x_2^+ + \ldots$

From the differential cross section for tau production with polarizations s_1^* and s_2^* given by equation 2.23 and from the angular distributions of the tau decays with spin s_i^* in its rest frame, the correlated distribution for tau production and subsequent decays in the process

$$e^-e^+ \to \tau^-\tau^+ \to x_1^- x_2^+ + \ldots \,,$$

is given by

$$d\sigma(e^-e^+ \to x_1 x_2) = 4 d\sigma(\vec{n_1}^*, \vec{n_2}^*) \, \frac{d\Gamma_{x_1}}{\Gamma_\tau} \, \frac{d\Gamma_{x_2}}{\Gamma_\tau} \,. \tag{2.46}$$

It has been assumed that $\Gamma_\tau \ll m_\tau$, and $d\sigma(\vec{n_1}^*, \vec{n_2}^*)$ is obtained from $d\sigma(\vec{s_1}^*, \vec{s_2}^*)$ by substituting for the polarization vectors $\vec{s_1}^*$ and $\vec{s_2}^*$ [13, 23, 24] the expressions

$$\vec{n_1}^* = \alpha_1 \frac{A_2^{(1)}}{A_1^{(1)}} \vec{q_1}^* \tag{2.47}$$

$$\vec{n_2}^* = -\alpha_2 \frac{A_2^{(2)}}{A_1^{(2)}} \vec{q_2}^* \,, \tag{2.48}$$

where the terms proportional to $\frac{m_\tau^2}{M_Z^2}$ are neglected. The differential decay width $d\Gamma_{x_i}$ for an unpolarized tau is

$$d\Gamma_{x_i} = \frac{1}{2} \sum_{s_i} d\Gamma_{x_i}^{(s_i)} = \Gamma(\tau \to \nu_\tau + x_i + \ldots) \, A_1^{(i)} d^3 q_i^* \,, \tag{2.49}$$

where Γ_τ is the total width of the tau.

Finally, introducing expressions 2.47 and 2.48 in 2.23 according to 2.46, the

correlated distribution obtained is

$$\begin{aligned}\frac{d^8\sigma}{d\Omega\ d^3q_1^* d^3q_2^*} &= K(s)\Big\{[A_1^{(1)}A_1^{(2)} + \alpha_1\alpha_2 A_2^{(1)}A_2^{(2)} q_1^* q_2^* \cos\theta_1^* \cos\theta_2^*] \times \\ &\quad [F_0(s)(1+\cos^2\theta) + F_1(s)2\cos\theta] \\ &- [\alpha_1 A_2^{(1)}A_1^{(2)} q_1^* \cos\theta_1^* + \alpha_2 A_1^{(1)}A_2^{(2)} q_2^* \cos\theta_2^*] \times \\ &\quad [G_0(s)(1+\cos^2\theta) + G_1(s)2\cos\theta] \\ &+ \alpha_1\alpha_2 A_2^{(1)}A_2^{(2)} q_1^* q_2^* \sin\theta_1^* \sin\theta_2^* \times \\ &\quad \sin^2\theta[F_2(s)\cos(\phi_2^* - \phi_1^*) + G_2(s)\sin(\phi_2^* - \phi_1^*)]\Big\}\ , \end{aligned} \tag{2.50}$$

with

$$K(s) = \frac{1}{4s} Br(\tau \to x_1) Br(\tau \to x_2)\ , \tag{2.51}$$

where q_1^*, q_2^* are the momenta of the particles x_1, x_2, and θ_i^*, ϕ_i^* (i=1,2) are the polar and azimuthal angles that define the direction of the particles x_1, x_2 in the $\tau^\mp$ rest frame respectively.

This distribution, however, depends on the tau direction θ in the laboratory frame, as well as on the momenta $\vec{q_1}^*$, $\vec{q_2}^*$ of the particles x_1, x_2 in the $\tau^\mp$ rest frames, respectively. Without reconstruction of the tau direction, one cannot measure these variables experimentally. Instead, one can rewrite this cross section (equation 2.50) in the laboratory frame and use variables independent of the tau direction.

For this purpose the laboratory frame is defined in such a way that the momentum of x_i (q_i, θ_i, ϕ_i) (i = 1,2) is referred to the direction of the $\tau^\mp$, $\vec{p_i}$ (i = 1,2), respectively. For $\sqrt{s} = M_Z$, the boost connecting the laboratory and the $\tau^\mp$ rest frames is defined by the parameters $\gamma = M_Z/(2m_\tau)$, and $\beta = \sqrt{1-\gamma^{-2}}$. Then, the variables in the two systems are related by

$$\begin{aligned} E_i^* &= \gamma(E_i - \beta q_i \cos\theta_i) \\ q_i^* \cos\theta_i^* &= \gamma(q_i \cos\theta_i - \beta E_i) \\ q_i^* \sin\theta_i^* &= q_i \sin\theta_i \\ \phi_i^* &= \phi_i\ , \end{aligned} \tag{2.52}$$

with the Jacobian

$$\frac{\partial(q_i^*, \cos\theta_i^*)}{\partial(q_i, \cos\theta_i)} = \frac{E_i^*}{q_i^{*2}} \frac{q_i^2}{E_i}\ . \tag{2.53}$$

The range of the angular variables depends on the decay channel. For two-body decays the energy and the angle are not independent variables, so that for a given energy the angle is given by

$$\cos\theta_i = \cos\zeta_i \equiv \left(\frac{\gamma E_i - W_i}{\beta\gamma q_i}\right) . \tag{2.54}$$

For the leptons, which appear in three-body decays, one has instead a certain range of $\cos\theta_i$ that is $0 \leq \theta_i \leq \zeta_i$ for a given energy.

The variables θ_1, ϕ_1, θ_2, ϕ_2, which refer to the x_1 and x_2 directions with respect to their parent $\tau^{\mp}$, are still not directly observable. The measurable quantities are instead the opening angle θ_{12} between x_1 and x_2 and the orientation of the x_1 x_2 momentum plane with respect to the electron beam.

The transverse and normal spin correlations between both taus only appear in 2.50 associated with the azimuthal variable $\phi' = \phi_1 - \phi_2$, related to the orientation of the $x_1 x_2$ momentum plane. These correlations give rise to the previously mentioned aplanarity observables [11]. However, in the present analysis ϕ' is integrated out and further studies are restricted to the acollinearity distribution.

To analyze the correlated distribution in the laboratory frame, it is convenient to define the acollinearity angle ε between the two decay products: $\varepsilon = \pi - \theta_{12}$. The acollinearity angle ε is related to the azimuthal angle ϕ between the $\tau^- x_1^-$ momentum plane and $\tau^+ x_2^+$ momentum plane in the laboratory frame ($\phi = \phi_1 + \phi_2$) by:

$$\cos\varepsilon = \cos\theta_1 \cos\theta_2 - \sin\theta_1 \sin\theta_2 \cos\phi \ . \tag{2.55}$$

After including the boost transformation to the laboratory frame and the substitutions in terms of the observable quantities expression 2.50 leads to

$$\begin{aligned}
\frac{d^5\sigma}{d\Omega dE_1 dE_2 d\cos\varepsilon} \;=\; & 4\pi K(s) q_1\, q_2 \int \frac{E_1^* E_2^*}{Q} d\cos\theta_1 d\cos\theta_2 \times \\
& \Big\{ [A_1^{(1)} A_1^{(2)} + \alpha_1\alpha_2 A_2^{(1)} A_2^{(2)} q_1^* \cos\theta_1^* q_2^* \cos\theta_2^*] \times \\
& [F_0(s)(1+\cos^2\theta) + F_1(s) 2\cos\theta] \\
- \; & [\alpha_1 A_2^{(1)} A_1^{(2)} q_1^* \cos\theta_1^* + \alpha_2 A_1^{(1)} A_2^{(2)} q_2^* \cos\theta_2^*] \times \\
& [G_0(s)(1+\cos^2\theta) + G_1(s) 2\cos\theta] \Big\} \ ,
\end{aligned} \tag{2.56}$$

where for compactness of notation not all the * variables are substituted, so E_i^* and $q_i^* \cos\theta_i^*$, defined in the $\tau^{\mp}$ rest frames, are given in 2.52 in terms of the laboratory variables E_i, q_i, $\cos\theta_i$, and Q^{-1} is the Jacobian $\dfrac{\partial\phi}{\partial(\cos\varepsilon)}$, with

$$Q = \sqrt{\sin^2\theta_1 \sin^2\theta_2 - (\cos\theta_1 \cos\theta_2 - \cos\varepsilon)^2} \ . \tag{2.57}$$

The non-observable angles θ_1 and θ_2 are integrated out in equation 2.56; again for compactness the explicit relations are not written . This result still depends on the production angle θ of the tau with respect to the beam. However, equation 2.56 can be expanded to the dominant order in the dilation factor γ, taking into account that $\theta_1, \theta_2, \varepsilon \sim \gamma^{-1}$. As the angular distribution of the tau is explicitly dependent on $\cos\theta$, it can be substituted by $\cos\theta = \cos\theta_- + \mathcal{O}\left(\dfrac{1}{\gamma^2}\right)$, where θ_- is the polar angle between the x_1^- decay product and the e^- beam. This will be the physical meaning of $\cos\theta$ from now on.

2.5.3 Angular Correlations

The correlated angular distribution $\dfrac{d^2\sigma}{d\cos\theta d\varepsilon}$ is obtained from equation 2.56 by integrating out E_1 and E_2, as well as the azimuthal angle of the tau. This yields

$$\begin{aligned} \frac{d^2\sigma}{d\cos\theta d\varepsilon} &= 2\pi K(s) \Big\{ F(\varepsilon) \left[F_0(s)(1+\cos^2\theta) + F_1(s) 2\cos\theta \right] \\ &- G(\varepsilon) \left[G_0(s)(1+\cos^2\theta) + G_1(s) 2\cos\theta \right] \Big\} \ . \end{aligned} \tag{2.58}$$

The functions $F(\varepsilon)$ and $G(\varepsilon)$ of the acollinearity angle ε are defined as

$$F(\varepsilon) = Q_{11}(\varepsilon) + \alpha_1\alpha_2 Q_{22}(\varepsilon) \tag{2.59}$$

$$G(\varepsilon) = \alpha_1 Q_{21}(\varepsilon) + \alpha_2 Q_{12}(\varepsilon) \ . \tag{2.60}$$

The functions $Q_{ij}(\varepsilon)$ are defined as [25]

$$\begin{aligned} Q_{ij}(\varepsilon) \equiv\ & 4\pi \sin\varepsilon \int \frac{E_1^* E_2^*}{Q} q_1\ q_2\ dE_1 d\cos\theta_1 dE_2 d\cos\theta_2\ \times \\ & A_i^{(1)} (q_1^* \cos\theta_1^*)^{i-1} A_j^{(2)} (q_2^* \cos\theta_2^*)^{j-1} \ . \end{aligned} \tag{2.61}$$

They satisfy

$$\int d\varepsilon Q_{ij}(\varepsilon) = \delta_{i1}\delta_{j1} \ , \tag{2.62}$$

showing that the information on the polarization distribution is lost when equation 2.58 is integrated over ε. A more detailed description of the integration of those functions is given in appendix A.

As can be seen from equation 2.61, $Q_{12}(\varepsilon) = Q_{21}(\varepsilon)$ when the τ^+ and τ^- decay products have the same mass. The use of the acollinearity angle ε as an observable introduces a constraint between the (unobservable) quantities $\cos\theta_1, \cos\theta_2$ due to the relation 2.55. Specifying ε defines an allowed region in (θ_1, θ_2)-space, which is a rectangle whose boundaries are obtained for coplanar events ($\cos\phi = \pm 1$). This rectangle defines also an allowed region in (E_1, E_2)-space for a given ε and confines the region of integration over $\cos\theta_1$ and $\cos\theta_2$ to its interior. As a result, the integration over $\cos\theta_1$ depends on $\cos\theta_2$ and one cannot factorize the functions $Q_{ij}(\varepsilon)$. It will be shown in the next section that in the case of the energy-energy correlations the terms in $\cos\theta_1$ and $\cos\theta_2$ can be factorized.

Although the functions $Q_{ij}(\varepsilon)$ depend on the final states x_1 and x_2, the general shape is common for all the 1-prong decays considered. The Q_{ij} functions corresponding to the $\tau^- \to \pi^-\nu_\tau$, $\tau^+ \to \pi^+\bar{\nu_\tau}$ channel are shown in figure 2.6, and in figure 2.7 those corresponding for $\tau^- \to e^-\nu_\tau\bar{\nu}_e$, $\tau^+ \to \mu^+\bar{\nu_\tau}\nu_\mu$. Figure 2.8 shows the Q_{ij} functions corresponding to the $\tau^- \to e^-\nu_\tau\bar{\nu}_e$, $\tau^+ \to \rho^+\bar{\nu_\tau}$, where the difference between $Q_{12}(\varepsilon)$ and $Q_{21}(\varepsilon)$ is distinguishable.

From equation 2.58, two independent observables can be defined which at the peak of the Z^0 resonance only depend on $\mathcal{A}_\tau$ and $\mathcal{A}_e$ [25]. Once equation 2.58 is integrated over $\cos\theta$, the normalized acollinearity distribution is given by

$$\frac{1}{\sigma}\frac{d\sigma}{d\varepsilon} = F(\varepsilon) + \mathcal{A}_\tau\, G(\varepsilon)\,, \tag{2.63}$$

which is an observable linear in $\mathcal{A}_\tau$.

Also, the acollinearity distribution of the forward-backward asymmetry can be defined as

$$A_{FB}(\varepsilon) = \frac{\int_{\cos\theta>0}\frac{d\sigma}{d\cos\theta d\varepsilon} - \int_{\cos\theta<0}\frac{d\sigma}{d\cos\theta d\varepsilon}}{\int_{\cos\theta>0}\frac{d\sigma}{d\cos\theta d\varepsilon} + \int_{\cos\theta<0}\frac{d\sigma}{d\cos\theta d\varepsilon}}\,. \tag{2.64}$$

At the peak of the Z^0, this can be written

$$A_{FB}(\varepsilon) = \frac{3}{4}\,\frac{\mathcal{A}_e\,\{\mathcal{A}_\tau\,F(\varepsilon) + G(\varepsilon)\}}{F(\varepsilon) + \mathcal{A}_\tau G(\varepsilon)}\,. \tag{2.65}$$

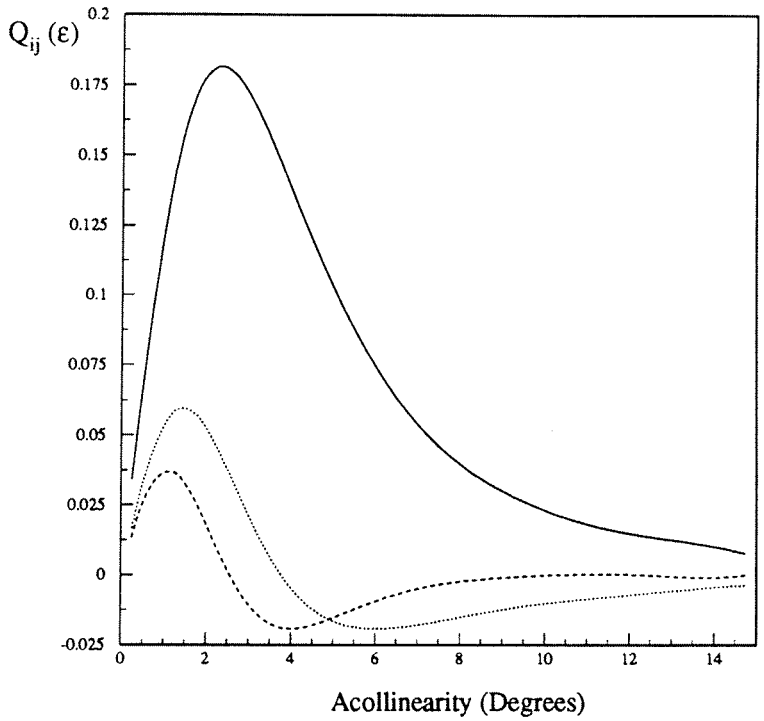

Figure 2.6: *Functions $Q_{ij}(\varepsilon)$ for the $\pi^-\pi^+$ decay channel. Continuous line: Q_{11}; dashed line: Q_{22}; dotted line: $Q_{21} = Q_{12}$.*

Combining expressions 2.63 and 2.65, the observables $\mathcal{A}_e$ and $\mathcal{A}_\tau$ can be separated. Alternatively, if universality is assumed, 2.63 and 2.65 provide independent methods to determine $\mathcal{A}_{e-\tau}$.

2.5.4 Energy-Energy Correlations

For completeness, the expression for the energy-energy correlations is also given because when measuring the tau polarization dependence from the acollinearity distributions, since the acollinearity is kinematically correlated with both energies, some genuine energy-energy correlation information is measured too.

The general distribution $\dfrac{d^4\sigma}{d\Omega dE_1 dE_2}$ can be obtained by integrating equation

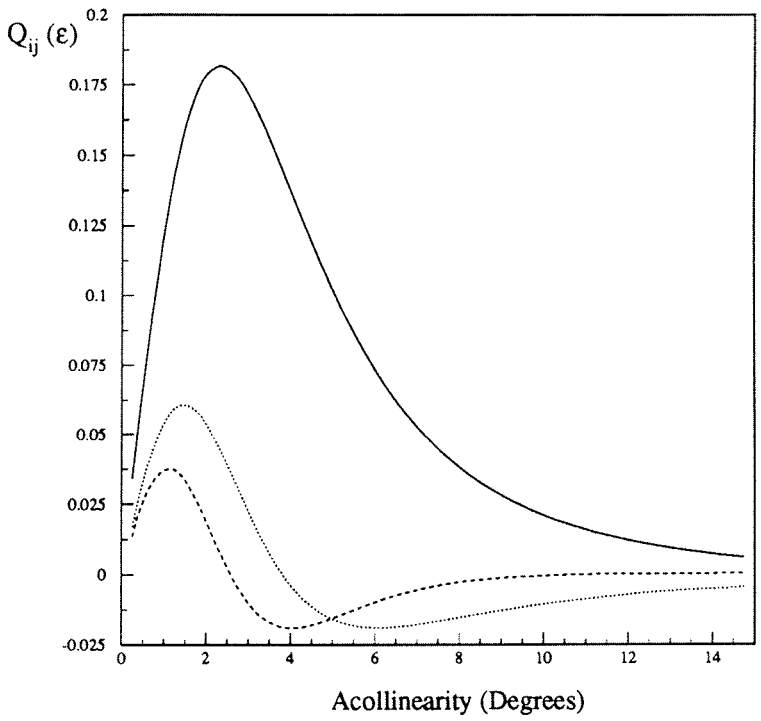

Figure 2.7: *Functions $Q_{ij}(\varepsilon)$ for the $e^-\mu^+$ decay channel. Continuous line: Q_{11}; dashed line: Q_{22}; dotted line: $Q_{21} = Q_{12}$.*

2.56 over ε:

$$\frac{d^4\sigma}{d\Omega dE_1 dE_2} = \int_{\cos(\theta_1-\theta_2)}^{\cos(\theta_1+\theta_2)} \frac{d^5\sigma}{d\Omega dE_1 dE_2 d\cos\varepsilon} d\cos\varepsilon \tag{2.66}$$

$$\begin{aligned} &= 4\pi^2 K(s)\; q_1\; q_2 \int E_1^* E_2^* d\cos\theta_1 d\cos\theta_2 \times \\ &\quad \Big\{ [A_1^{(1)} A_1^{(2)} + \alpha_1\alpha_2 A_2^{(1)} A_2^{(2)} q_1^* \cos\theta_1^* q_2^* \cos\theta_2^*] \times \\ &\quad [F_0(s)(1+\cos^2\theta) + F_1(s) 2\cos\theta] \\ &- [\alpha_1 A_2^{(1)} A_1^{(2)} q_1^* \cos\theta_1^* + \alpha_2 A_1^{(1)} A_2^{(2)} q_2^* \cos\theta_2^*] \times \\ &\quad [G_0(s)(1+\cos^2\theta) + G_1(s) 2\cos\theta] \Big\} \; . \end{aligned} \tag{2.67}$$

The energy-energy correlated distributions are considerably simpler than the angular distribution, due to the fact that the integration over $\cos\theta_1$ is independent of the integration over $\cos\theta_2$. Thus for leptons

$$\cos\zeta_i \leq \cos\theta_i \leq 1 \; ,$$

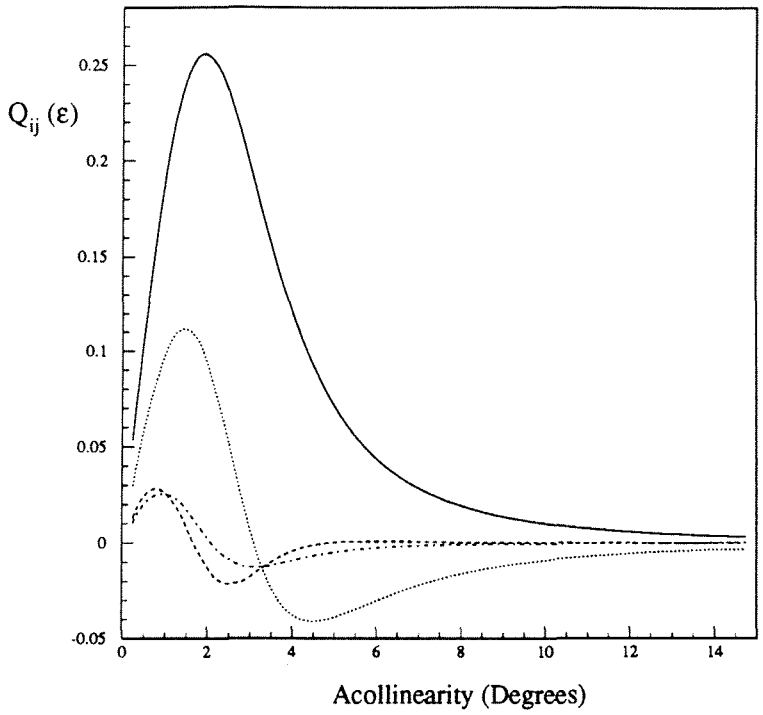

Figure 2.8: *Functions $Q_{ij}(\varepsilon)$ for the $e^-\rho^+$ decay channel. Continuous line: Q_{11}; dashed line: Q_{22}; dotted line: Q_{21}; dashed-dotted line: Q_{12}.*

and for mesons

$$\cos\theta_i = \cos\zeta_i \ ,$$

with ζ_i as given in equation 2.54.

After integrating over the tau direction, the distribution function around the Z^0 resonance for any combination of leptons and mesons in the tau decays can therefore be written as:

$$\begin{aligned}\frac{1}{\sigma}\frac{d^2\sigma}{dE_1 dE_2} &= \Big\{H_0^{(1)}(E_1)H_0^{(2)}(E_2) + \alpha_1\alpha_2 H_1^{(1)}(E_1)H_1^{(2)}(E_2) \\ &\quad + P_\tau[\alpha_1 H_1^{(1)}(E_1)H_0^{(2)}(E_2) + \alpha_2 H_0^{(1)}(E_1)H_1^{(2)}(E_2)]\Big\} \ . \quad (2.68)\end{aligned}$$

For leptons one gets [20]

$$\begin{aligned} H_0^{(i)}(E_i) &= \frac{q_i}{2\lambda_i}\int_{\cos\zeta_i}^{1} a_1^{(i)} d\cos\theta_i \\ &= \frac{q_i}{2\lambda_i}\sum_{n=0}^{2} R_n^{(i)}(E_i)\frac{1}{n+1}(1-\cos^{n+1}\zeta_i) \qquad (2.69) \\ H_1^{(i)}(E_i) &= \frac{q_i}{2\lambda_i}\int_{\cos\zeta_i}^{1} a_2^{(i)}(q_i^*\cos\theta_i^*) d\cos\theta_i \\ &= \frac{q_i}{2\lambda_i}\sum_{n=0}^{2} S_n^{(i)}(E_i)\frac{1}{n+1}(1-\cos^{n+1}\zeta_i)\ , \qquad (2.70) \end{aligned}$$

where the coefficients $R_n^{(i)}(E_i)$ and $S_n^{(i)}(E_i)$ are defined by writing the functions $a_1^{(i)}$ and $a_2^{(i)}(q_i^*\cos\theta_i^*)$ in the laboratory frame

$$a_1^{(i)} = \sum_{n=0}^{2} R_n^{(i)}(E_i)\cos^n\theta_i \qquad a_2^{(i)}(q_i^*\cos\theta_i^*) = \sum_{n=0}^{2} S_n^{(i)}(E_i)\cos^n\theta_i\ , \qquad (2.71)$$

whereas for mesons

$$\begin{aligned} H_0^{(i)}(E_i) &= \frac{1}{2\gamma\beta P_i} \qquad (2.72) \\ H_1^{(i)}(E_i) &= \frac{1}{2\gamma\beta P_i}\frac{E_i-\gamma W_i}{\gamma\beta P_i}\ . \qquad (2.73) \end{aligned}$$

Around the Z^0-resonance, it can be seen that the s-dependence of the energy correlation given by equation 2.68 is quite smooth. When this observable is integrated over E_2, the well known single tau decay spectrum is reproduced [26].

Chapter 3

The ALEPH Detector

3.1 LEP Storage Ring

The measurement of the Z^0 and W boson properties to test the Standard Model, and searches for possible new phenomena, provided the physics motivation behind the construction of the Large Electron-Positron collider, LEP [27]. The LEP collider accelerates electron and positrons up to 55 GeV for production of Z^0 in its first phase. A second phase is foreseen in which the LEP machine is expected to provide collisions at a center of mass energy of 200 GeV, to study W production and decay properties in detail.

The LEP storage ring consists of eight arcs alternating with eight straight sections. The electrons and positrons are maintained on circular orbits by mean of 3368 dipole magnets located in the arcs. The beams are focused by 808 quadrupole and sextupoles magnets positioned along the straight and arc sections. The electron and positron beams collide at the center of four of the straight sections, where the detectors are installed.

The LEP injection chain is shown in figure 3.1. It consists of a two stage linear accelerator (LINAC) which accelerates electrons and positrons. In the first stage some electrons are first accelerated up to 200 MeV, and are used to produce positrons by colliding in a intermediate target. Then, in the second stage, electrons and positrons are accelerated up to 600 MeV, before being injected into the Electron Positron Accumulating ring (EPA), where they are accumulated and cooled by synchrotron radiation. From there, electrons and positrons are injected into the

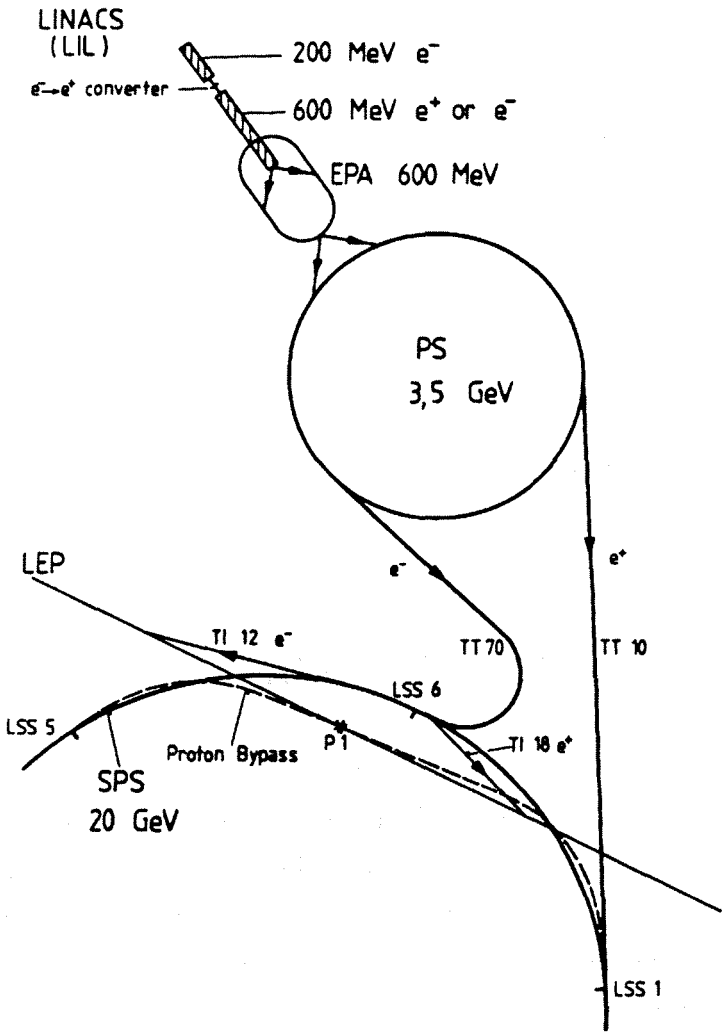

Figure 3.1: *Scheme of the LEP injectors and accelerators.*

Proton Synchrotron (PS), where the energy is raised up to 3.5 GeV. Then, they are sent to the Super Proton Synchrotron (SPS) for a further acceleration up to 20 GeV. Finally, bunches of electrons and positrons are transferred into the LEP ring and accelerated to a maximum energy of 55 GeV. Four bunches per beam circulate in opposite directions, and are accelerated using klystron-powered radiofrequency cavities. The bunches are typically 1.2 cm long with a horizontal and vertical size of about 250 μm and 12 μm respectively at the collision points. Other LEP parameters of interest are shown in table 3.1. Presently, the luminosity delivered by LEP in good running conditions is about 10^{32} cm^{-2} s^{-1}.

Parameter	Value	Units
Circumference	26667	m
Average radius	4243	m
Bending radius in the dipoles	3096	m
Depth	80-130	m
Number of interaction points	8	
Number of experimental areas	4	
Number of bunches per beam	4 - 8	
RMS Bunch length	12	mm
Horizontal bunch sigma	200	μm
Vertical bunch sigma	12	μm
Injection Energy	20	GeV
Maximum beam energy (phase I)	55	GeV
RF Frequency	353	MHz
Total current per beam	29	mA
Luminosity	10^{32}	$\mathrm{cm}^{-2}\ \mathrm{s}^{-1}$
Vertical β_V^*	5	cm
Horizontal β_H^*	$25\times\beta_V^*$	cm

Table 3.1: *Main LEP parameters.*

3.2 The ALEPH Detector

ALEPH (Apparatus for LEP PHysics) is a general purpose detector for e^+e^- interactions described in great detail in [28, 29]. The detector was conceived to cover as much as possible of the total solid angle and to collect the maximum amount of information per event. For this purpose, ALEPH has been designed with tracking detectors and a high magnetic field, to permit precise momentum measurement for charged particles, and calorimeters surrounding it to measure neutral particles and provide good particle identification.

The ALEPH detector has a cylindrical structure around the beam pipe as in figure 3.2 where an overall view of the detector with the main subdetectors is shown.

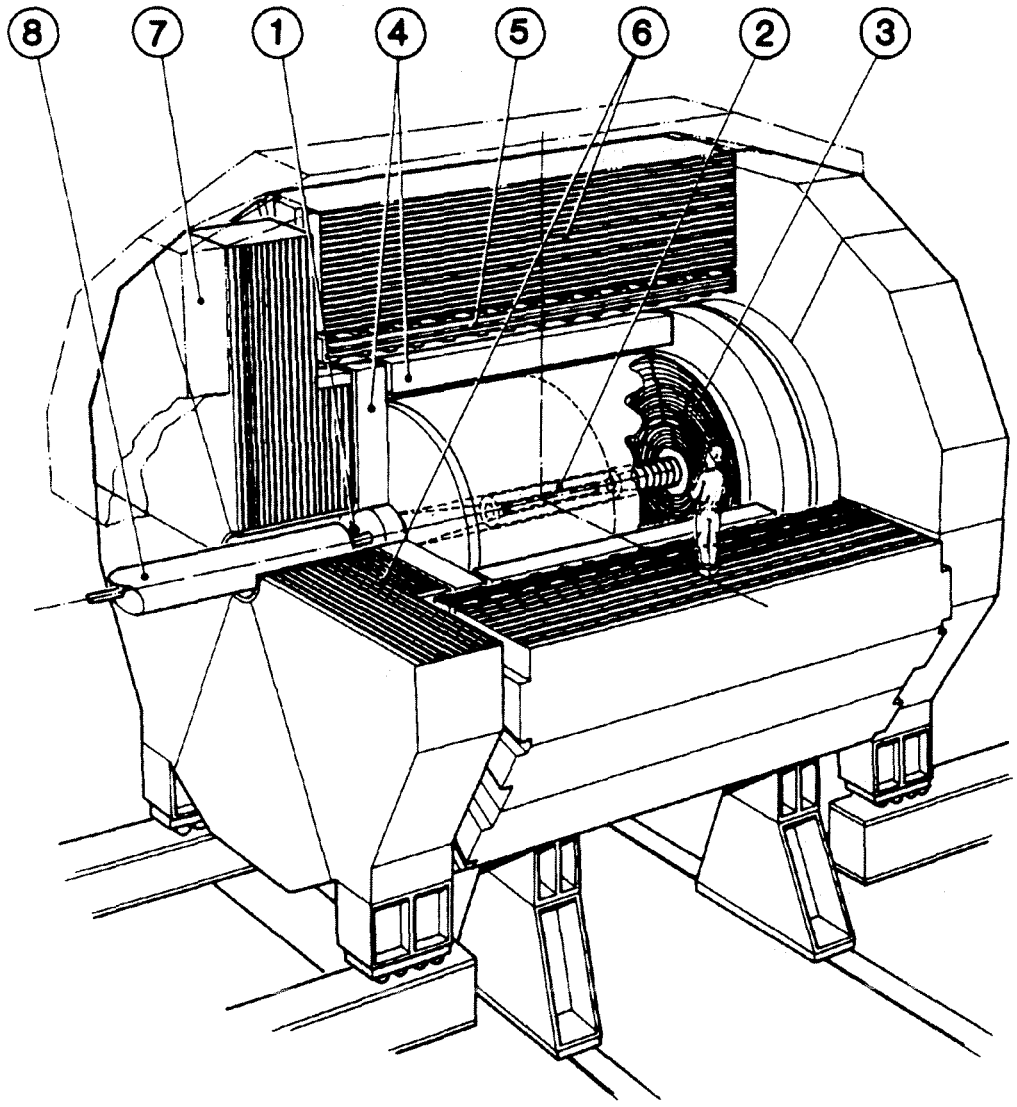

Figure 3.2: *Overall view of the ALEPH detector. (1) Luminosity Monitor. (2) Inner Tracking chamber. (3) Time Projection Chamber. (4) Electromagnetic Calorimeter. (5) Superconducting coil. (6) Hadronic Calorimeter. (7) Muon chambers. (8) Superconducting quadrupole around the beam pipe.*

The electron-positron interactions take place inside the beam pipe. The first detector that surrounds the beam pipe is a double layer silicon strip vertex detector, not visible in figure 3.2, for very accurate measurement of tracks coming from the interaction point.

There are two tracking chambers in ALEPH. A small inner tracking chamber (ITC) using axial wires is a drift chamber. Surrounding this first chamber, a large cylindrical time projection chamber (TPC) is located, providing a three dimensional measurement for each track. Beyond the tracking chambers is the electromagnetic calorimeter (ECAL) consisting of alternating layers of lead sheets and proportional tubes. A magnet consisting of a iron yoke and a superconducting solenoid surrounds the electromagnetic calorimeter. The magnet provides a magnetic field of 1.5 T parallel to the LEP beam direction with high uniformity. The iron yoke, just outside the coil, serves several functions. Firstly, it shapes the longitudinal magnetic field. Secondly, it is used as a sampling medium for the hadron calorimeter (HCAL). Finally, it is also used as support for most of the other subdetectors. The hadron calorimeter consists of limited streamer tubes interleaved with the iron plates forming the magnet return yoke. The outermost subdetector is the muon chambers which consists of a two double layers of limited streamer tubes with a half meter separation between them.

For the luminosity measurements there are three detectors. The original luminosity calorimeter LCAL is constructed like the electromagnetic calorimeter. Recently, a second calorimeter based on tungsten absorber and silicon crystals (SICAL) is been installed with a higher acceptance than the previous one. Finally, a very small angle luminosity monitor (BCAL) is located after the final focus quadrupoles in order to provide an instantaneous measurement of the luminosity.

3.2.1 Tracking Detectors

Inner Tracking Detector

The inner tracking detector (ITC) is a cylindrical multiwire drift chamber composed of eight layers of sense wires parallel to the beam direction [30]. The active volume is a cylinder of 2 m length where the radial region varies from 16 cm to 26 cm. Inside this volume this chamber can provide up to eight coordinate points per track. The $r\phi$ coordinate is obtained by measuring the drift time, giving a precision of about 100 μm. The z coordinate is obtained by measuring the difference in the arrival times of the pulses at the two ends of each sense wire. The accuracy on this coordinate is 3 cm.

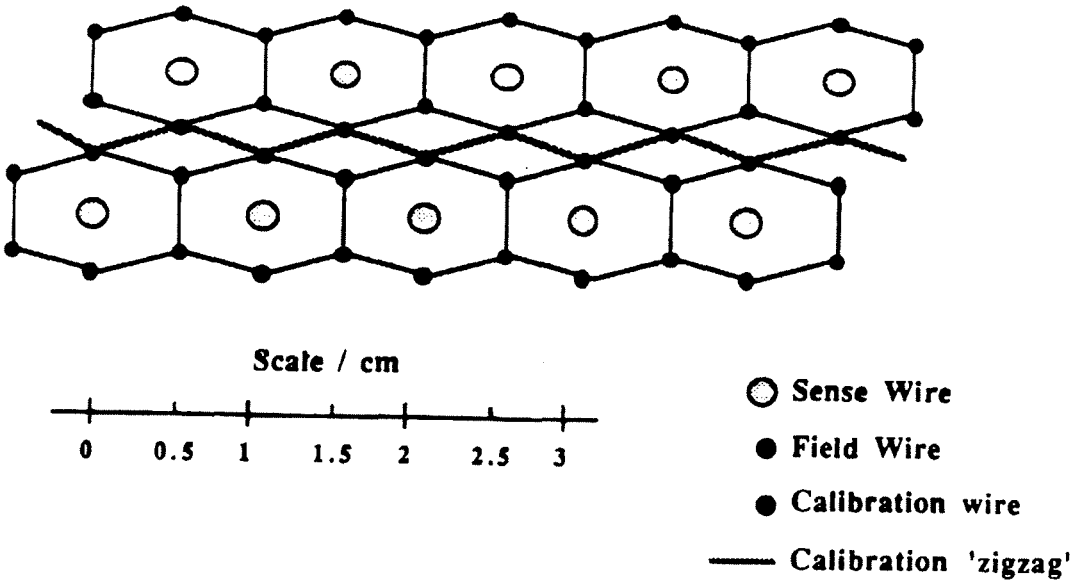

Figure 3.3: *ITC drift cells.*

The ITC drift cells have hexagonal shape, with a central sense wire surrounded by six field wires. The six field wires are held at earth potential, except one field wire per cell which is insulated from the end-plate where all the others are connected, in order to inject a calibration pulse when needed. Four of these field wires are shared by neighbouring cells in the same layer as can be seen in figure 3.3. The sense wire is operated at a positive potential in the range of 1.8 to 2.5 KV.

The size of the cells was kept small to reduce the drift time in order to give a fast signal to be used in the trigger. In addition, the cells in contiguous layers are offset by half a cell width, which is intended to help the left-right ambiguity in the track fitting.

The sense wires are directly connected to preamplifiers. The signal coming out from this preamplifier is the input for the main board which contains more amplifiers, discriminators and latches. The signal is amplified 36 times and discriminated. The discriminated output from one end of the chamber is connected to a time-to-digital converter module.

The signal from this time-to-digital converter is used to determine the drift time, which generates two $r\phi$ coordinates, one on each side of the anode wire. The

signals from both ends of the ITC go to a second time-to-digital converter. The time difference is used to measure the z coordinate. The ambiguity in $r\phi$ coordinates is solved at the tracking stage explained on the last section of this chapter.

This main board provides two signals for each wire used for the trigger processors. The first signal, a hit wire latch, is used to search for tracks in the radial patterns of wire cells. The second signal is a pulsed output which represents the z position of the hit. The trigger signal produced is available to the ALEPH trigger in less than 3 μs.

Time Projection Chamber

The time projection chamber (TPC) is a very large three dimensional imaging chamber, giving high precision measurements of tracks coordinates and dE/dx of charged particles. This detector consists of a large cylinder of 4.7 m length with an inner radius of 0.31 m and a outer radius of 1.8 m.

Inside this cylinder there are axial parallel magnetic and electric fields. The 11 kV/m electric drift field points from each end-plate towards the central membrane which is connected to a negative potential that divides the chamber into two halves. The TPC is filled with a a mixture of Argon and methane.

Charged particles crossing the TPC volume produce ionization. The resulting electrons are driven by the electric field toward the end-caps. When the electrons arrive at the end-plates they induce ionization avalanches in a plane of wire chambers. The measurement of the point where this second ionization takes place gives the $r\phi$ coordinate; whereas the time needed for the electrons to reach the end-plate gives the z coordinate.

The presence of a 1.5 T magnetic field produced by the superconducting solenoid surrounding the TPC causes the trajectory of a charged particle inside the TPC volume to have a helical form. The projection of a helix onto the end-plate is an arc of a circle. The measurement of the sagitta of this arc yields the curvature radius which is proportional to the component of the momentum perpendicular to the magnetic field. The large dimensions of the TPC were dictated by the goal of reaching 10% resolution in the transverse momentum for 100 GeV/c tracks.

The TPC has a large number of end-plate sectors, 18 on each side, as can be seen in figure 3.4. The zig-zag geometry of the sector boundaries reduces the number of

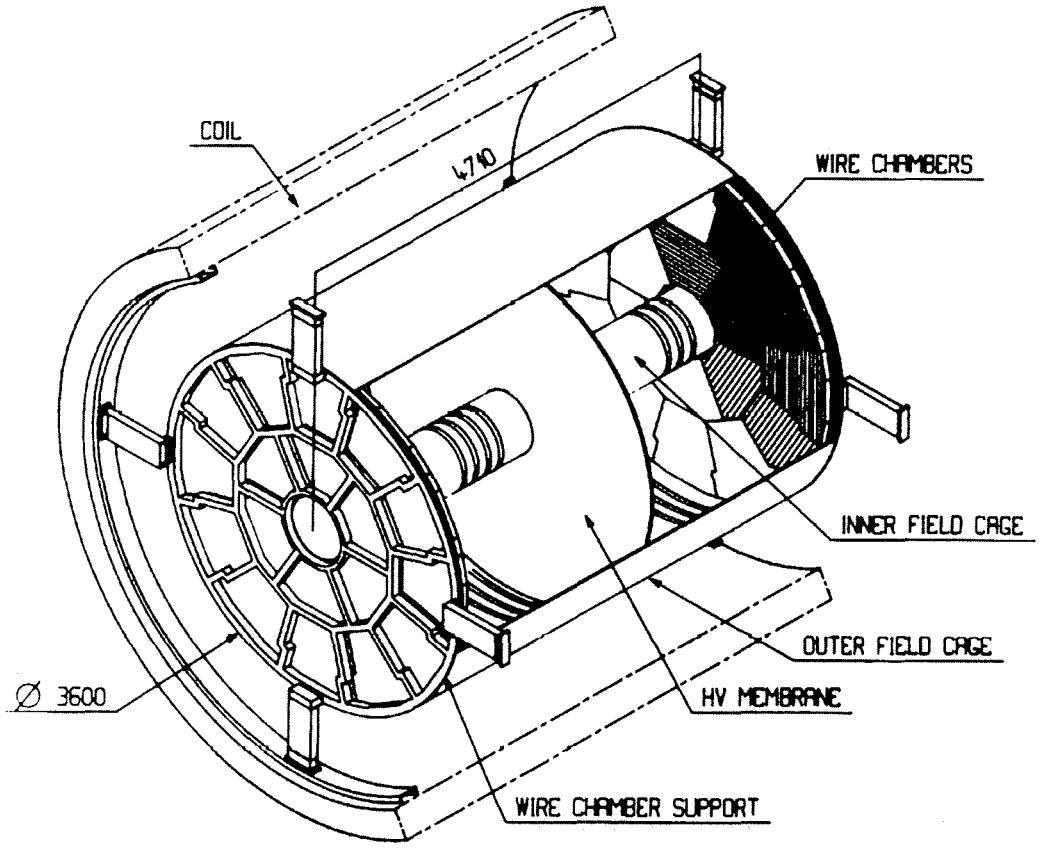

Figure 3.4: *View of the TPC.*

tracks not visible because they totally overlap with the dead region at the sector boundaries. There are three planes of wires on each chamber. Starting from the central membrane to the end-plates,

- the first layer has the function of gating grid,
- the second layer is the cathode plane, and
- the last wire plane contain sense wires interleaved with field wires.

This structure is shown in figure 3.5.

The cathode wires together with the central membrane create the electric drift field. The ionization avalanches created around the sense wires are read out by the signal induced on cathode pads at a distance of 4 mm from the sense wires. In addition, in the sectors there are long circular trigger pads from which a trigger signal is derived.

High precision in the alignment of each chamber with the others is required because each radial track is measured by 2 different wire chambers. The relative positions of the wires in the $r\phi$ plane within the sense/field grid are accurate to ± 0.02 mm. The overall positions in the $r\phi$ plane of the three grids with respect to the references on the pad plane are better than ± 0.1 mm. The pad positions have a tolerance of ± 0.02 mm relative to the reference marks on the chamber.

In the avalanches, positive ions are produced near the sense wires. If they enter in the drift volume, they can alter the drift field and cause track distortions. In order to avoid this, a gating wire grid was introduced. The gating grid has two possible states: open and closed. In the open state, a potential $V_g = -67\ V$ is placed on the gate wires, so that the gate is transparent to drifting charged particles. On the other hand, in the closed state, potentials $V_g \pm 40\ V$ are placed on alternate wires of the grid. The resulting dipole fields prevent the passage of positive ions. The gate is opened 3 μs before every beam crossing. If a positive trigger signal arrives, the gate is kept open, otherwise the gate is closed [31, 32].

The sense wires are read out to give the energy deposition dE/dx for particle identification. The dE/dx estimation is done by taking the mean of the smallest 60% of the 330 possible samples associated with a track. The resolution is found to be around 5% for electrons coming from hadronic events [33].

The $r\phi$ spatial resolution is affected by the diffusion of the drifted electrons, and it depends on the angles of the track with respect to the pads and wires. For low momenta, the effect of the angle between the track and the pads, the so-called angular pad effect, becomes dominant. The achieved $r\phi$ spatial resolution is around 200 μm [34].

The transverse momentum resolution of a track, with the maximum possible number of measured coordinates, that is 21, is given by

$$\frac{\Delta p}{p} = 10^{-3} p \left(\frac{\mathrm{GeV}}{\mathrm{c}}\right)^{-1} \left(\frac{<\sigma>}{150\mu\mathrm{m}}\right) \left(\frac{1.5\ \mathrm{T}}{B}\right) \oplus\ 0.003\ , \tag{3.1}$$

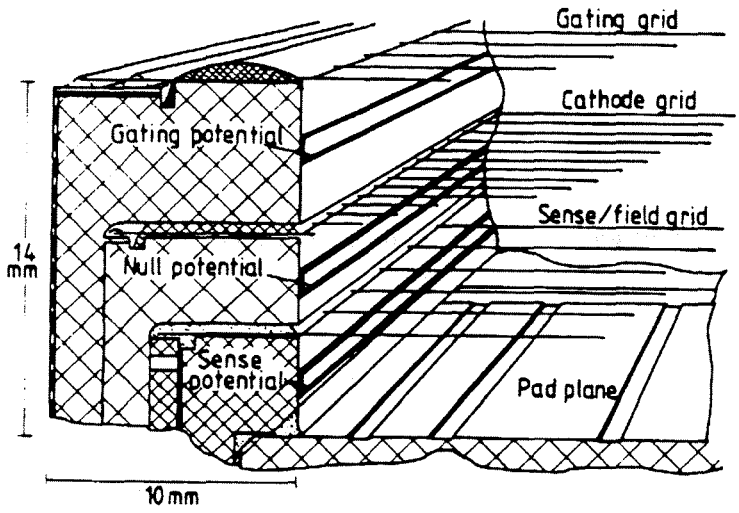

Figure 3.5: *View of a TPC wire chamber.*

where p is the transverse momentum, B the magnetic field, $< \sigma >$ is the average error on each $r\phi$ coordinate and the factor 0.003 takes into account the contribution of the multiple scattering in the gas of the chamber [35]. Owing to the angular pad effect, at low momenta, the momentum resolution is deteriorated. The momentum resolution for high momentum tracks having 21 TPC coordinates is

$$\frac{\Delta p}{p^2} = 1.2\ 10^{-3} \left(\frac{\mathrm{GeV}}{\mathrm{c}}\right)^{-1} . \tag{3.2}$$

The momentum resolution can be improved by using the measured coordinate points from ITC, TPC and silicon strip detector all together up to 0.6 $10^{-3}\mathrm{GeV/c}^{-1}$. The achieved resolution for the acollinearity angle ε in two track events is about 1.5 mrad.

In the case of the z component, the uncertainties come from the systematic differences in the transit time of the electronics, the length of cables, and the shaping time of the electronics. Also, the drift velocity needs a careful monitoring. The drift velocity is measured by mean of a laser system, which is based on the comparison of the reconstructed polar angles of the laser tracks with the deflection angles of the beam into the chamber. From the pad information, the error on the z coordinate

varies between 1 mm for tracks with a polar angle around 90°, and 2 mm when the polar angle is close to 20° or 160°.

Microvertex Detector

In 1991 a silicon microvertex detector was installed in ALEPH. The motivation for this detector is the measurement of multiple vertices for heavy quarks and leptons, but it also provides high precision measurement of charged tracks close to the interaction point and this complements the momentum measurement in the main tracking chambers.

The ALEPH minivertex detector is made out of two concentric barrels of double sided silicon microstrip detectors positioned around the beam pipe [36]. Each silicon wafer has read out strips parallel to the beam on one side and perpendicular to the beam on the other side. The resolution in $r\phi$ is 12 μm and in z is 10 μm.

3.2.2 Calorimeter Detectors

Electromagnetic calorimeter

The electromagnetic calorimeter (ECAL) is a sampling calorimeter of lead sheets and proportional wire chambers designed for measuring the energy and position of electromagnetic showers [37]. The electromagnetic calorimeter has three parts: a barrel and two end-caps as can be seen in figure 3.6. The barrel surrounds the TPC and is divided in twelve modules, each subtending 30° in azimuthal angle. The barrel is a cylinder 4.8 m long with an inner radius of 1.85 m and an outer radius of 2.35 m.

The entire barrel is rotated by about 2° with respect to the hadron calorimeter in order to avoid overlapping of crack regions. Each end-cap is 0.56m long with an inner radius of 0.54 m and 2.35 m for the outer radius. Each end-cap is divided in twelve modules. The barrel is closed at both ends with these end-caps.

The end-cap modules have a 15° rotation with respect to the barrel modules. The calorimeter is highly granular and with a good hermiticity: the cracks represent only 2% of the barrel and 6% in the end-caps. The energy and the position of the electromagnetic showers is measured using small (30×30 mm^2) cathode pads. The

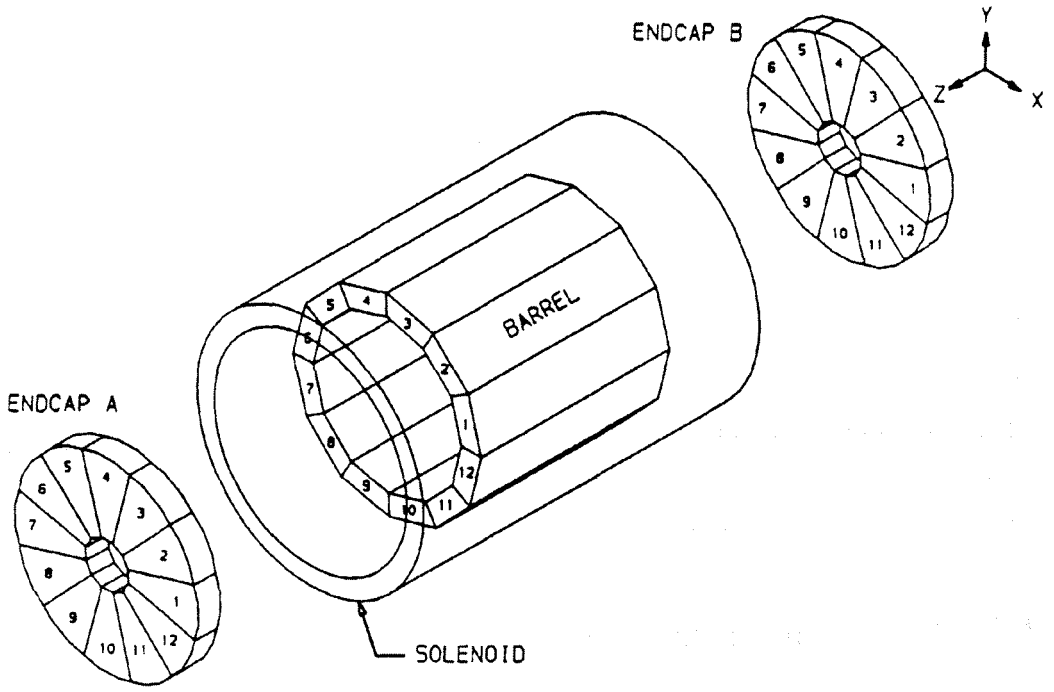

Figure 3.6: *View of the ECAL detector.*

cathode pads are connected internally to form towers pointing to the interaction point. Each tower is read out in three sections in depth, called storeys. Each module consists of 45 layers of lead and wire chambers. The structure of a single layer is shown in figure 3.7. It has 3 parts:

- a lead sheet of 0.2 cm (0.5 radiation lengths) thickness,
- a wire chamber plane (anode plane), which are made of aluminium extrusions,
- a pad plane (cathode plane).

In addition to the pads, all wires in a wire plane are read out together on a single channel. A barrel module, thus, contains 12288 pad channels but only 45 wire channels. The wire signals are used for calibrating the modules and for triggering. The energy resolution is measured to be

$$\frac{\sigma_E}{E} = \frac{18\%\ \mathrm{GeV}^{1/2}}{\sqrt{E}} \oplus 2\% \,. \tag{3.3}$$

The achieved position resolution is

$$\sigma_x = \sigma_y = \frac{6.8\ \mathrm{mm}\ \mathrm{GeV}^{1/2}}{\sqrt{E}} \,. \tag{3.4}$$

Pion-electron separation relies on the fact that the cluster structure is quite different in electromagnetic and hadronic showers [38]. Two estimators can be defined in order to separate electrons from pions. The first one compares the momentum measured by the TPC to the energy deposited in the four towers closest to the extrapolated track. The second estimator is a quantitative measure of how well the longitudinal shower profile matches with the longitudinal shower profile expected for an electron. The measured pion efficiency for an electron efficiency larger than 95% is of the order of 10^{-3} above 10 GeV.

Hadron calorimeter and streamer tubes

The hadron calorimeter (HCAL) is a sampling calorimeter of streamer tubes and iron sheets [39, 40]. The iron serves as the absorber part of the hadronic calorimeter and as the magnet return yoke. This calorimeter is composed of a barrel outside the superconducting coil and two end-caps. These structures are shown in figure 3.8. The barrel and each end-cap have twelve and six modules respectively. Each module consists of twenty-three layers of streamer tubes separated by 5 cm iron sheets. The total iron thickness of a module is 1.2 m, corresponding to 7 interaction lengths. On both sides of the tubes, pulses are induced in external electrodes. On one side copper pads are placed, which are summed in order to build up 4788 projective towers pointing to the interaction point. On the other side of the tubes, aluminium strips follow each individual tube. They provide a standard logic signal if a tube has been fired. Signals from these strips provide a two-dimensional view of the development of hadronic showers. This digital readout is very effective for

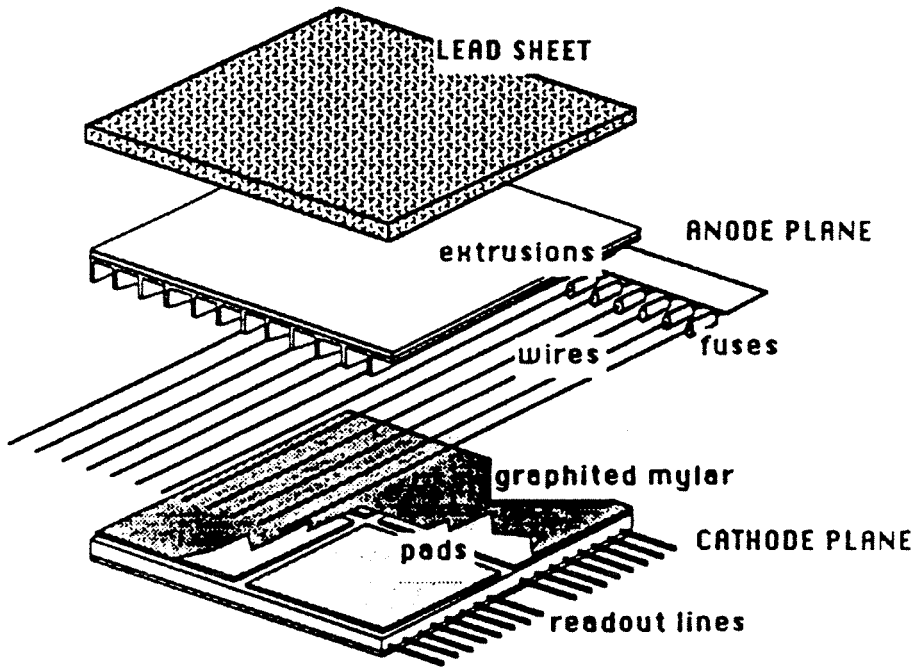

Figure 3.7: *View of an ECAL layer.*

identifying muons. This digital readout is also used for the level-1 trigger. The energy resolution of the hadronic calorimeter is given by

$$\frac{\sigma_E}{E} \equiv \frac{0.90 \text{ GeV}^{1/2}}{\sqrt{E}}, \tag{3.5}$$

with an angular resolution of 10 mrad for the polar angle for muons.

Outside this calorimeter structure are two additional double layers of streamer tubes; they serve as muon detectors. The muon chambers do not contribute to the measurement of the hadronic shower energy. They are used simply as tracking devices with two coordinates read out from each layer of tubes.

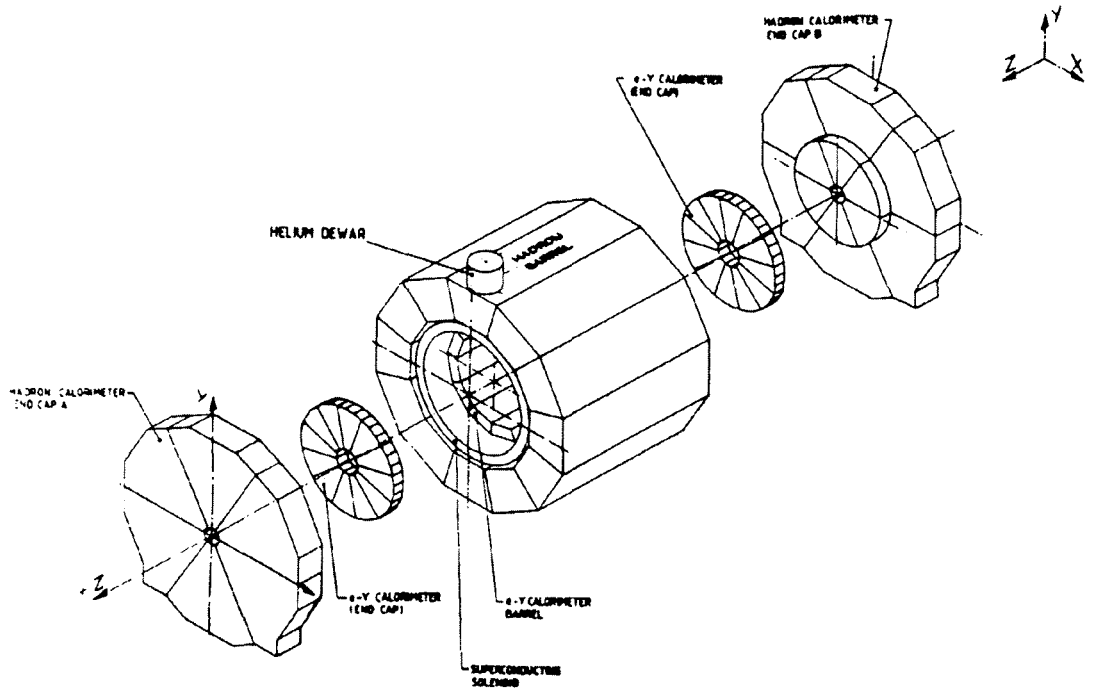

Figure 3.8: *View of the HCAL detector.*

3.2.3 Luminosity Detectors

The luminosity is determined from the rate of Bhabha events at small scattering angles. At the LEP energies, the cross section is well known from the quantum electrodynamic theory, and the interference of the γ and Z^0 is small for small angle. The Bhabha events are characterized by an electron and positron in coincidence on both sides of the interaction region with energies close to beam energy.

In ALEPH the main luminosity calorimeter (LCAL) is a sampling calorimeter of lead sheets and wire chambers located around the beam pipe on both sides of the interaction region. The LCAL detector is made of four semicylindrical modules.

The outer radius is 52 cm and the inner radius is 10 cm. The detector is placed at 2.7 m from the interaction point.

The total energy and the position of the electromagnetic shower are measured using small 30 mm square cathode pads. The cathode pads are connected internally to form towers pointing to the interaction point. Each tower is read out in three sections of depth. The energy resolution is around

$$\frac{\sigma}{E} = \frac{15\%\ \mathrm{GeV}^{1/2}}{\sqrt{E}} \oplus 11\% \,, \tag{3.6}$$

for wires and pads. The instrumental systematic error in the luminosity determination is found to be of the order of 0.2%.

In October 1992 a new luminosity calorimeter was installed in ALEPH [41]. This new detector consists of a compact cylindrical silicon-tungsten calorimeter (SICAL) mounted on each side of the interaction region, which extends the low angle acceptance for Bhabha events from 55 mrad down to 28 mrad. Each calorimeter is assembled from two half-modules enclosing the beam pipe, and consists of 12 tungsten sheets alternating with layers of silicon pads. The successive layers of silicon are rotated in the azimuthal angle by one-third of the pad size. This detector provides a gain in luminosity statistics of a factor close to 5, and the systematic error is significantly reduced, approximately to the order of 0.08% [42].

In order to provide a fast luminosity measurement, an additional Bhabha calorimeter (BCAL) is installed to detect Bhabha events at very small angle, between 5 and 9 mrad [43]. The system consists of four identical sampling calorimeters located symmetrically on each side of the beam pipe with respect to the horizontal (bending) plane of LEP, and on each side of the ALEPH interaction region. Each of the four calorimeters is made with tungsten converter sheets interspersed with 5 sampling layers made of plastic scintillator read out by photomultipliers, which provide information on the energy deposited in BCAL. In addition, a layer of silicon strips, located at a depth of 8 radiation lengths (near shower maximum for a 45 GeV shower), provides information on the point of entry of the particle in the front face of the calorimeter. This information is used to correct the energy measurement for lateral leakage of the shower. The BCAL calorimeter has turned out to be a useful tool for the LEP accelerator in the understanding of important machine effects.

3.3 Trigger and Data Acquisition System

The trigger system is designed to activate the read out of the whole detector for all possible Z^0 candidate events, without bias or preference in the events, and to keep signals from possible new physics events, while reducing the background to an acceptable level. In ALEPH there is an additional requirement that the trigger frequency must be small enough in order to have the gating of the TPC working efficiently and causing the smallest possible dead-time. The background is mainly due to beam-gas interactions and off-momentum beam particles hitting the beam pipe or the detector itself.

The basic design of the trigger is to exploit different detector signals and to provide a fast decision on single particles or jets. The ALEPH trigger system is based on three levels of refinement.

- Level-1 trigger: A decision is taken within 5 μs after the beam crossing. The information to make the decision is taken from pads and wires from the electromagnetic and hadron calorimeters, and from the hit pattern of the ITC. In addition, LCAL tower signals or SICAL pads are used to trigger on Bhabha events in order to monitor the e^+e^- collision rate. The level-1 trigger rate must not exceed a few hundred Hz.

- Level-2 trigger: A decision is made within 50 μs at most. The level-2 trigger refines the level-1 trigger by looking at the TPC sector information which is pointed to the ITC track. In case that the level-2 trigger does not confirm the trigger, then this decision is broadcast to all subdetectors. The level-2 trigger rate is around 10 Hz.

- Level-3 trigger: This decision is software driven. The level-3 trigger has access to the information that comes from all subdetectors. The aim of this trigger is to reject the background events that have been triggered. If the level-3 trigger validates the previous levels, the event is recorded on storage medium. A typical trigger rate at this level is around 1-2 Hz.

The trigger efficiency for hadronic, leptonic and luminosity events have been estimated to be at the 100% level in the acceptance region of the detector.

Data Acquisition System

The modular structure of ALEPH motivates as well a modular structure of the data acquisition system [44, 45, 46]. In other words, each subdetector has some independence to take data and to perform in parallel other activities such as calibration or data consistency checks. The architecture of the data acquisition system is tree-like with a strong hierarchy, implemented with FASTBUS.

Synchronized with the beam crossing by the Timing Module, the data acquisition activates the trigger system and the read out of the data from the different components of the detector. Every subdetector has an associated microprocessor to build its subevent. A main processor collects the pieces of an event from the microprocessors, ensuring resynchronization and completeness. This main processor sends the event to the level-3 event processor [47, 48]. After this step, the events are written on disk in the main computer system.

3.4 Event Reconstruction and Simulation

Due to the large rate of events and their size, a large amount of computing is needed. The Facility for ALEPH reCONstruction (FALCON) is a dedicated computer system designed to perform online event reconstruction of the data. This computer system consists of two microVAXes that act as servers, twelve diskless VAX stations and three dual-ported disks [49]. One disk port is connected to FALCON whilst the second port is connected to the data acquisition computers. The disks, that contain the data, are alternatively mounted on both systems under software control. The twelve stations run a subsets of events over the reconstruction program in parallel. The raw data files written on disk by the data acquisition system are reconstructed by FALCON within a few hours after having been taken. The reconstructed data is transmitted to the CERN computer centre and is stored on tape.

The ALEPH reconstruction program, JULIA, uses all the information coming from the subdetectors. It reconstructs coordinates in the tracking chambers into charged particle trajectories. For the calorimeters, neighbouring towers which contain energy are joined into clusters. These clusters are associated with charged tracks if possible. Finally, a count of the Bhabha events is also given as a preliminary luminosity estimate.

For this thesis, Monte Carlo simulated events for different processes have been used to evaluate the background contaminations, efficiencies, detector effects and other corrections. The following steps are needed to produce Monte Carlo events, which are included in the ALEPH simulation program (GALEPH) [50].

- The generation of the event kinematics according to the physics processes. The processes needed for this analysis are
  - $e^+e^- \longrightarrow \tau^+\tau^-$ (KORALZ generator [51, 52]).
  - $e^+e^- \longrightarrow \mu^+\mu^-$ (KORALZ generator).
  - $e^+e^- \longrightarrow e^+e^-$ (BABAMC generator [53], [54]).
  - $e^+e^- \longrightarrow q\,\bar{q}$ (LUND generator [55]).
  - $e^+e^- \longrightarrow l^+l^-(l^+l^-)$ (PHOPHO generator [56], [57]).
- The materials and geometries of the different subdetectors are described through the GEANT package [58]. The trajectory inside the detector and the generation of secondary particles are described by means of the GEANT and GHEISHA [59] packages.
- Finally, the conversion of energy or charge deposition into measurable signals for all subdetectors is also simulated.

The output of the GALEPH program uses the same conventions and formats that the real data uses. The last step in the chain generation consists of using the reconstruction program (JULIA) for this simulated data.

3.5 Charged Track Reconstruction

In this thesis, the acollinearity distribution is used to extract the couplings, and for this reason the explanation of the process taking place between the signals coming from the detectors and the reconstructed tracks is expanded. On the other hand, this discussion will also help to understand the systematics entering in the angular measurements which are given in chapter 6.

In the TPC, as mentioned in a previous section, from the cathode pads the three dimensional coordinates are measured whilst from the sense wires the data is used

for particle identification by dE/dx [60, 61]. The raw data for pads are composed of pad number, pulse length, arrival time of the pulse, so-called all together 'hit data', and the pulse-height per time-slice (also called buckets or samples). A pulse is defined in a pad-row when a signal starts above a certain threshold in a bucket and finish at a certain number of buckets later.

The first step in finding the coordinates is the recognition of two dimensional ϕ - z clusters in each TPC pad row. Starting with one pulse, another pulse on an adjacent pad is included if it overlaps the first by at least one sample. The second step consists of separating inside each cluster the possible contributions from different particles, using the pulse-height information. Looking for peaks that are sufficiently isolated, subpulses are tagged. In this way, a group of subpulses on adjacent pads that are aligned with respect to time are grouped in subclusters. From each subcluster a three dimensional coordinate is inferred. The $r\phi$ coordinate is determined by using a Gaussian model of the pad response if only few pads are involved. Otherwise a charge-weighted average of the pad positions is used. Such a case occurs for low momenta particles, and increases the coordinate error. The z coordinate is calculated from a charge-weighted average of the time estimates of the subpulses. At this point, the coordinates are corrected for misalignment or distortions of the drift field.

From the established set of TPC coordinates, a search is done for those coordinates that are consistent with a segment of a helix with less than π radians [62]. Segments that are determined to belong to the same helix are linked together as a single TPC track candidate. Five helix parameters are determined by a fit to the coordinates within the first half turn of each track candidate. The five helix parameter are chosen to be:

ω = inverse radius of curvature,

$\tan\lambda$ = tangent of the dip angle, $\theta = \lambda - \frac{\pi}{2}$,

ϕ_0 = emission angle in the x, y plane at the point of closest approach to the z axis,

d_0 = impact parameter in the x, y plane,

z_0 = z coordinate at $x^2 + y^2 = d_0^2$.

The TPC trajectories are projected back into the ITC and a search is made to find possible ITC coordinates within a road in $r\phi$ and z. If no suitable ITC coordinate is found in the 2 outer layers of the ITC for a given TPC track, then the search is stopped. Otherwise, if more than three ITC coordinates are found for a TPC track a fit is performed, and the resulting ITC track is accepted if the χ^2 of the fit lies inside a certain range. In the final fit of the tracks, the multiple scattering of the particles is taken into account.

Given the resolutions in section 3.2.1 for the $r\phi$ and z coordinates in the TPC for a track with 21 z measurements and polar angle close to 90°, the expected statistical error for λ and ϕ resolutions inside the TPC are found to be given by

$$\Delta \tan\lambda \approx 6 \cdot 10^{-4} \tag{3.7}$$

$$\Delta\phi \approx 4 \cdot 10^{-4} \ . \tag{3.8}$$

In the expressions 3.7 and 3.8 is necessary to add in quadrature the expected error $\Delta\Psi_{space}$ from multiple scattering given by

$$\Delta\Psi_{space} \approx \frac{13.6 \text{ MeV}}{p}\sqrt{\frac{0.06}{\sin\theta_{track}}} \ . \tag{3.9}$$

Chapter 4

Selection of events

Tau candidates are selected by retaining low-multiplicity events coming mainly from lepton-pair decays of the Z^0. After association of the charged particles and photons with one of the two hemispheres in the event, as defined by the event thrust axis, the identity of the charged particles and the presence of photons and/or π^0s determine the tau decay classification. The removal of non-tau background based on the kinematics of the opposite hemisphere largely avoids kinematic biases and loss of sensitivity, except for the energy correlations between hemispheres. A typical tau event is shown in figure 4.1.

The selection consists of three main parts. First of all, a preselection of the events is performed, as described in section 4.1. Secondly, the track type of each track is identified. The method used for the particle identification is described in section 4.2. Finally, the tau channel identification is done by defining the cuts for the signal and the cuts to reject all sources of background, which are given in section 4.3.

4.1 Preselection

The events are required to pass a preselection criteria by requiring that

- there exist at least 2 and at most 8 good charged tracks as defined below,
- the momentum of at least one track must exceed 3 GeV,

- the thrust axis is calculated from the good charged tracks, and the event is divided into two hemispheres. The cosine of the maximum opening angle of all tracks with respect to the thrust axis must be larger than 0.85 in each hemisphere.
- The absolute value of the cosine of the thrust axis polar angle must be smaller than 0.9,
- there exist at most 4 bad tracks also defined below,
- the data acquisition flag must indicates no problem in the readout of the event.

A good track in the above definition must have

- at least 4 TPC hits,
- $|\cos\theta| < 0.95$,
- the distance of the closest approach to the beam axis ($|d_0|$) must be smaller than 2 cm, and
- the z coordinate at the point of closest approach to the beam axis ($|z_0|$) must be smaller than 5 cm.

On the other hand, a track is called a "bad track" if

- it has at least 3 TPC hits,
- the $|d_0|$ is smaller than 20 cm, and
- the $|z_0|$ is smaller than 40 cm,
- it is not found to be a good track.

The main source of bad tracks are tracks produced by photon conversions, nuclear interactions or cosmic rays. Tracks with only ITC hits or from calorimeter backsplash tend not to pass either criteria.

With this preselection, most of the Z^0 decays to hadrons are excluded by the cut that requires fewer than nine tracks coming from the interaction region and

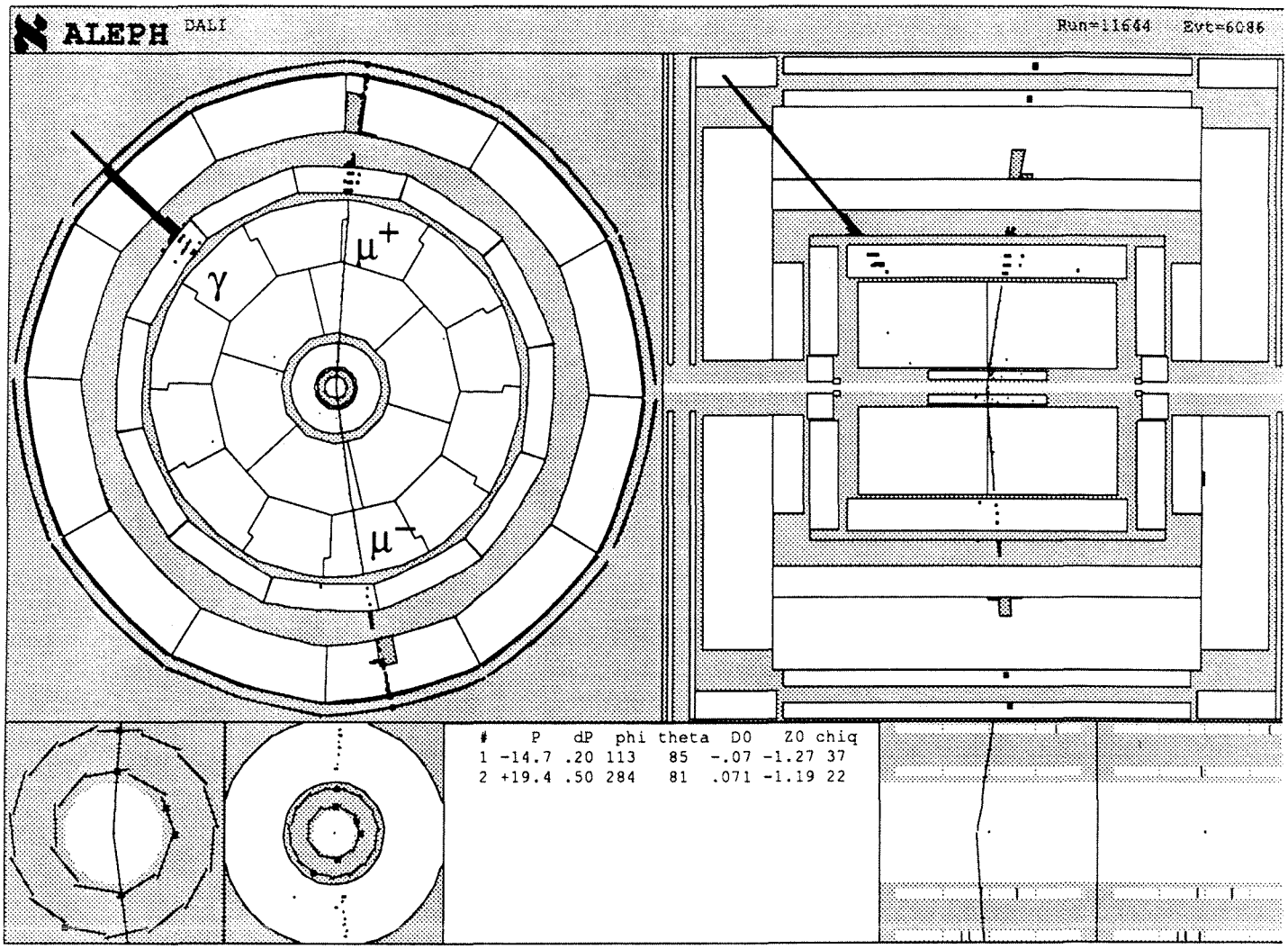

Figure 4.1: *Typical tau event as seen in the ALEPH detector. In this particular event the negative tau decays to a muon and the positive tau decays to a muon with a radiative photon. The minivertex and ITC hits are drawn in the xy projection, respectively, at the lower left corner, whereas in the zy projection are shown at the lower right corner.*

that tracks have an angle with respect to the axis of the jet such that its cosine is larger than 0.85. Most two-photon events are excluded by demanding at least two charged tracks, and at least one track with momentum above 3 GeV, because the energetic scattered electron and positron escape through the beam pipe. The cut

on the thrust axis polar angle avoids Bhabha background and poorly reconstructed tracks.

The remaining sample of events after this preselection consists of Bhabha events, muon pairs and tau pairs with low multiplicity [63]. This event preselection retains 84% of the tau events produced, and 99% of those within the angular acceptance.

4.2 Particle Identification

For charged particle identification a neural network algorithm is employed. The particle identification neural network uses simultaneously the information from the tracking and calorimeter devices. The neural network input uses the available information from the TPC, ITC, ECAL, HCAL and muon chambers for all the good and bad tracks. The output for a charged track consists of being identified exclusively as electron, muon or pion.

This neural network has benefited from a pattern recognition algorithm (HARBOR) to improve the muon, pion and electron separation [64]. The digital pattern of the calorimeter tubes from HCAL is significantly different for muons, pions and electrons, but it suffers from noise, dead zones and inefficiencies. This algorithm overcomes these problems by first constructing segments between signals from tubes which are close in distance and angle, which reduces the noise problem. Looking for possible extrapolations of the segments and constructing an outgoing tree reduces the inefficiency and dead zones problems.

The input quantities associated to each track are

- from the tracking detectors: track momentum, polar and azimuthal angle and dE/dx estimator for electron and pion hypothesis.
- from the electromagnetic calorimeter: the ratio of the total ECAL cluster energy to the associated TPC track momentum, the ratios in each ECAL storey of the energy in the four towers nearest the extrapolated track to the total ECAL cluster energy, and the fraction of the track trajectory in ECAL spent within 4 cm of an ECAL crack.
- from the hadronic calorimeter: the number of HARBOR trees associated to a track; the length, distance, energy and angle of the closest HARBOR tree

to the track. The sum of residuals for a fit of the main branch, the angular dispersion and the ratio of energy to length of the main tree are also used [64].

- from muon chambers: the inner and outer layer hit estimator.

The neural network used for this particle identification has a layered structure of "neurons" having scalar numerical values [65, 66]. The neural net has an input layer of neurons where each neuron correspond to an input variable, two hidden layers of ten neurons, and an output layer consisting of three neurons. The nodes in each layer connect to each of the nodes in the next layer by weights. The value of neuron j in the layer h is given by

$$h_j = \frac{1}{2} \tanh \left(\sum_{i=1} w_{ij} x_i + T_j \right) , \tag{4.1}$$

where x_i is the value of the neuron in the previous layer, w_{ij} is the weight, and T_j is a threshold. A neural network must be trained, which means that values for the weights and thresholds must be found which minimize the error in the output layer values [67, 68].

	Sources of Monte Carlo particles				
track ID	$\tau \to e\nu\overline{\nu}$	$\tau \to \mu\nu\overline{\nu}$	$\tau \to \pi\nu$	$Z^0 \to e^+e^-$	$Z^0 \to \mu^+\mu^-$
e	98.9±0.1	-	1.4±0.1	98.4±0.1	-
μ	-	99.2±0.1	1.2±0.1	-	99.5±0.1
π	1.1±0.1	0.8±0.1	97.4±0.1	1.6±0.1	0.5±0.1

Table 4.1: *Efficiency (in percent) of the neural network particle identification method, for tracks with p/E_{beam} above 0.05 and $|\cos\theta| < 0.9$ from Monte Carlo lepton pair events. The fiducial region includes the cracks between calorimeter modules.*

The neural net has been trained with a Monte Carlo sample of 26000 pions, 10700 muons and 18600 electrons. Table 4.1 shows the efficiency of the neural network for Monte Carlo events with momenta above 3 GeV. The behaviour of the neural network with momenta below 3 GeV shows slightly higher efficiency for electrons, which is relevant of the reconstruction of electrons from photon conversions;

however, the situation is worse for muons since they tend not to penetrate the whole HCAL and are more often confused with pions.

Compared to analyses based on cuts, in the crack and overlap regions of the detector the neural network has the advantage of providing additional acceptance for electrons. In the muon channel, the background has been reduced to a very low level due to the use of the information of the electromagnetic calorimeter.

4.3 Channel Classification

As explained in section 4.4 below, only the $\tau \to e\nu_e\nu_\tau$, $\tau \to \mu\nu_\mu\nu_\tau$ and $\tau \to \pi\nu_\tau$ channel classifications are required for the analysis presented in this thesis. In the next subsections the specific cuts used to identify the tau decay channels and to reduce the non tau-background significantly and the tau background somewhat are explained.

As the event is divided in two hemispheres and all the good charged tracks are identified as electron, muon or pion; the presence of one charged track identified in one hemisphere as an electron indicates a $\tau \to e\nu_e\nu_\tau$ decay, whereas the identification in one hemisphere of a charged track as a muon indicates a $\tau \to \mu\nu_\mu\nu_\tau$ decay. However, the remaining backgrounds, from $e^+e^- \longrightarrow e^+e^-$, $e^+e^- \longrightarrow \mu^+\mu^-$ or to two photon dilepton production, can be greatly reduced by imposing restrictions on the track type, energy, and angle of the recoil hemisphere. In the case of a charged track identified as a pion in one hemisphere, a closer look to this hemisphere is necessary to reject mainly $\tau \longrightarrow \rho\nu$ and $\tau \longrightarrow a_1\nu$ which can also give single charged pions.

In order to reduce the Bhabha background, events with one electron identified by the particle identification on both sides are rejected. To reduce the background due to $Z^0 \longrightarrow \mu^+\mu^-$ events, events with one muon in each hemisphere are kept only if the visible energy is significantly less than the center-of-mass energy. As tracks from Bhabha and muon pair events sometimes are misidentified as pions, events are rejected if in the recoil hemisphere there is an electron or muon with a large fraction of the beam energy. The remaining two-photon events are rejected by requiring a minimum energy in both hemispheres when there is either one electron or one muon in both sides.

Many tools have been developed in ALEPH to work with tau final states. In particular one needs an efficient photon reconstruction algorithm, since photons are present in many tau final states. The photon reconstruction algorithm (GAMPEK [69]) is used to separate photons from charged tracks, "fake" photons and overlapping photon pairs. The algorithm starts by looking for local energy maxima, that is, storeys that have an energy higher than the neighbours with which they share a face. Then each storey is assigned to the cluster of its neighbour of maximal energy. The energy of the photon is computed from the energy of the four central towers. The angle of the photons with respect to the thrust axis determines the hemisphere to which they are assigned.

Fake photons may appear because a charged track has produced small satellite clusters. In order to distinguish between genuine and fake photons, the former are required to have a minimum total energy of 400 MeV, such that the two first stacks of ECAL have energy and the ratio of their sum to the total energy is higher than 70%. In addition, to separate photons from charged tracks, the minimal distance between the extrapolated track through the calorimeter and the barycenter of the photon must be larger than 5 cm.

The algorithm QPAIRF [70] is used to identify photons which convert to electron-positron pairs in the detector material by selecting all oppositely charged track pairs in which at least one track is identified as an electron by the neural net and the invariant mass of both tracks is smaller than 15 MeV. In addition, there is the requirement that the two tracks have to pass close together at a certain radius away from the interaction point. If such a photon is found then the criteria for fake or genuine photon explained above is applied to it.

The identification of neutral pion is also crucial for the separation of several tau decay channels (mainly π, $\rho \rightarrow \pi\pi^0$ and $a_1 \rightarrow \pi\pi^0\pi^0$). However, due to the semi-inclusive categories defined in section 4.4, this identification only becomes important for the pion channel. A neutral pion reconstructed from two distinct photons is defined by a cut on the invariant mass: $0.08 < m_{\gamma\gamma} < 0.23$ GeV.

From now on, only events with one good track on each hemisphere and with opposite charges are kept for the electron, muon and pion channel identification.

4.3.1 Electron Channel Classification

The electron channel is classified with the following requirements:

- there is exactly one track identified as an electron in the hemisphere,
- the electron energy is smaller than the beam energy, where the electron energy is the sum of the ECAL cluster energy, or its energy estimated from the TPC when it passes within 4.5 cm of an ECAL crack, plus the energy of all the reconstructed photons in the hemisphere,
- there are at most 2 photons and no π^0 in the hemisphere,
- the HCAL energy over the momentum is smaller than 0.2 for tracks which do not go into a ECAL crack, i.e. the track passes at least at 4.5 cm from the edge of the second stack in ECAL.

However the electron is not accepted if any of the following criteria is true:

- the recoil track in the opposite hemisphere is identified as an electron,
- the recoil track is not a muon and it goes into an ECAL crack,
- the recoil track is not a muon and the ECAL energy in the recoil hemisphere is larger than 75% of the beam energy,
- the energies of the tracks in both hemispheres are each less than 5 GeV.

4.3.2 Muon Channel Classification

The muon channel is classified with the following requirements:

- there is exactly one track in the hemisphere identified as a muon,
- the TPC momentum is smaller the beam energy,
- the TPC momentum is larger than 2 GeV for 1990 data (3 GeV for 1991 data),
- there are at most 2 photons and no π^0 in the hemisphere,

- there are associated muon chamber hits, when there are photons in the hemisphere.

However the muon is not accepted if any of the following criteria is true:

- the recoil track is a muon, and the total energy in the hemisphere (track + photons) is larger than 65% of the beam energy in both hemispheres,
- the recoil track is a pion, and the total energy in the hemisphere is larger than 90% of the beam energy in both hemispheres,
- the recoil track is not an electron, and the sum of the momenta in both hemispheres is smaller than 40 GeV and its difference smaller than $\varepsilon/4$ GeV, where ε is the acollinearity angle,
- the recoil track is a muon, and the sum of the momenta in both hemispheres is smaller than 30 GeV and its difference smaller than 10 GeV and the $|\cos\theta_{thrust}| > 0.8$,
- the energy of each track in both hemispheres is less than 6 GeV.

4.3.3 Pion Channel Classification

The pion channel is classified with the following requirements:

- there is only one track in the hemisphere identified as an pion,
- the TPC momentum is smaller than the beam energy,
- the measured momentum in the TPC is larger than 2 GeV,
- there are no converted photons and no π^0 in the hemisphere,
- for tracks going to ECAL cracks the dE/dx estimator must be within 1.5 sigma deviation of what it would be for a pion,
- the ECAL energy is less than the TPC momentum, and the total calorimeter energy is less than twice the TPC momentum,
- there are no genuine photons, and no fake photons of more than 5 GeV.

However the pion is not accepted if any of the following criteria is true:

- the recoil TPC momentum over the beam energy is at least 0.88 and the total recoil calorimeter energy over recoil TPC momentum is smaller than 0.3,
- the momentum of the fastest track over the beam energy is smaller than 0.2 in each hemisphere,
- if the pion goes into a ECAL crack, and the momentum of the recoil track over the beam energy is larger than 0.5, and the ECAL energy for the recoil track over the beam energy is larger than 0.8,
- the recoil track is an electron and, either the recoil ECAL energy over the beam energy is larger than 0.9, or the pion has a momentum larger than 20 GeV with $|\cos\theta| > 0.7$ and the HCAL energy is smaller than 2 GeV,
- if the recoil track is a muon, and the momentum of the pion over the beam energy is larger than 0.45, and the sum of the energies in both hemispheres including the energy of the photons in the recoil side is larger than 82 GeV.

decay channel	$e\nu\overline{\nu}$	$\mu\nu\overline{\nu}$	$\pi\nu$
acceptance (%)	48	70	61
tau background (%)	1.9	1.3	7.0
non-tau background (%)	1.1	1.1	1.5

Table 4.2: *Performance of channel classification and background rejection.*

The overall efficiencies and backgrounds for $\tau \to e\nu_e\nu_\tau$, $\tau \to \mu\nu_\mu\nu_\tau$ and $\tau \to \pi\nu_\tau$ are shown in table 4.2. It is important to notice that those efficiencies are considerably higher than the previous values published by ALEPH in [71]. The improvements are also noticeable for the reduced amount of backgrounds in the electron and muon channel decays.

4.4 Semi-Inclusive Categories

The efficiency for identifying tau final states is typically around $50 - 70\%$ for $\tau \to e\nu_e\nu_\tau$ and $\tau \to \mu\nu_\mu\nu_\tau$ and 60% for $\tau \to \pi\nu_\tau$. Thus, the requirement of identification

of the final state of the two taus considerably reduces the statistics of the sample. In addition the branching ratios are also typically low. For instance, in the case where both taus decay to a single pion,

$$Br^2(\tau \to \pi\nu_\tau) \times \text{Efficiency}|^2_\pi \sim 0.36\ \% .$$

For the data collected in 1990 and 1991, corresponding to 16000 observed tau pair events, this results in 58 events of the class $\pi - \pi$.

In order to avoid the identification of the two exclusive final states, "inclusive" categories are introduced. The motivation is that, once the mass of the particle on one side is fixed, the acollinearity distribution (governed by the Q functions of equation 2.61) does not depend strongly on the mass of the tau decay product on the other side. The Q functions of the different exclusive channels going into the inclusive category defined below have a similar shape, thus not inducing a loss of sensitivity.

Possible inclusive categories are:

- inclusive pion: where in one hemisphere one tau decays as $\tau \to \pi\nu_\tau$ and in the other hemisphere the tau decays as $\tau \to \pi\nu_\tau$, $\tau \to e\nu_e\nu_\tau$, $\tau \to \mu\nu_\mu\nu_\tau$, $\tau \to \rho\nu_\tau$ or $\tau \to a_1\nu_\tau$.
- inclusive lepton: where in one hemisphere one tau decays as $\tau \to l\nu_l\nu_\tau$ (l = electron, muon) and in the other hemisphere the tau decays as $\tau \to e\nu_e\nu_\tau$, $\tau \to \mu\nu_\mu\nu_\tau$, $\tau \to \rho\nu_\tau$ or $\tau \to a_1\nu_\tau$.
- inclusive hadron: where in one hemisphere one tau decays as $\tau \to \rho\nu_\tau$ or $\tau \to a_1\nu_\tau$, and in the other hemisphere the tau decays as $\tau \to \rho\nu_\tau$ or $\tau \to a_1\nu_\tau$.

The inclusive pion and the inclusive lepton categories are used in this analysis. The inclusive hadron category has less statistical sensitivity and larger background and systematic uncertainties, and is thus not studied further.

4.5 Acollinearity Event Classification

The acollinearity analysis uses only events where both taus decay into one charged track and the polar angles θ for those tracks satisfies $|\cos\theta| < 0.9$. The charged

tracks are identified, and the decay channel classified according to the description in section 4.3.

The events are therefore classified into two categories, called the

- $\pi - X$, or "inclusive pion": at least one hemisphere is classified as $\tau \to \pi\nu$, and there is no additional restriction on the other tau hemisphere
- $l - X$ or "inclusive lepton": at least one hemisphere is classified as $\tau \to e\nu\overline{\nu}$ or $\tau \to \mu\nu\overline{\nu}$, and neither hemisphere is classified as $\tau \to \pi\nu$ in order to avoid double counting.

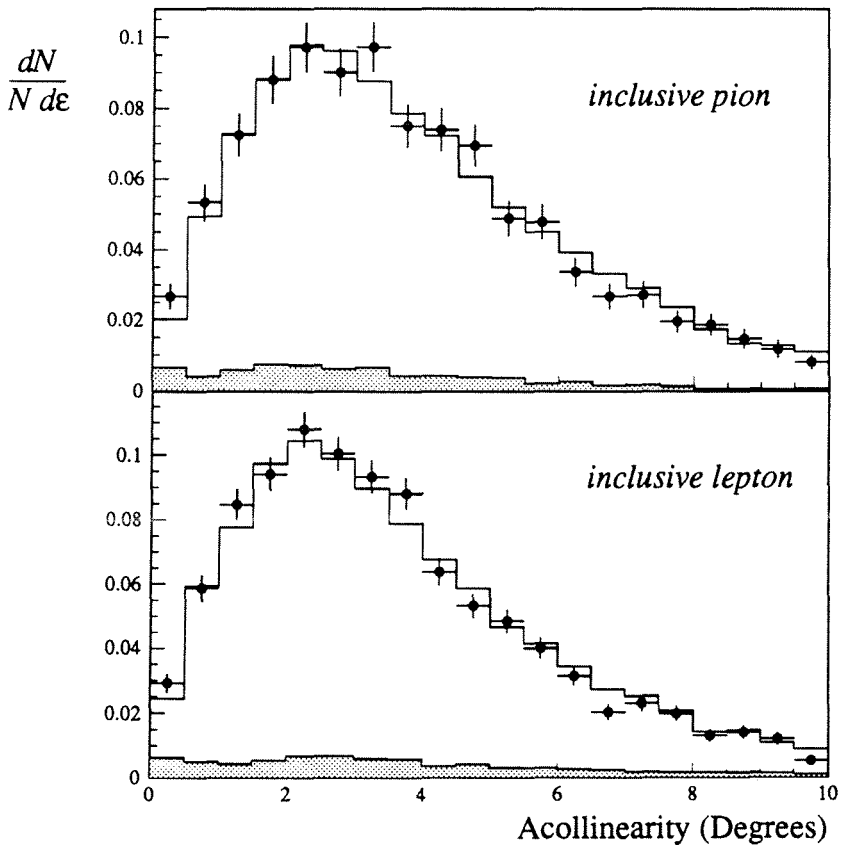

Figure 4.2: *Acollinearity distributions for the selected events in both samples. The points with error bars are the data. The solid curves are the Monte Carlo prediction. The coloured areas correspond to the total expected background.*

The analysis described employs the tau decay modes $e\nu\overline{\nu}$, $\mu\nu\overline{\nu}$, $\pi\nu$, $\rho\nu$, and $a_1\nu$, together constituting more than 75% of all tau decays. In the $a_1\nu$ decay only $a_1 \rightarrow \pi\pi^0\pi^0$ is considered. Charged pions are not distinguished from kaons in the data, however, the K^* decays are treated as background. The decay modes $\tau \rightarrow \pi\nu$ and $\tau \rightarrow K\nu$ are treated together and referred to herein as "$\pi\nu$".

The candidate events correspond to the data collected in ALEPH in the years 1990 and 1991 within 150 MeV of the Z^0 peak, where the total integrated luminosity was 11.2 pb^{-1}, as shown in table 4.3.

year	Energy (GeV)	Int. Luminosity (nb^{-1})
1990	91.215	3652
1991	91.238	4609
1991	91.207	2937

Table 4.3: *Integrated luminosities per year and mean energy for data sets.*

The overall acceptances and backgrounds of this selection, estimated from Monte Carlo simulation, appear in table 4.4.

The acollinearity distributions for the selected events in the data for both samples are shown in figure 4.2, together with the predictions from the Monte Carlo simulation. A good agreement is found over the whole range of acollinearities.

item	$\pi - X$	$l - X$
candidate events	1987	3699
acceptance (%)	60	55
tau background	6.4	6.2
non-tau background	0.9	0.9

Table 4.4: *Summary of the efficiencies and backgrounds (in percent) for the selected acollinearity sample.*

The tau background in the inclusive lepton class is higher than the background

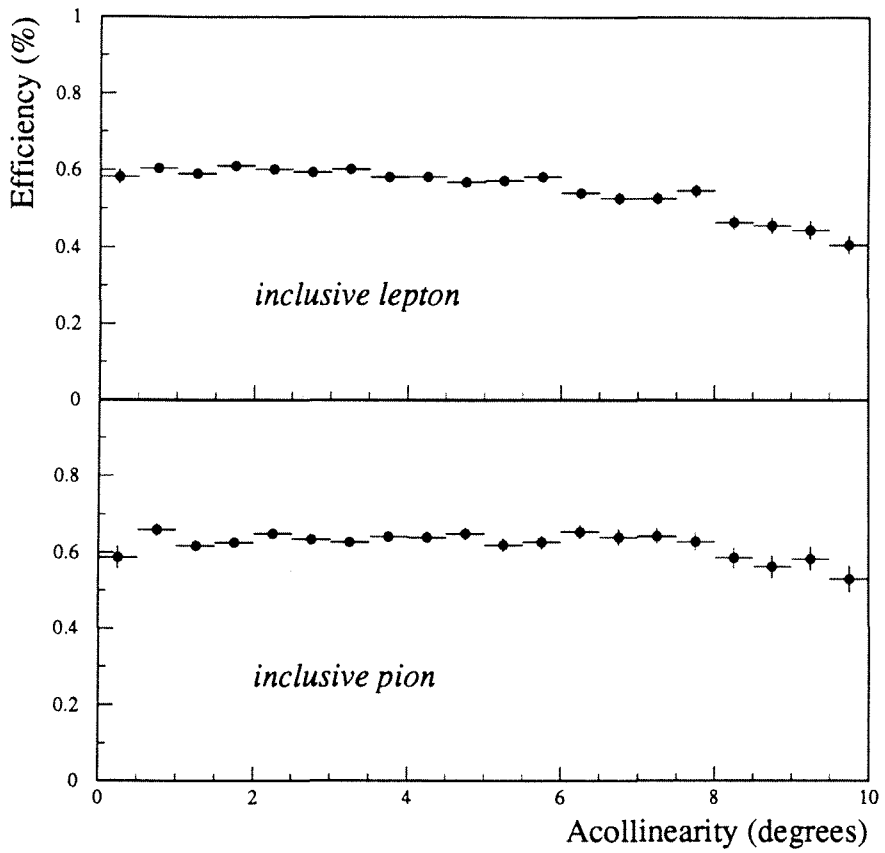

Figure 4.3: *Efficiencies as a function of the acollinearity angle for inclusive pions and leptons.*

for $\tau \to e\nu_e\nu_\tau$ and $\tau \to \mu\nu_\mu\nu_\tau$ shown in table 4.2 because there are pion versus lepton events where the pion is not identified but the lepton is. According to the inclusive lepton classification, where in the recoil side a $\tau \to \pi\nu_\tau$ decay is not allowed, these events are considered to be background. The non-tau background comes mainly from Bhabha events and from muon pair events identified as pions. The hadronic background is found to be completely negligible.

The efficiencies and the tau backgrounds as a function of the acollinearity distributions are shown in figures 4.3 and 4.4, respectively. These efficiencies are not flat for high values for the acollinearity. This is due to the fact that high acollinearity is correlated with low energies, where the channel and particle identifications become more difficult. This correlation between acollinearity and energy is shown

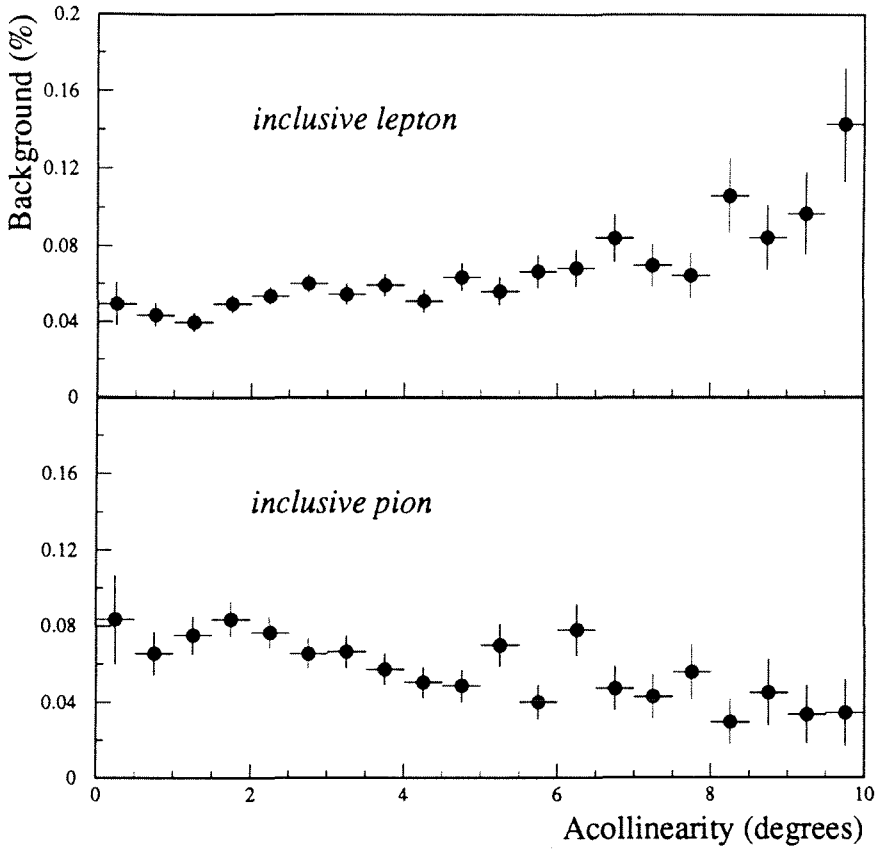

Figure 4.4: *Backgrounds as a function of the acollinearity angle for inclusive pions and leptons.*

in figure 4.5 for the lepton sample, being similar for the pion sample.

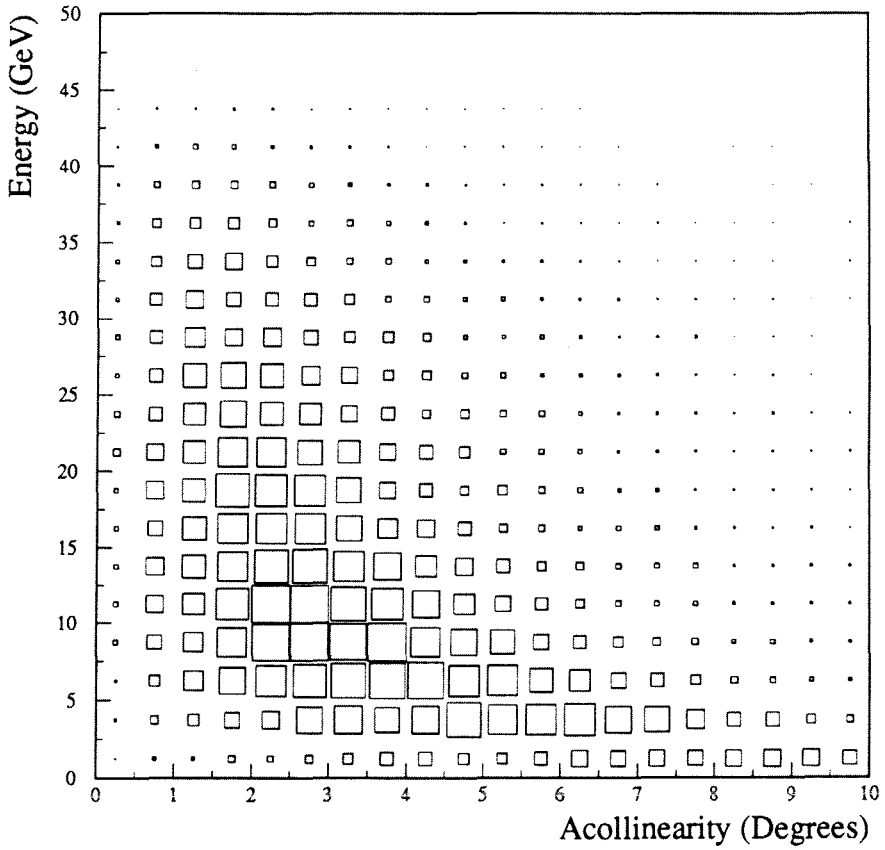

Figure 4.5: *Correlation between energy of a tau decay product and acollinearity for the lepton sample.*

Chapter 5

Measurement of the Electron and Tau Couplings

5.1 Observables Based on the Acollinearity

The two basic observables constructed from the acollinearity are the acollinearity distribution of the cross section

$$\frac{1}{\sigma}\frac{d\sigma}{d\varepsilon} = F(\varepsilon) - \mathcal{A}_\tau G(\varepsilon) \ , \tag{5.1}$$

and its forward backward asymmetry

$$A_{FB}(\varepsilon) = \frac{3}{4}\mathcal{A}_e \frac{F(\varepsilon)\mathcal{A}_\tau - G(\varepsilon)}{F(\varepsilon) - G(\varepsilon)\mathcal{A}_\tau} \ . \tag{5.2}$$

For reasons that will become more clear below, it is also useful to consider separately the acollinearity distribution of the cross section in the forward and in the backward hemispheres, $d\sigma^F/d\varepsilon$ and $d\sigma^B/d\varepsilon$, respectively. Since the acollinearity distribution at fixed θ is given by

$$\frac{1}{\sigma}\frac{d\sigma}{d\varepsilon} = F(\varepsilon) + P_\tau(\cos\theta)\ G(\varepsilon) \ , \tag{5.3}$$

one can obtain from them the values of P_τ in the forward and in the backward hemispheres.

Since $P_\tau(\cos\ \theta)$ is given by

$$P_\tau(\cos\theta) = -\frac{\mathcal{A}_\tau(1+\cos^2\theta) + \mathcal{A}_e(2\cos\theta)}{(1+\cos^2\theta) + \mathcal{A}_\tau\mathcal{A}_e(2\cos\theta)} \ , \tag{5.4}$$

the parameters $\mathcal{A}_\tau$, $\mathcal{A}_e$ and $\mathcal{A}_{e-\tau}$ can be derived from these forward and backward values of P_τ. This will be further explained in section 5.3.4.

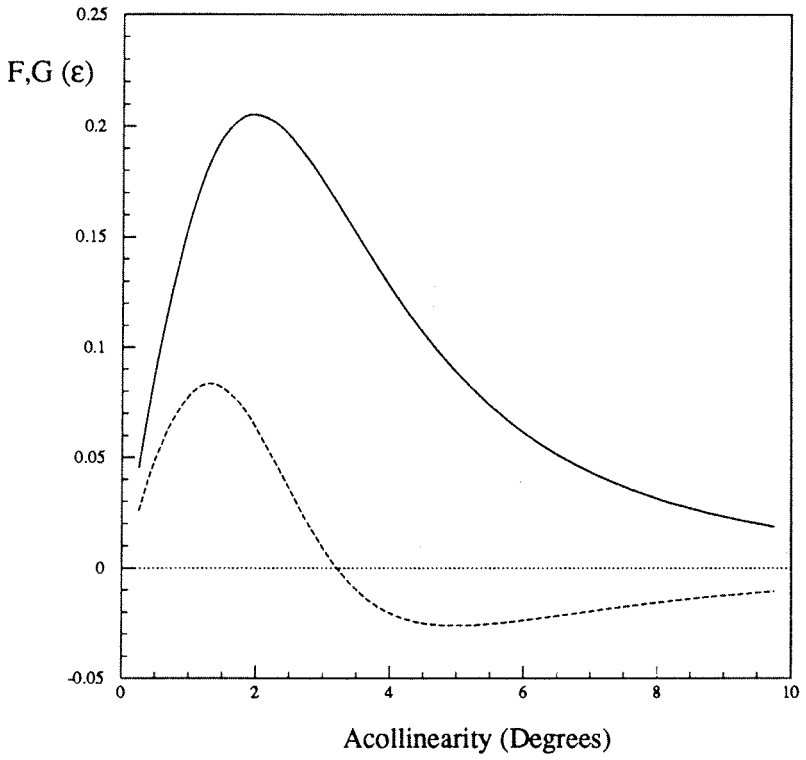

Figure 5.1: *F (continuous curve) and G (dashed curve) functions for inclusive pions.*

The inclusive samples selected for our measurements of the correlated distributions were described in chapter 4. The corresponding inclusive theoretical acollinearity distributions are defined by weighting with the appropriate branching ratios the exclusive theoretical distributions. Equation 5.5 illustrates one example, that of the inclusive pion,

$$\left.\frac{1}{\sigma}\frac{d\sigma}{d\varepsilon}\right|_{\pi-X} = \frac{Br(\tau \to e\nu_e\nu_\tau)\left.\frac{1}{\sigma}\frac{d\sigma}{d\varepsilon}\right|_{\pi-e} + Br(\tau \to \mu\nu_\mu\nu_\tau)\left.\frac{1}{\sigma}\frac{d\sigma}{d\varepsilon}\right|_{\pi-\mu} + \cdots}{Br(\tau \to e\nu_e\nu_\tau) + Br(\tau \to \mu\nu_\mu\nu_\tau) + \cdots}, \quad (5.5)$$

where the normalized cross sections in the numerator are given by equation 2.63 above, and $Br(\tau \to \nu x)$ is the branching ratio of tau decaying to the x one prong decay. In a similar way, the forward-backward asymmetry as a function of the

acollinearity for inclusive pions may be written as

$$A_{FB}(\varepsilon)|_{\pi-X} = \frac{Br(\tau \to e\nu_e\nu_\tau)\ A_{FB}(\varepsilon)|_{\pi-e} + Br(\tau \to \mu\nu_\mu\nu_\tau)\ A_{FB}(\varepsilon)|_{\pi-\mu} + \cdots}{Br(\tau \to e\nu_e\nu_\tau) + Br(\tau \to \mu\nu_\mu\nu_\tau) + \cdots}. \tag{5.6}$$

Analogous expressions can be written for the inclusive leptons with their corresponding branching ratios; and for the forward and backward acollinearity distributions for both inclusive samples. From now on, the effective observables analyzed are in terms of equations similar to 5.1 and 5.2 computed as in 5.5 and 5.6.

For these observables, their inclusive $F(\varepsilon)$ and $G(\varepsilon)$ functions for the two inclusive categories is plotted in order to illustrate the behaviour and sensitivity of the acollinearity distribution. Figure 5.1 and 5.2 show these functions for inclusive pions and leptons, respectively.

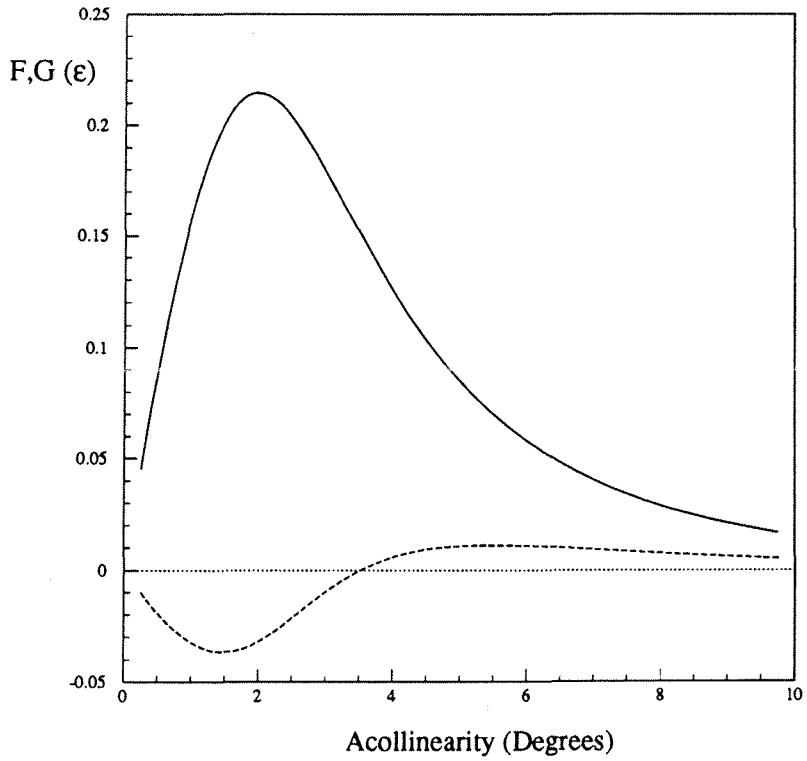

Figure 5.2: *F (continuous curve) and G (dashed curve) functions for inclusive leptons.*

From these basic observables several evaluations of the parameters $\mathcal{A}_\tau$, $\mathcal{A}_e$ and $\mathcal{A}_{e-\tau}$ are possible:

- $\mathcal{A}_\tau$ from $\frac{d\sigma}{d\varepsilon}$.

  $\mathcal{A}_\tau$ can be extracted in a straightforward way from a one parameter fit to equation 5.1.

- $\mathcal{A}_{e-\tau}$ from $A_{FB}(\varepsilon)$.

  $\mathcal{A}_{e-\tau}$ can also be extracted from a one parameter fit to equation 5.2. As explained below this value of $\mathcal{A}_{e-\tau}$ is correlated with the forward-backward charge asymmetry.

- $\mathcal{A}_\tau$, $\mathcal{A}_e$ and $\mathcal{A}_{e-\tau}$ from $\frac{d\sigma}{d\varepsilon}$ and $A_{FB}(\varepsilon)$ simultaneously.

  The parameters $\mathcal{A}_\tau$, $\mathcal{A}_e$ and $\mathcal{A}_{e-\tau}$ can be extracted in a simultaneous fit to equations 5.1 and 5.2. With this method maximal use is made of the information contained in the acollinearity observables. However, it should be pointed out that this method gives values correlated with those obtained from the forward-backward charge asymmetry. This can be seen by considering the integral over ε of $A_{FB}(\varepsilon)$, which is in fact the forward-backward charge asymmetry. Traditionally the forward-backward charge asymmetry is also used to determine $\mathcal{A}_e \cdot \mathcal{A}_\tau$ of the various leptons. Therefore, care should be taken when combining the values of these quantities obtained from the charge asymmetry and from $\frac{d\sigma}{d\varepsilon}$ and $A_{FB}(\varepsilon)$. However, the forward-backward asymmetry as a function of the acollinearity provides in addition further tests of the Standard Model as will be described in section 5.3.2 below.

- $\mathcal{A}_\tau$, $\mathcal{A}_e$ and $\mathcal{A}_{e-\tau}$ from $d\sigma^F/d\varepsilon$ and $d\sigma^B/d\varepsilon$.

  This method provides values of $\mathcal{A}_\tau$, $\mathcal{A}_e$ and $\mathcal{A}_{e-\tau}$ that are only weakly correlated with those obtained from the forward-backward charge asymmetry. For this reason, these are the values that will be combined with those obtained from the single tau method, as discussed in chapter 7.

The kinematics of the decay products of a single tau and the acollinearity of the two taus are correlated. When the decay products are more energetic the acollinearity has a tendency to be smaller, and vice versa. Therefore, the polarizations extracted from the acollinearity method and from the energy distributions are not completely independent. This correlation is smaller for larger numbers of particles in the final state of the tau decay. The systematic uncertainties in measuring angles are, however, largely independent of the systematics of the single-tau method described in chapter 7.

5.2 Corrections to the Data Samples

In the acollinearity method introduced above the Z^0 couplings are determined by fitting a tree-level theoretical prediction for the acollinearity distribution obtained as explained in the previous sections, with no initial- or final-state radiation, to the observed distribution in events where both taus decay to final states with a single charged track. This experimental distribution is first corrected for acceptance, background, experimental resolution and radiative effects. The acollinearity is defined using charged tracks only, as $\varepsilon = \pi - \theta_{12}$, where θ_{12} is the opening angle between the tracks given by

$$\cos\theta_{12} = \frac{\vec{p_1} \cdot \vec{p_2}}{|\vec{p_1}|\ |\vec{p_2}|}\ , \tag{5.7}$$

where $\vec{p_1}$ and $\vec{p_2}$ are the three components of the momenta, measured by the TPC and ITC, of the charged tracks in both hemispheres.

The corrected number of events in a given acollinearity bin i is given by

$$N_i^{cor} = C_i^{rad} \frac{1}{\eta_i} \sum_j A_{ij} N_j^{obs} (1 - B_j)\ , \tag{5.8}$$

where N_j^{obs} is the number of events in bin j of acollinearity, η_i and B_j are the efficiency and background fraction for bin i and j respectively, and C_i^{rad} is a correction factor accounting for radiative effects and the effect of accompanying neutral particles. No attempt is made to reconstruct these neutrals in order to keep the acollinearity measurement as independent as possible from the energy measurement. In this way the systematic uncertainties are expected to be largely independent. The

efficiencies and different backgrounds are shown previously in chapter 4, in figures 4.3 and 4.4.

The angular resolution unfolding matrix A_{ij} has been calculated from the bin to bin migrations observed in Monte Carlo events with full detector simulation by solving the equation

$$O_i = \sum_j G_{ij} \cdot T_j \ , \tag{5.9}$$

where O_i is the number of events in acollinearity bin i, T_j is the number of events in bin j of the true acollinearity, and G_{ij} is the probability that an event with true acollinearity in bin j will be reconstructed with observed acollinearity in bin i. The solution is given by $A_{ij} = (G^{-1})_{ij}$.

This procedure involves the inverse of the matrix G_{ij}, which can in principle lead to unstable results. A widely used alternative to bypass the problems connected with the inversion of equation 5.9 is to estimate directly from the Monte Carlo simulation a probability matrix p_{ij}, which is defined by

$$p_{ij} = \frac{G_{ij}}{\sum_j G_{ij}} \ . \tag{5.10}$$

However, since these probabilities depend on the acollinearity distribution put into the simulation, the unfolding result can be biased towards the Monte Carlo input, which is not the case with the inversion method. In this particular analysis the matrix G_{ij} is nearly diagonal resulting in a stable correction matrix A_{ij}. The matrix G_{ij} for inclusive leptons is shown in figure 5.3.

The coefficients C_i^{rad} have been derived from two high-statistics Monte Carlo samples of tau pair events generated without detector simulation[3] [72]. One sample was generated with all radiative effects disabled, and the acollinearity was defined using the parent hadron h for $\tau \to \nu_\tau h$. The other sample included all radiative effects, and the acollinearity was defined using the charged pion for $\tau \to \nu_\tau h$, $h \to \pi x$ decays with x being any number of π^0. The corrections are the bin by bin ratio between the differential acollinearity distributions of the two samples. Figure 5.4 shows these coefficients C_i^{rad} for both samples, inclusive pion and inclusive

[3]The version of KORALZ used for the generation of the tau pair events in this analysis does not included the transverse spin correlations, which are not relevant for the acollinearity distribution since they are integrated out.

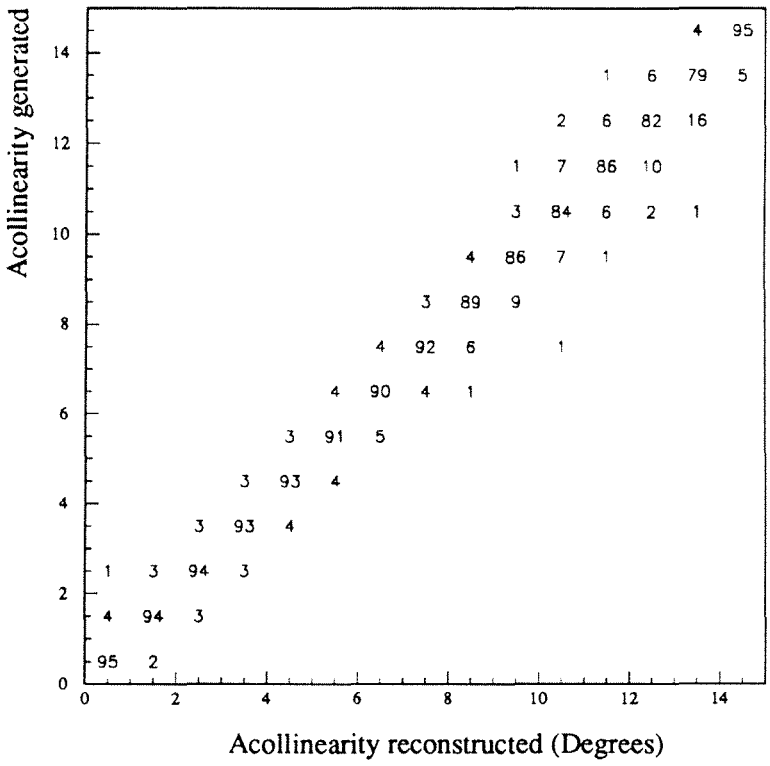

Figure 5.3: *Resolution matrix G_{ij} applied for inclusive lepton sample. The numbers in each column represents the percentage of acollinearity generated lying in a bin of acollinearity reconstructed.*

lepton, integrated over the whole $\cos\theta$ range. Analogous corrections have been computed for the forward and backward hemispheres. Their shape is similar to those plotted in figure 5.4.

5.3 The Acollinearity Distribution and its Forward-Backward Asymmetry

The corrected (using expression 5.8) and uncorrected acollinearity distributions, for the inclusive pion and lepton samples, are shown in figure 5.5.

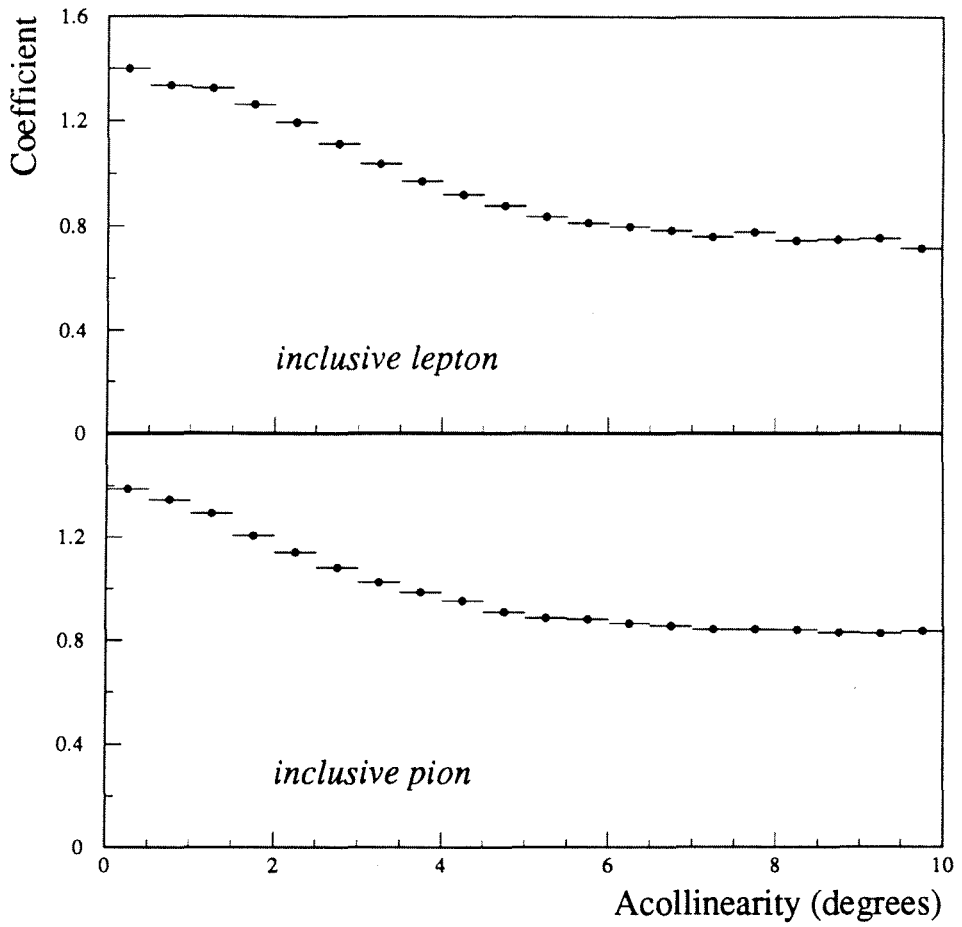

Figure 5.4: *Correction coefficients for inclusive pions and leptons as a function of the acollinearity.*

5.3.1 Extracting $\mathcal{A}_\tau$ from $\frac{d\sigma}{d\varepsilon}$

The average tau polarization, equivalent to $\mathcal{A}_\tau$, is extracted from each of the corrected distributions by a χ^2 fit to the theoretical acollinearity distributions where correlations between bins due to the unfolding procedure are taken into account. The χ^2 is defined as:

$$\chi^2 = \sum_{ij} (N^{th} - N^{cor})_i \; V_{ij}^{-1} \; (N^{th} - N^{cor})_j \; , \tag{5.11}$$

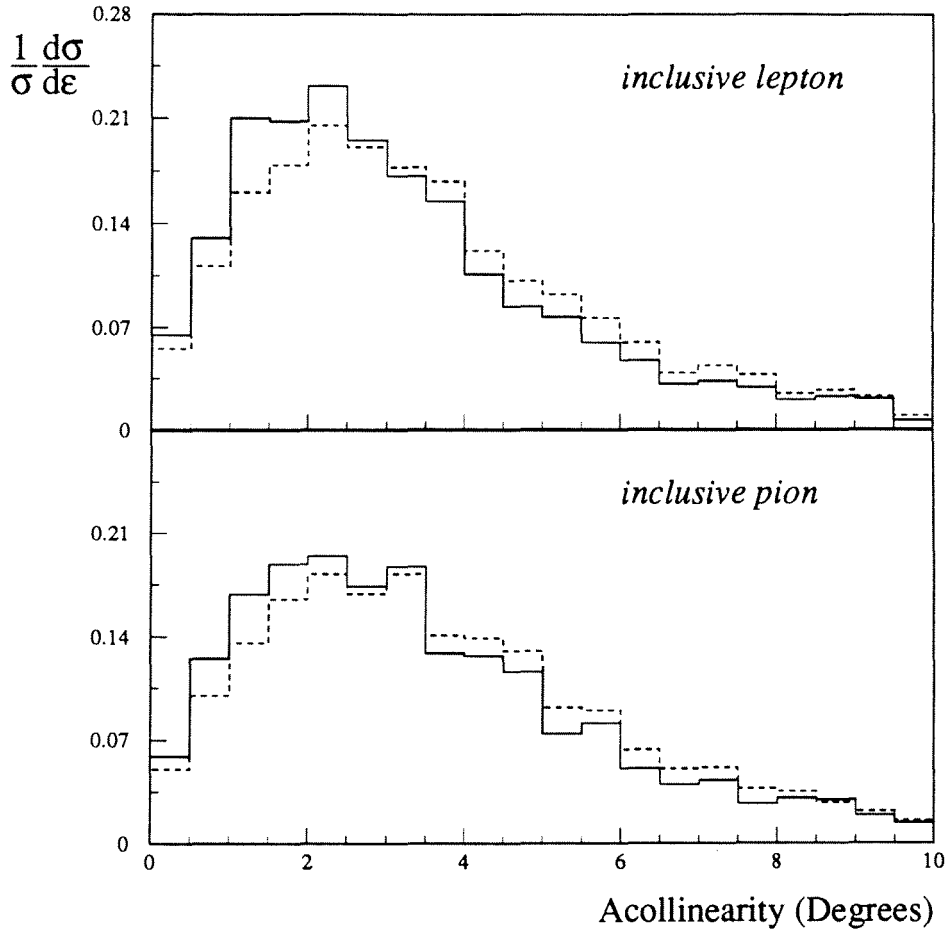

Figure 5.5: *Observed distributions integrated over the whole acceptance range (solid line) and corrected distributions (dashed line) for pions and leptons.*

where N^{th} is the predicted number of events and N^{cor} is the corrected number of events in bin i of acollinearity. The covariance matrix V_{ij} is given by

$$V_{ij} = \sum_k A_{ik} E_k A_{kj}^T , \tag{5.12}$$

where A_{ij} is the angular resolution matrix (see equation 5.8) and E_k is the error array which is given by

$$E_k = \left(\frac{C_k^{rad}}{\eta_k} (1 - B_k) \sigma_k \right)^2 , \tag{5.13}$$

where σ_k accounts for the statistical error of the data and the Monte Carlo. A range of 10 degrees in the acollinearity angle has been chosen to perform the least

squares fit for both inclusive samples. A wider range would increase the systematic uncertainties in the unfolding procedure due to the statistical fluctuations on the tails of the distributions, where the cross section is very small.

The values obtained on $\mathcal{A}_\tau$ from the inclusive pion and leptons are shown in table 5.1. The fitted curves for both samples are plotted in figure 5.6, where the contributions from right- and left-handed taus are also shown.

event type	$\mathcal{A}_\tau$ from $d\sigma/d\varepsilon$	χ^2/ndf
$\pi - X$	0.059 ± 0.065	18/19
$l - X$	0.302 ± 0.099	20/19

Table 5.1: *Polarization parameters extracted from the acollinearity distribution of the cross section. The error is statistical.*

5.3.2 Extracting $\mathcal{A}_{e-\tau}$ from $A_{FB}(\varepsilon)$

A fit to the forward-backward asymmetry as a function of the acollinearity $A_{FB}(\varepsilon)$ (equation 5.2) is performed to extract $\mathcal{A}_{e-\tau}$ assuming universality, $\mathcal{A}_e = \mathcal{A}_\tau$. In this case, a one parameter fit has been chosen because the statistics do not allow a meaningful two-parameter fit to $\mathcal{A}_e$ and $\mathcal{A}_\tau$. A similar χ^2 is minimized, where correlations between bins due to the unfolding procedure in the forward and backward hemispheres are taken into account. It has been assumed that there were not correlations between the forward and backward hemispheres. A more detailed description of the constructed covariance matrix can be found in appendix B.

event type	$\mathcal{A}_{e-\tau}$ from $A_{FB}(\varepsilon)$	χ^2/ndf
$\pi - X$	0.118 ± 0.075	19/19
$l - X$	0.158 ± 0.058	11/19

Table 5.2: *Polarization parameters extracted from the forward-backward asymmetry as a function of the acollinearity. The error is statistical.*

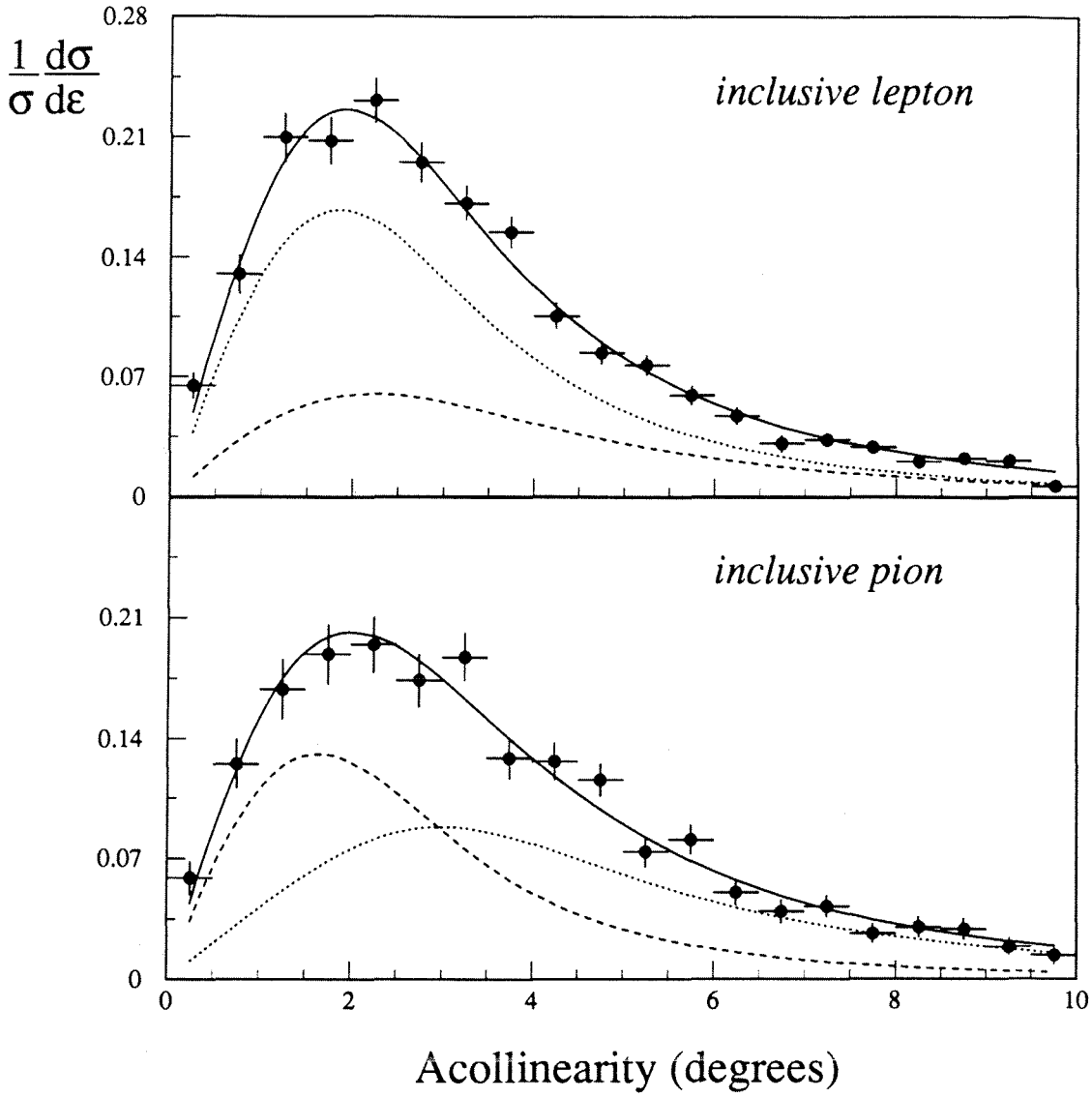

Figure 5.6: *Result of the fit to the acollinearity distribution of the cross section. The points with error bars are the corrected data. Solid curves are the result of the fits. Dashed (dotted) curves are the contributions from right- (left-) handed taus.*

The values obtained from these fits are shown in table 5.2. Figure 5.7 shows the measured asymmetries with the fitted curves. In order to illustrate the sensitivity of these asymmetries, the predicted forward-backward asymmetries for $\mathcal{A}_e = \mathcal{A}_\tau = \pm\ 0.5$ for pion and lepton samples, are drawn in figure 5.8. As mentioned in section 5.1 these values are correlated to those obtained from the forward-backward charge

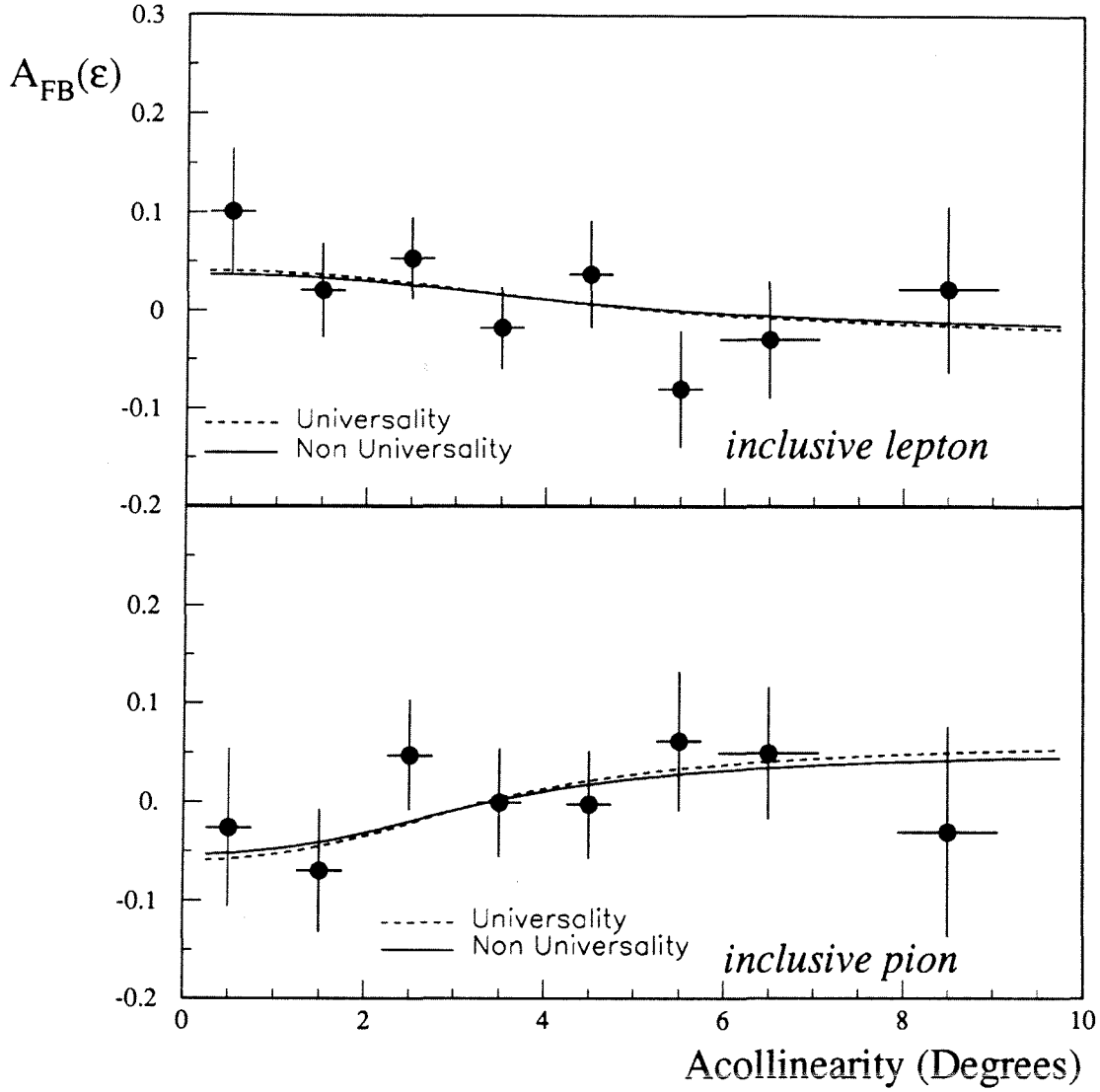

Figure 5.7: *Result of the fit to the forward-backward asymmetry as a function of the acollinearity. The points with error bars are the corrected data. Solid and dashed curves are the results of the fits.*

asymmetry [73], a quantity also used to determine the Z^0 couplings.

It is interesting to mention that the forward-backward charge asymmetry in tau pairs has been analyzed traditionally integrating over the energies and the acollinearity. Any possible contribution in the cross section proportional to $\mathcal{A}_e\mathcal{A}_\tau \cos\theta$

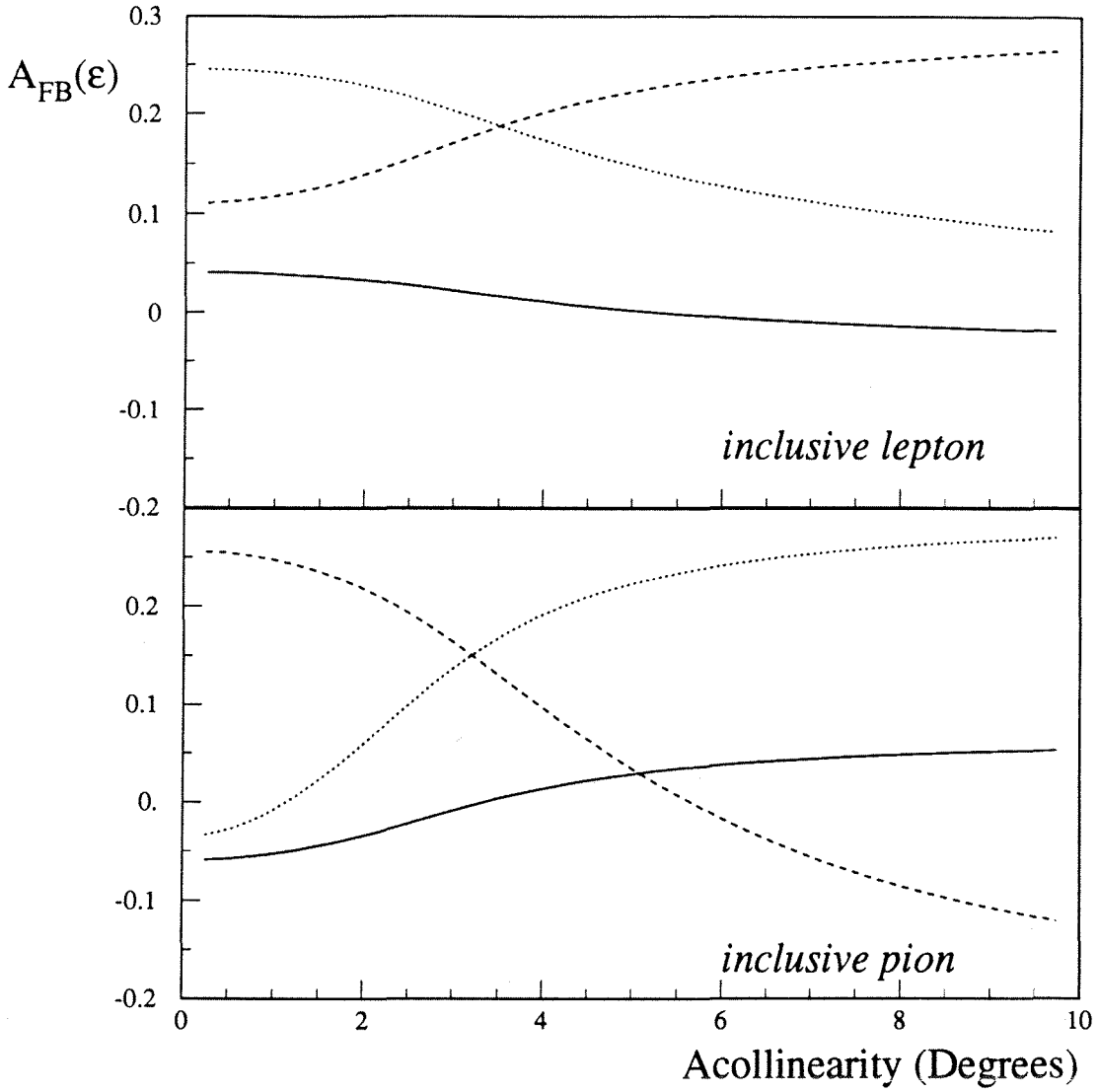

Figure 5.8: *Predicted forward-backward asymmetry as a function of the acollinearity for* $\mathcal{A}_{e-\tau} = \pm\ 0.5$, *dotted and dashed lines respectively, for inclusive pions and leptons. The solid curves are the results of the fit.*

times a function $h'(\varepsilon)$ such that

$$\int h'(\varepsilon)\ d\varepsilon = 0 \tag{5.14}$$

will not affect the forward-backward charge asymmetry but it will be manifested very clearly in figure 5.7. The χ^2 of the fit, given in table 5.2, provides a quantitative

test of the agreement of the data with the form predicted by the Standard Model, and can be taken as a test of this model.

Futhermore, if the forward-backward asymmetry of the acollinearity distribution, given by equation 5.2, is rewritten as

$$A_{FB}(\varepsilon) = \frac{A^c_{FB}\ F(\varepsilon) - \frac{3}{4}\ \mathcal{A}_{e-\tau}\ G(\varepsilon)}{F(\varepsilon) - \mathcal{A}_{e-\tau}\ G(\varepsilon)}\ , \tag{5.15}$$

where A^c_{FB} is the forward-backward charge asymmetry, a simple fit to the two parameters A^c_{FB} and $\mathcal{A}_{e-\tau}$ yields

$$A^c_{FB} = 0.013 \pm 0.013\ , \tag{5.16}$$

$$\mathcal{A}_{e-\tau} = 0.146 \pm 0.075\ . \tag{5.17}$$

The value obtained of $\mathcal{A}_{e-\tau}$ from this fit is essentially independent of the information of the forward-backward charge asymmetry. This may be compared to [73] from where is taken the value of the forward-backward charge asymmetry at the peak, that is measured through its $\cos\theta$ dependence, that gives

$$A^c_{FB} = 0.009 \pm 0.009\ .$$

Taking into account that roughly only 50% of the events are common in both samples, mainly because the acollinearity analysis is from one-prong events, the difference between both measurements of A^c_{FB} is 0.004 ± 0.012, where this error is from the statistical fluctuation of the non-common events.

Finally, equation 5.2 suggests a different procedure to extract the tau and electron couplings to the Z^0, by a simultaneous fit to the forward-backward charge asymmetry and to the forward-backward polarization asymmetry, taking into account the correlation between them. This maximizes the information that can be obtained from the acollinearity angle.

5.3.3 Extracting $\mathcal{A}_\tau, \mathcal{A}_e$ and $\mathcal{A}_{e-\tau}$ simultaneously from $\frac{d\sigma}{d\varepsilon}$ and $A_{FB}(\varepsilon)$

The values of $\mathcal{A}_e$, $\mathcal{A}_\tau$ and $\mathcal{A}_{e-\tau}$ can alternatively be obtained from a simultaneous χ^2 fit of the acollinearity distributions and of the forward-backward asymmetry

as a function of the acollinearity using expressions 5.1 and 5.2. The advantage of this simultaneous fit is that the forward-backward asymmetry has a quadratic dependence on the fitted Z^0 couplings giving non-symmetric errors, and thus making it difficult to average these results. This problem is solved when all the information is fitted together. The same fit, with the constraint $\mathcal{A}_e = \mathcal{A}_\tau$ gives $\mathcal{A}_{e-\tau}$, which are shown in table 5.3. These values of $\mathcal{A}_e$ and $\mathcal{A}_\tau$ have a correlation coefficient of -0.22.

parameter	$d\sigma/d\varepsilon$ and $A_{FB}(\varepsilon)$	χ^2/ndf
$\mathcal{A}_e$	0.130 ± 0.063	86/78
$\mathcal{A}_\tau$	0.162 ± 0.052	
$\mathcal{A}_{e-\tau}$	0.148 ± 0.035	87/79

Table 5.3: *Polarization parameters extracted from the acollinearity distribution of the cross section and its forward backward asymmetry. The error is statistical only.*

These measurements have to be corrected in principle for the effect of the radiative corrections. The radiative corrections that enters in those measurements are mainly the initial- and final-state radiation, subtraction of the photon exchange and its interference with the Z^0 exchange. The initial- and final-state radiative corrections have been taken into account by means of the deconvolution coefficients as explained in equation 5.8. The subtraction of the photon exchange and the interference effect amounts to -0.0005 for the parameters $\mathcal{A}_e$, $\mathcal{A}_\tau$ and $\mathcal{A}_{e-\tau}$. Finally, these measurements are performed at a certain average value of the center of mass energy that does not correspond to M_Z. The integrated luminosities, that enters in the analysis per year and the average energies are shown in table 4.3. The effective center of mass energy turns out to be 91.220 GeV. Running the measurement up to the center of mass energy equal to M_Z one gets by means of the program ASYM [74] a correction of +0.0003. This correction is at the same level for $\mathcal{A}_e$ and $\mathcal{A}_\tau$. In summary, going from the measured parameters $\mathcal{A}_e$, $\mathcal{A}_\tau$ and $\mathcal{A}_{e-\tau}$ to the bare parameters $\mathcal{A}_e^o(M_Z)$, $\mathcal{A}_\tau^o(M_Z)$ and $\mathcal{A}_{e-\tau}^o(M_Z)$ the theoretical corrections are negligible.

5.3.4 The Forward and Backward Acollinearity Distributions

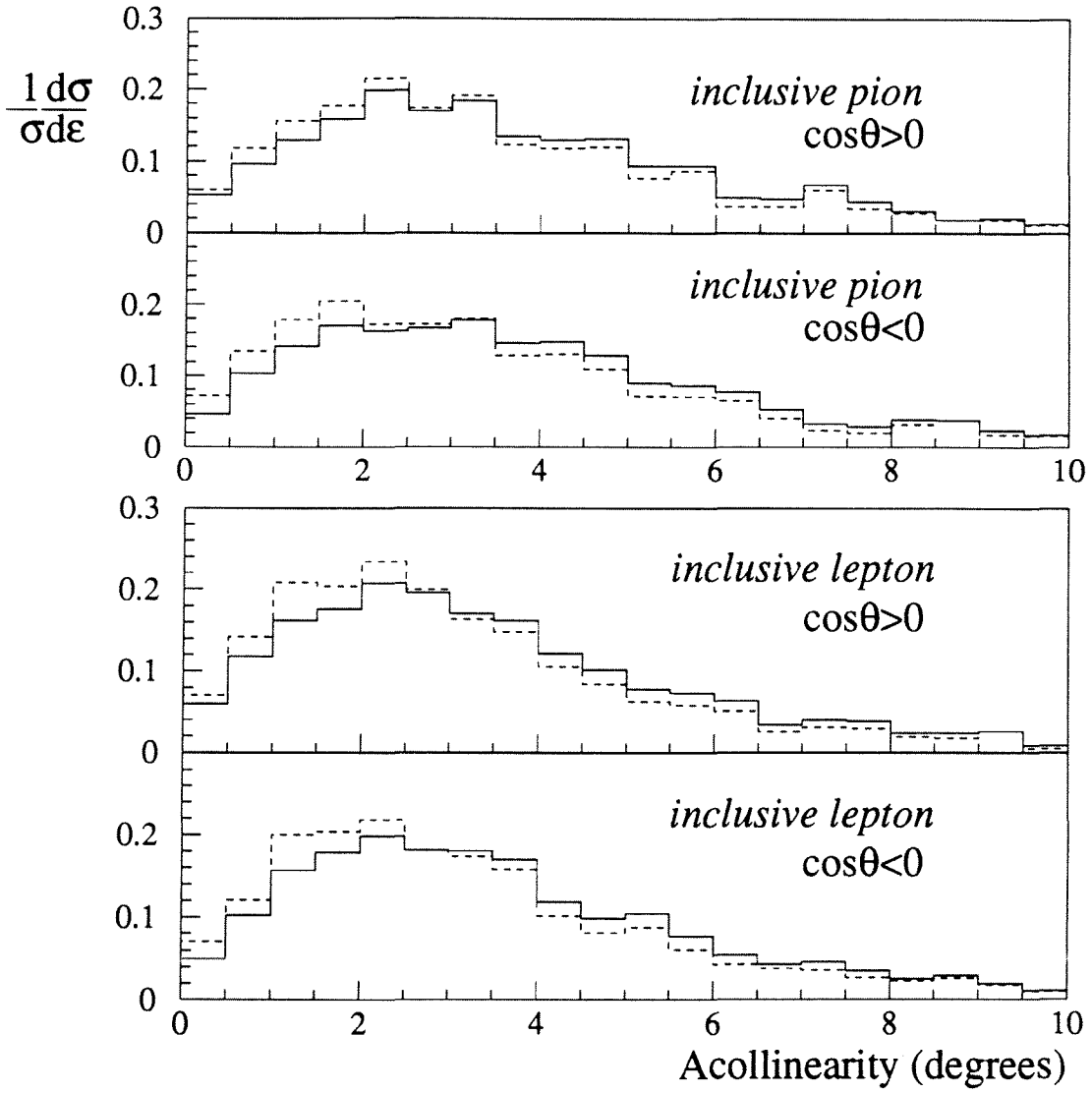

Figure 5.9: *Observed distributions integrated over the forward and backward hemispheres (solid line) and corrected distributions (dashed line) for pions and leptons.*

This method offers perhaps the greatest advantages. In addition to measuring $\mathcal{A}_e$ and $\mathcal{A}_\tau$ separately (hence testing universality) and to improving the statistical power of the fit by exploiting the $\cos\theta$ dependence (in two bins), without a need for an absolute normalization, the method greatly reduces the correlation between the

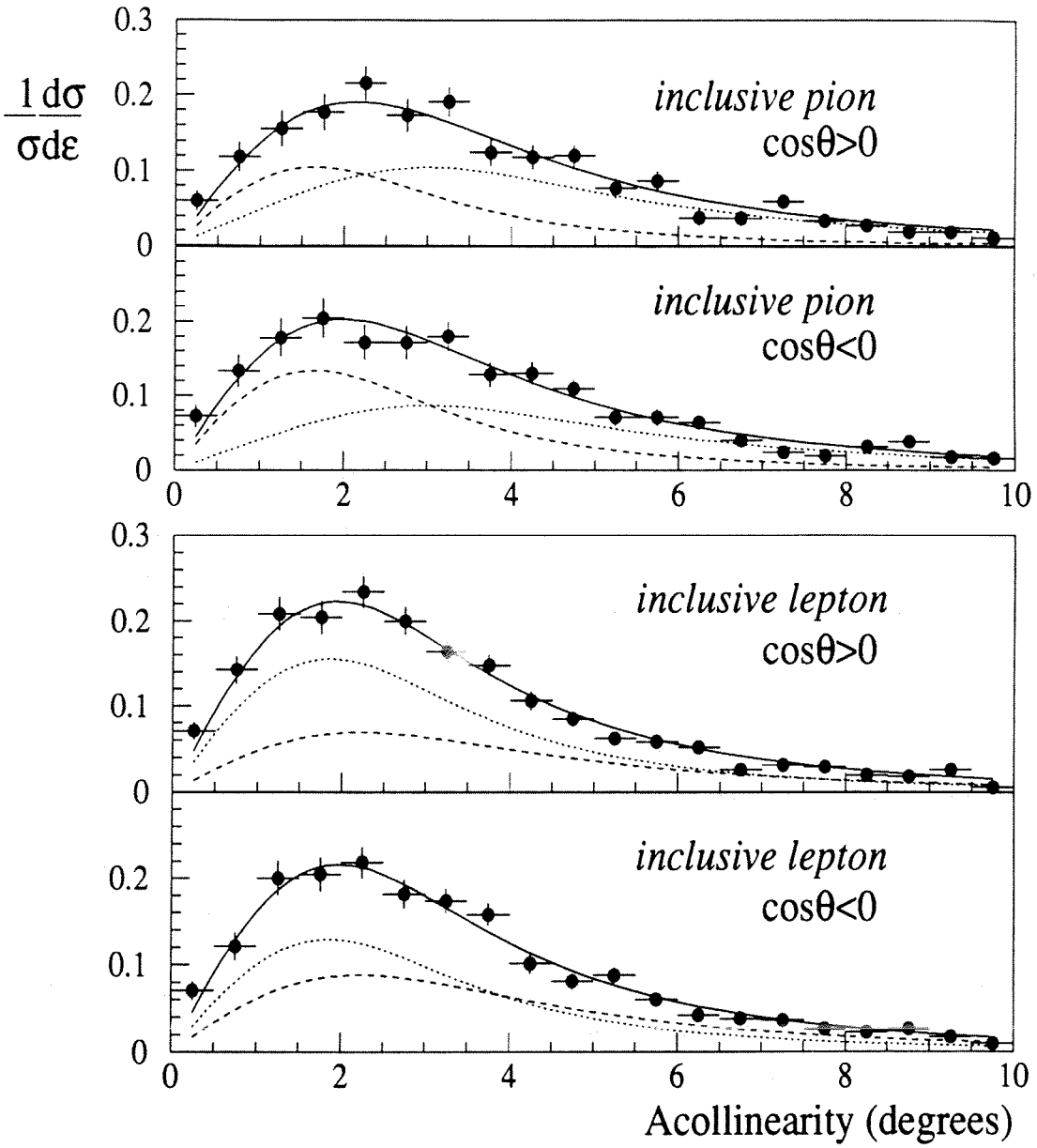

Figure 5.10: *Result of the fit to the normalized forward and backward acollinearity distributions. The points with error bars are the corrected data. Solid curves are the results of the fits. Dashed (dotted) curves are the contributions from right- (left-) handed taus.*

result and that obtained from the forward-backward charge asymmetry. The latter

$\cos\theta$ range	$P_\tau(\cos\theta)$	χ^2/ndf
$[-0.9, 0.]$	-0.038 ± 0.078	47/39
$[0., +0.9]$	-0.254 ± 0.078	41/39

Table 5.4: *Measured polarization as a function of polar angle, for the acollinearity method. The error is statistical only.*

is traditionally used in in global electroweak fits, and therefore the results obtained here can be easily incorporated in this type of analysis.

However, it is interesting to point out that the results still have a small correlation with the forward-backward charge asymmetry. This is also true for the measurements of the τ polarization and the $\cos\theta$ dependence of the polarization based on energy measurements. In fact, it is very difficult to decouple the information from the forward-backward charge asymmetry and from the forward-backward asymmetry of the polarization because both have a $\cos\theta$ dependence. This can be seen for instance in equation 5.4.

The observed and corrected distributions, for pions and leptons, integrated over the forward and backward hemispheres are plotted in figure 5.9. The values of the average tau polarization in the forward and backward hemispheres, $P_\tau(\cos\theta)$, are extracted from the corrected acollinearity distributions of the inclusive pion and inclusive lepton samples, shown in figure 5.10. The fit is performed with the same assumptions used in the previous section, to the inclusive pions and leptons simultaneously.

Table 5.4 shows the values of $P_\tau(\cos\theta)$ obtained in the forward and backward hemispheres. The solid curves in figure 5.10 show the acollinearity distributions corresponding to these fitted values.

Table 5.5 shows the corresponding values of $\mathcal{A}_e$ and $\mathcal{A}_\tau$, or, assuming universality, $\mathcal{A}_{e-\tau}$, extracted using equation 5.4. The reported values of $\mathcal{A}_e$ and $\mathcal{A}_\tau$ in table 5.5 have a correlation coefficient of 0.06. These results are combined in chapter 7 with the corresponding values obtained from the single-tau method.

The values in table 5.5 are quite consistent with those of table 5.3. The errors are somewhat larger in table 5.5, because the fit does not exploit the information

parameter	$d\sigma^F/d\varepsilon$ and $d\sigma^B/d\varepsilon$
$\mathcal{A}_e$	0.154 ± 0.079
$\mathcal{A}_\tau$	0.147 ± 0.056
$\mathcal{A}_{e-\tau}$	0.149 ± 0.047

Table 5.5: *Polarization parameters extracted from polar angle dependence of the acollinearity distribution. The first error is statistical and the second is systematic.*

in the forward-backward charge asymmetry. It is only the error on $\mathcal{A}_{e-\tau}$, where an induced anticorrelation coefficient appears due to the $\mathcal{A}_e \cdot \mathcal{A}_\tau$ term, that changes significantly. Figure 5.11 compares these mean values from tables 5.5 and 5.3 with their statistical errors, and also shows the effective value and error on $\mathcal{A}_e$, $\mathcal{A}_\tau$ and $\mathcal{A}_{e-\tau}$ from the forward-backward charge asymmetry. The latter are calculated by estimating the values that the parameters would have to have such that combined as independent (neglecting correlations) with those of table 5.5, reproduce the values of table 5.3.

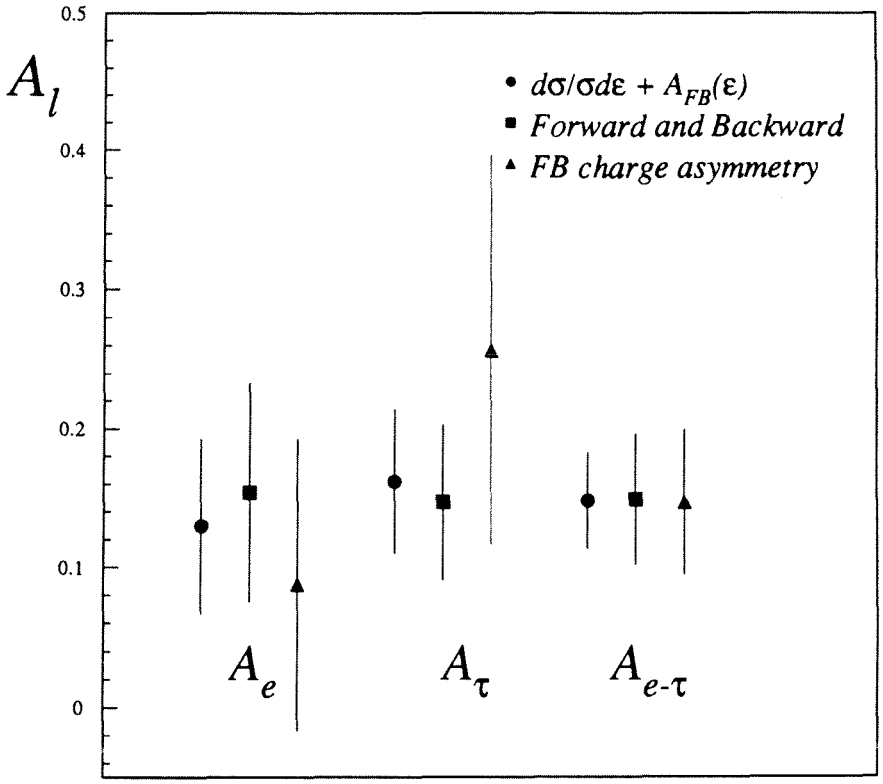

Figure 5.11: *Comparison of the fitted values with two different set of observables. The error bars included only statistical errors.*

Chapter 6

Systematic Errors

The measurements of $\mathcal{A}_e$, $\mathcal{A}_\tau$ and $\mathcal{A}_{e-\tau}$ rely on the understanding of the physics and the detector response. Any discrepancy between these simulations and the experiment can lead in principle to systematic uncertainties.

In fact it is known that several discrepancies exist between data and Monte Carlo. For instance, the charge-dependent shift on the measured momentum of particles in either the very forward or backward regions; variation of dE/dx as a function of $\cos\theta$; inefficiencies of HCAL tubes for muons; slight discrepancy in the rate of pions having muon chamber hits; poor modeling of HARBOR variables as described in reference [64].

However, not all these discrepancies, and others that will be described later in this chapter, have the same effect in obtaining the parameters that have been considered. Equation 5.4 expanded only to first order in terms of the fitted parameters can be written as

$$P_\tau(\cos\theta) \approx \mathcal{A}_\tau + \mathcal{A}_e \frac{2\cos\theta}{1+\cos^2\theta} + \mathcal{O}\left(\mathcal{A}_e^2\mathcal{A}_\tau, \mathcal{A}_e\mathcal{A}_\tau^2\right) , \tag{6.1}$$

which shows that $\mathcal{A}_\tau$ can be extracted from the average value of the polarization, while $\mathcal{A}_e$ is sensitive to the difference between the forward and backward values. The systematic uncertainties in these two parameters thus come from very different sources. Namely, any systematic effect leading to a forward-backward symmetric shift in the polarization affects only $\mathcal{A}_\tau$, while systematic effects which depend on $\cos\theta$ can affect either $\mathcal{A}_\tau$ or $\mathcal{A}_e$. A discrepancy having the same effect on the polarization of positive and negative tau decays will not affect $\mathcal{A}_e$, since it cancels out in the forward and backward difference. Even if a discrepancy with a $\cos\theta$

dependence affecting positive and negative tau decays differently, but with no effect on the polarization difference between the forward and backward hemispheres, will not affect $\mathcal{A}_e$. From now on, all the tables quoting systematic errors will refer to $\mathcal{A}_\tau$, unless otherwise specified.

The different sources of systematic errors are grouped according to expression 5.8, used to correct the observed acollinearity distributions

$$N_i^{cor} = C_i^{rad} \frac{1}{\eta_i} \sum_j A_{ij} N_j^{obs} (1 - B_j) \ . \tag{6.2}$$

Therefore, the systematic errors will be classified as coming from:

- selection and acceptance, which refers to η_i,
- backgrounds involved in the determination of B_j,
- tracking uncertainties affecting the measurement of the acollinearity angle, which enters in the matrix A_{ij},
- branching ratios and theoretical uncertainties, which appear in the calculation of the coefficients C_i^{rad} and in the computation of the theoretical formulae.

6.1 Selection and Acceptance

As described in chapter 4, our classification relies first on the track identification in one hemisphere and secondly in the decay channel identification.

Any imperfect modelling of the acollinearity dependence of the efficiency for identifying charged particles, photons and π^0s can influence the measured polarization by distorting the shape of the observed distributions. The ideal way to determine the level of this systematic uncertainty is to have a sample of particles in the detector, whose identity is known independently of the identification procedure used in the analysis. The comparison of the efficiency for this sample with that in the simulation leads in a straightforward way to a calculation of the apparent effect on the polarization.

To obtain such a sample of charged particles; electrons, muons and pions from the data are identified in ALEPH without using any of the information used in the

neural net particle identification. This is possible mainly for physics channels which can be selected on a kinematical basis such as:

- $e^{\pm}$ from $Z^0 \to e^+e^-(\gamma)$,
- $e^{\pm}$ from $\gamma\gamma \to e^+e^-$,
- $e^{\pm}$ from $\gamma \to e^+e^-$,
- $\mu^{\pm}$ from $Z^0 \to \mu^+\mu^-(\gamma)$,
- $\mu^{\pm}$ from $\gamma\gamma \to \mu^+\mu^-$,
- $\pi^{\pm}$ from $\tau \to \pi^{\pm}\pi^0[\pi^0...]\nu$ (tagged by presence of a resolved π^0), and
- $\pi^{\pm}$ from $\tau \to \pi^{\pm}\pi^{\pm}\pi^{\mp}(\pi^0...)\nu$.

As explicitly written below in equation 6.3, one can infer the error induced in the polarization from the acollinearity dependence of the ratio of the measured efficiency of the particle identification in the real data to that of the simulation. This procedure has some advantages over using data from a test beam, because it uses events distributed in the overall $\cos\theta$ range and takes into account the effect of cracks in the detector. The disadvantages are the control of the background in this kinematical identification and the lack of statistics in certain ranges of acollinearity.

For our purpose the kinematically identified electrons are taken from Bhabha events at low acollinearity and from two-photon events for the higher acollinearity range. The requirements for an electron from Bhabha events are mainly to have 2 good tracks with no photons inside the acceptance. The electron candidate must have a momentum larger than 38 GeV and the other track must be identified as an electron. In the case of electrons from two-photon events the requirements are similar; with the difference that the electron candidates should have momenta smaller than 20 GeV and small angles with respect to the beam axis. For muons from Z^0 decays and from the two-photon process the same procedure that is described for Bhabha events and for electrons from two-photons is applied respectively, but requiring an identified muon instead of a identified electron. For the kinematically identified pions, one good track and two photons with the invariant mass of the π^0 (as defined in chapter 4), such that the combined mass is within one sigma of the ρ

mass resolution, is required. With these criteria the samples obtained have a purity larger than 99% [67].

In order to measure the systematic error in $\mathcal{A}_\tau$ coming from the Neural Net particle identification, a fit is performed which minimizes

$$\chi^2 = \sum \frac{\left(\frac{\eta^{DATA}(\varepsilon)}{\eta^{MC}(\varepsilon)} - \frac{\frac{d\sigma}{d\varepsilon}(\varepsilon, P_\tau + \Delta P_\tau)}{\frac{d\sigma}{d\varepsilon}(\varepsilon, P_\tau)} \right)^2}{\left(\Delta\eta(\varepsilon) \right)^2}, \tag{6.3}$$

where $\eta^{DATA}(\varepsilon)$ and $\eta^{MC}(\varepsilon)$ are the efficiencies for kinematically-selected data and equivalent for Monte Carlo as a function of the acollinearity angle respectively; $d\sigma/d\varepsilon$ are the theoretical cross sections for the samples under study (as given in chapter 2); $\Delta\eta(\varepsilon)$ is the statistical error of the ratio of those efficiencies; and P_τ is the value for the average polarization in the Standard Model and ΔP_τ is the shift value considered as the single free parameter in the fit.

The efficiency $\eta^{MC}(\varepsilon)$ is computed as the ratio between the kinematically identified Monte Carlo generated events and the identified events by the Neural Net algorithm. In a similar way the efficiency $\eta^{DATA}(\varepsilon)$ has been computed.

Table 6.1 shows the fit results for the parameter ΔP_τ and their associated statistical errors for both the 1990 and 1991 data samples. From this table one can infer that all the values are compatible with zero; thus the statistical errors have been considered as the associated systematic errors. The ratio of those efficiencies and the fit results for the 1991 data sample are plotted in figure 6.1.

With a similar procedure the systematic errors coming from the particle identification for $A_{FB}(\varepsilon)$ can be inferred by minimizing

$$\chi^2 = \sum \frac{\left(\frac{\eta^{DATA}(\varepsilon)}{\eta^{MC}(\varepsilon)} - \frac{A_{FB}(\varepsilon, P_\tau + \Delta P_\tau)}{A_{FB}(\varepsilon, P_\tau)} \right)^2}{\left(\Delta\eta(\varepsilon) \right)^2}, \tag{6.4}$$

where $\eta^{DATA}(\varepsilon)$ and $\eta^{MC}(\varepsilon)$ are the efficiencies described previously; $A_{FB}(\varepsilon)$ is the forward-backward asymmetry of the acollinearity distribution and $\Delta\eta(\varepsilon)$ is the statistical error of the ratio of the efficiencies.

ΔP_τ from $d\sigma/d\varepsilon$		
particle	1990	1991
e	-0.015 ± 0.013	0.014 ± 0.009
μ	-0.006 ± 0.008	-0.001 ± 0.004
π	-0.010 ± 0.013	0.012 ± 0.011

Table 6.1: *Systematic errors on the polarization coming from the effect, in $d\sigma/d\varepsilon$, of the lack of perfect modeling of the particle identification.*

The fit results for the parameter ΔP_τ and its associated statistical error for both 1990 and 1991 data samples for the forward-backward asymmetry are shown in table 6.2. Again no significant discrepancy is found within the statistical precision.

ΔP_τ from $A_{FB}(\varepsilon)$		
particle	1990	1991
e	-0.14 ± 0.08	-0.10 ± 0.14
μ	-0.25 ± 0.12	0.03 ± 0.09
π	0.56 ± 0.65	-0.48 ± 0.41

Table 6.2: *Systematic errors on the polarization coming from the effect, in $A_{FB}(\varepsilon)$, of the lack of perfect modeling of the particle identification. All those numbers must be multiplied by* 10^{-3}.

Due to the nature of the analysis done it is important to check for any possible deviation in the efficiencies as a function of the acollinearity, but it is crucial as well to perform the same kind of test of these efficiencies as a function of $\cos\theta$. Figure 6.2 shows the ratio of the Monte Carlo and data efficiencies for kinematically-selected events in bins of $\cos\theta$ for pions, Bhabha electrons and muon pairs. No significant discrepancy is observed.

For the $\tau \to e\nu_e\nu_\tau$, $\tau \to \mu\nu_\mu\nu_\tau$ and $\tau \to \pi\nu_\tau$ channel classification, the simulation of photons is crucial. In particular for the $\tau \to \pi\nu_\tau$ channel, the simulation of the fake photons accompanying hadronic showers in the electromagnetic calorimeter

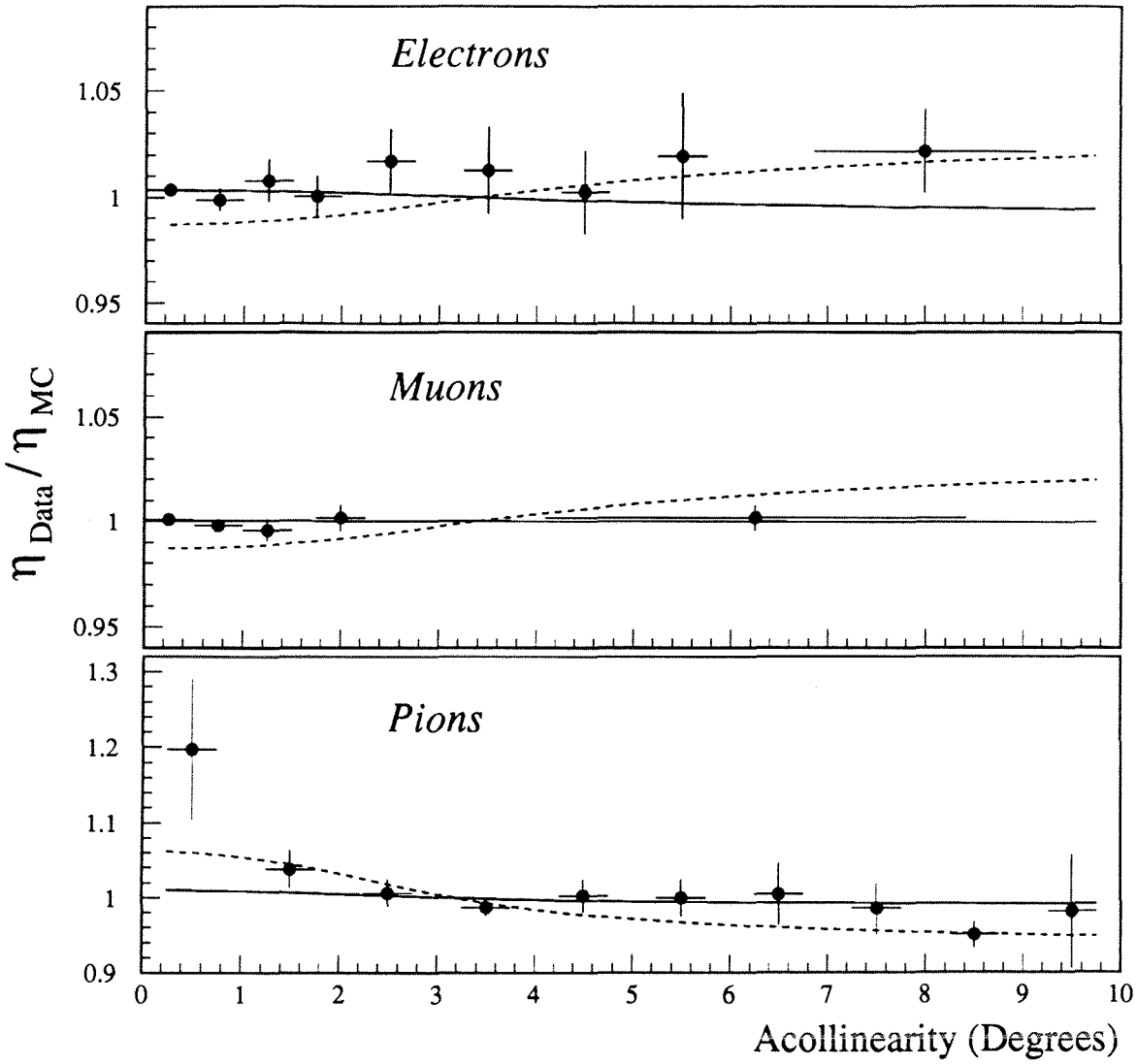

Figure 6.1: *Ratio of 1991 data and Monte Carlo neural network identification efficiency for kinematically identified electrons, muons and pions as a function of the acollinearity. The solid curves indicate the fits to the functional form of the acollinearity distribution of the cross section. The dashed curves illustrate the shift induced by* $\Delta P_\tau = 0.06$.

is very important. The most important properties of such fake photons are the number of fake photons, their energies and their distances to the charged track. These properties have been found to be in good agreement with the generated Monte

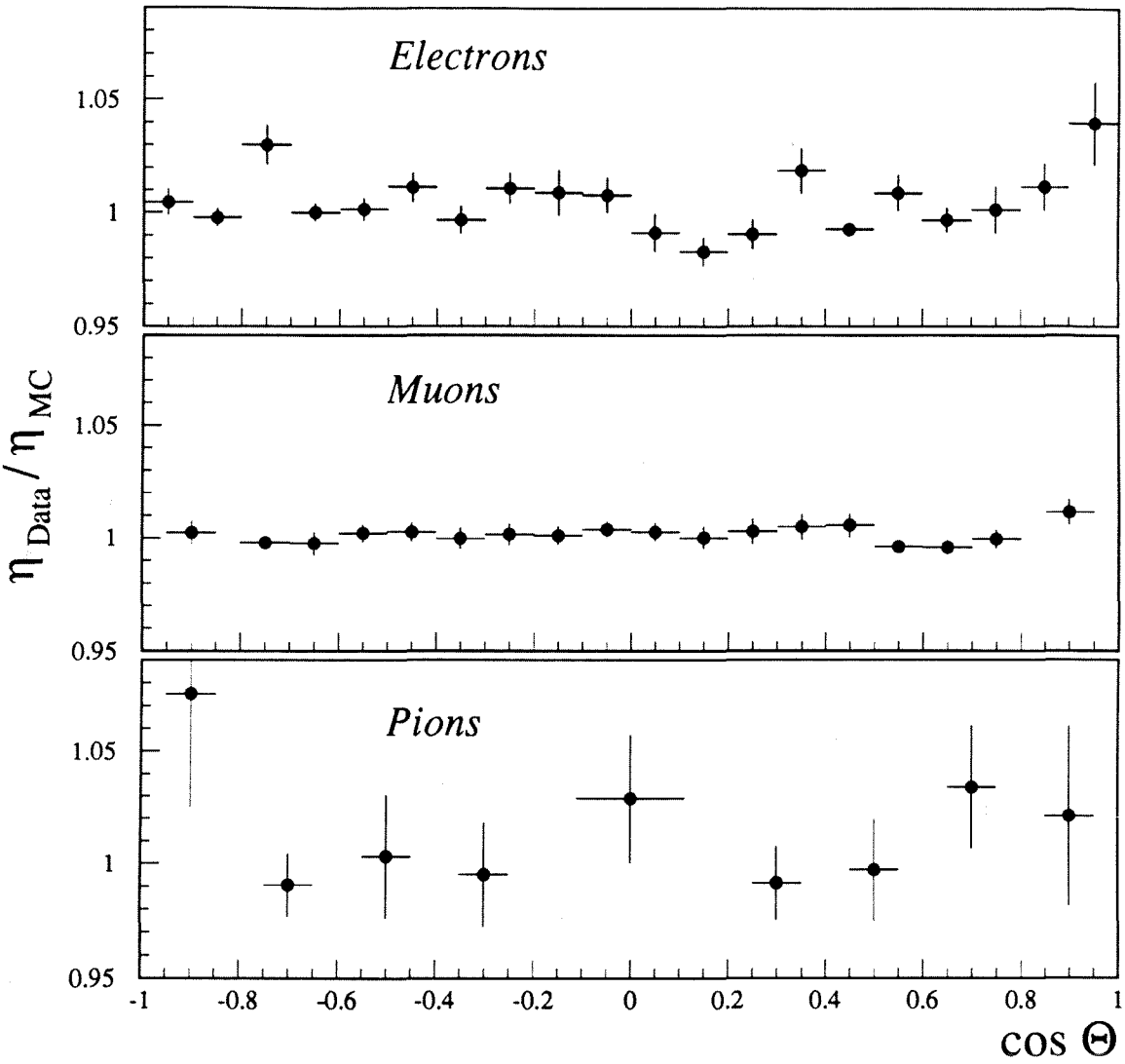

Figure 6.2: *Ratio of the Monte Carlo and data efficiencies as a function of the* $\cos\theta$ *for Bhabha electrons, muon pairs and pions.*

Carlo events. The number of events with zero, one, two and more reconstructed photons show a fairly good agreement between data and Monte Carlo as can be seen in table 6.3.

The acollinearity distributions for identified pions and leptons with various numbers of photons also agree between data and Monte Carlo, as shown in figures 6.3 and 6.4.

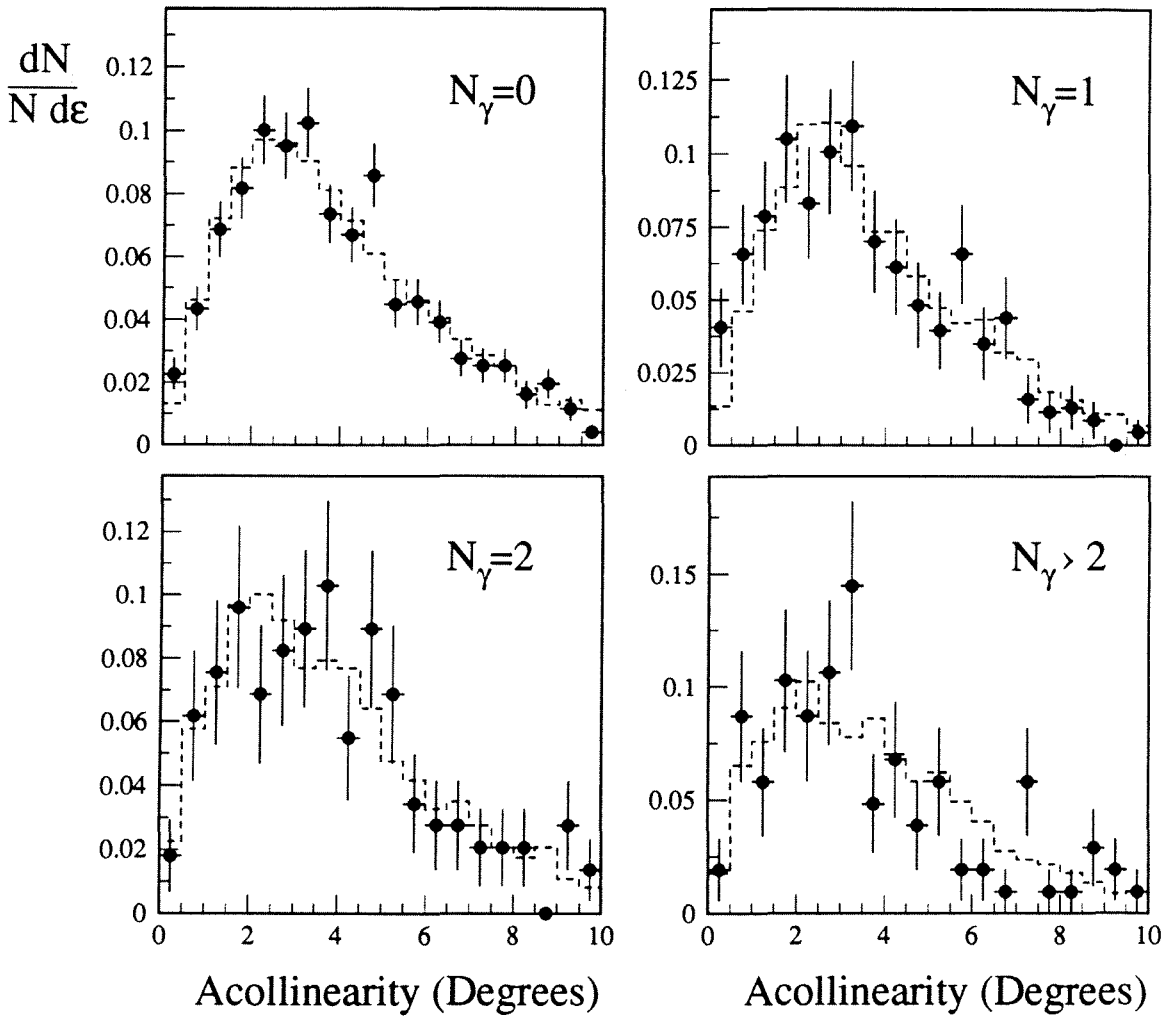

Figure 6.3: *Acollinearity distribution for identified pions with zero, one, two and more reconstructed photons.*

6.2 Background

6.2.1 Tau Background

To see the effect of a change in the background levels on the tau polarization, the normalization and shape of the tau background for the inclusive leptons and pions

Number of photons	$\pi - X$		$l - X$	
	MC	data	MC	data
0	1283	1299	2071	2064
1	337	306	619	650
2	214	205	563	501
> 2	153	173	444	480

Table 6.3: *Number of events with zero, one, two and more reconstructed photons for the inclusive pions and leptons for Monte Carlo and data.*

are varied by changing the tau branching ratios in the Monte Carlo by $\pm 15\%$. Only the effect of the K^* and $\pi\ n\pi^0$ backgrounds has been evaluated by varying their level by $\pm 50\%$. The modified background distributions were obtained by a reweighting procedure of the relative branching ratios. The parameters were refitted after subtracting the modified background distributions. The maximal change in the fitted parameters gives the corresponding systematic error. Table 6.4 shows the different estimated systematic errors for the samples considered.

The dependence on the polarization of the acollinearity distribution of the tau background in both samples has been studied, using the Monte Carlo, by changing the polarization according to its statistical error. No significant effect was found.

6.2.2 Non-Tau Background

Because the backgrounds from non-tau sources have kinematic distributions which differ greatly from those of the tau signal, incorrect normalization or poor modeling of the relevant quantities used to reject these background can induce severe systematic errors in the polarizations measured. However, as described (in the selection chapter 4), the background rejection was performed by cutting on the opposite hemisphere which reduces the non τ-background contributions to a very low level. The systematic uncertainties should then be very small.

There are three different sources of non τ-background considered here: Bhabha events, muons pairs and two-photon processes. The amount of QCD background

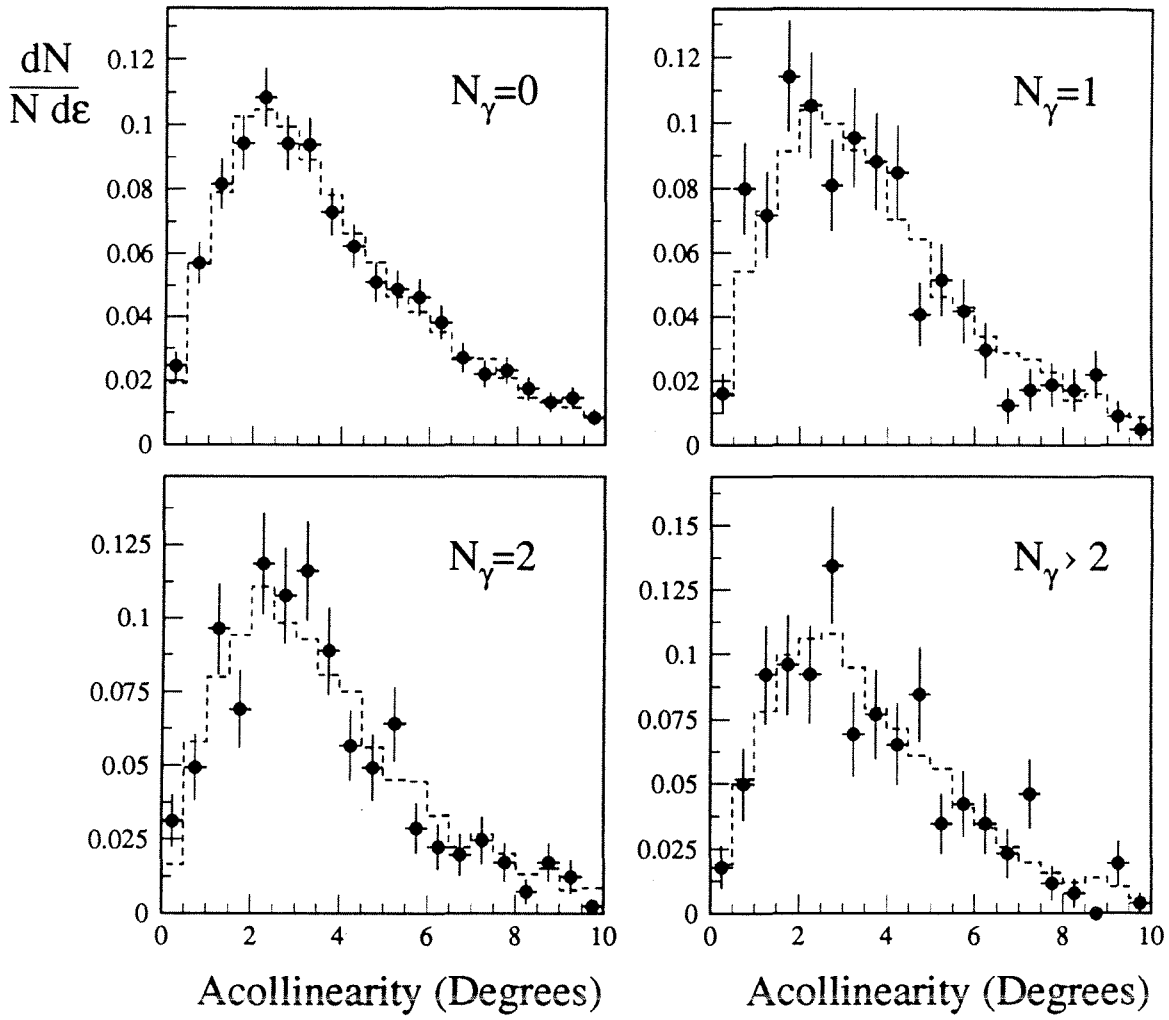

Figure 6.4: *Acollinearity distribution for identified leptons with zero, one, two and more reconstructed photons.*

is found from the Monte Carlo simulation to be completely negligible and for this reason it is not considered further. The Bhabha and muon pair background are peaked at low acollinearity, typically no more than 2 degrees, while the two-photon processes can extend over a wider acollinearity range.

The acollinearity distribution for two-photon processes has been compared for Monte Carlo and data. A sample of two-photon events is selected requiring the in-

variant mass of the event to be smaller than 12 GeV when using all the photons and good tracks inside the acceptance. Figure 6.5 shows the acollinearity distribution for two-photon Monte Carlo events and data up to 10 degrees. The shapes are in good agreement. There is, however, a considerable uncertainty on the size of the cross section and on the trigger acceptance for two-photon interactions. The normalization of the non-tau background was varied by a conservative ±20%, leading to variations of the measured polarizations, which are listed in table 6.4.

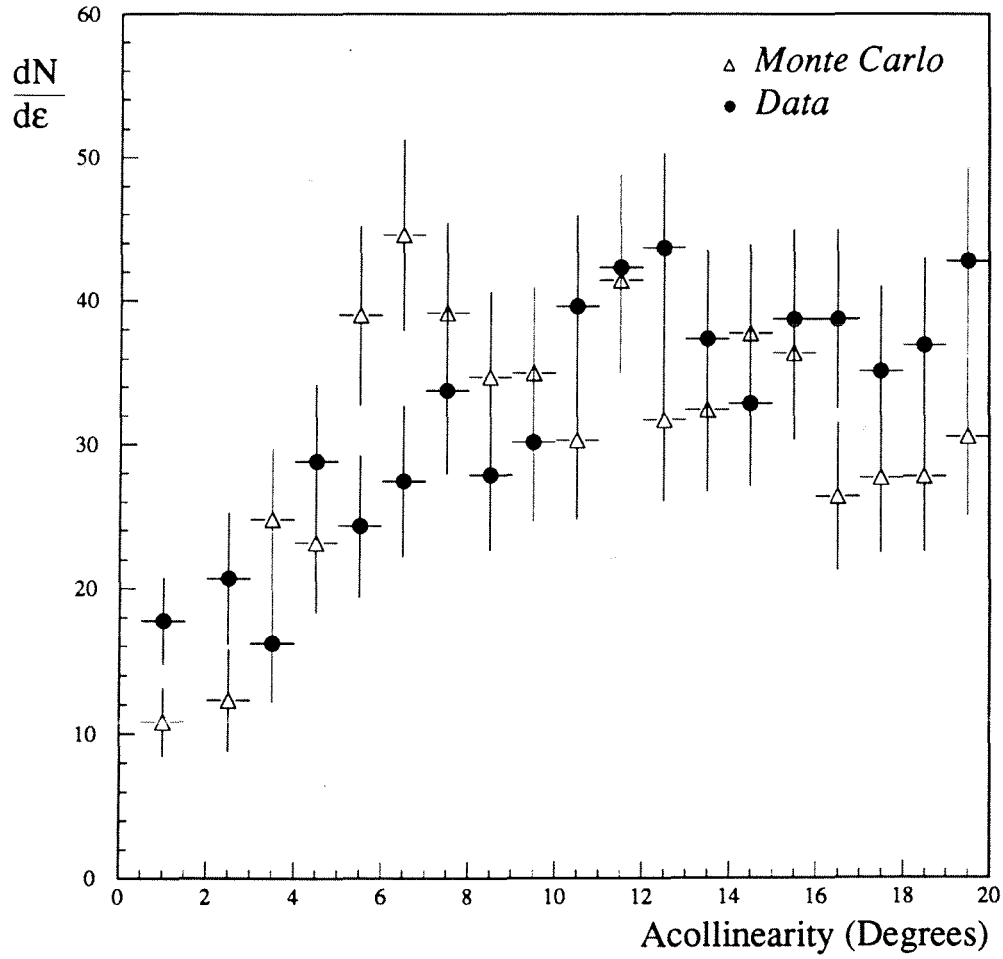

Figure 6.5: *Acollinearity distribution for Monte Carlo and data of two-photon events.*

Selecting muon pairs from Z^0 decays consists on simply taking events with two high momentum oppositely charged tracks and demanding that both tracks be

identified as muons; no discrepancy is found between the acollinearity distribution of Monte Carlo events and of data, as can be seen in figure 6.6.

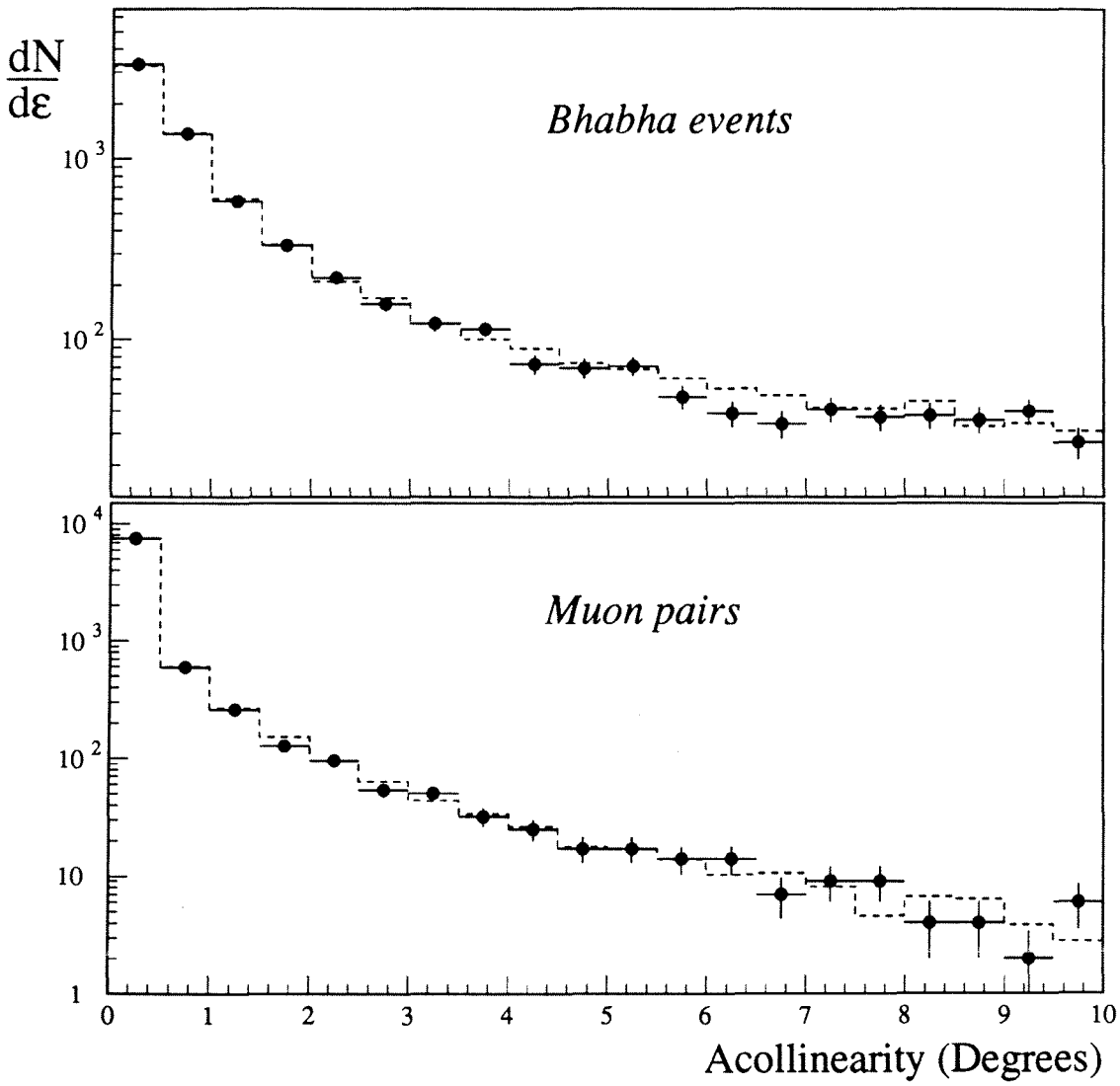

Figure 6.6: *Acollinearity distributions for Bhabha and dimuon events. The error bars are the selected data, whereas the dashed line corresponds to the Monte Carlo.*

Concerning the acollinearity distribution of Bhabha events, it is well known that the cut-off of the energy of the radiated photons and that including only $\mathcal{O}(\alpha)$ photon radiative effects shifts the acollinearity distribution for Monte Carlo events to slightly higher values of acollinearity [53]. A closer look at the Bhabha

source	$d\sigma/d\varepsilon$		$A_{FB}(\varepsilon)$	
	$\pi - X$	$l - X$	$\pi - X$	$l - X$
τ backgrounds	0.005	0.005	0.003	0.006
non-τ backgrounds	0.007	0.002	0.005	0.005
misidentification	0.001	0.001	0.001	0.001

Table 6.4: *Systematic errors on polarization from background sources. Here the column labelled "$d\sigma/d\varepsilon$" gives the errors on $\mathcal{A}_{e-\tau}$ from the acollinearity dependence of the cross section, and the column labelled "$A_{FB}(\varepsilon)$" gives the errors on $\mathcal{A}_{e-\tau}$ from the asymmetry $A_{FB}(\varepsilon)$.*

events shows that the Monte Carlo acollinearity distribution agrees with that of the data for Bhabha events when there is at least one charged track in the event with a momentum smaller than 40 GeV. Looking at the momenta distribution of the Bhabha background which enters in the inclusive pion and lepton samples reveals that most of this Bhabha background has a track with a momentum smaller than 40 GeV. This is due to the presence of a radiative photon whose shower overlaps the one from the electron and, therefore the electron track is identified wrongly as a pion. The acollinearity distributions for the selected Bhabha events in Monte Carlo and data are plotted in figure 6.6. Conservatively, the normalization for the Bhabha and muon pairs background was varied by $\pm 20\%$.

In fact, the last paragraph raises an important point about the misidentification probabilities. Only misidentification between pions and either electron or muons can induce a sizeable effect. The misidentification of electrons as muons and vice versa is irrelevant since the samples defined are both inclusive over leptons. In order to check these misidentifications, the probabilities to identify an electron as a pion in the data and in the Monte Carlo have been computed, using the previously described kinematically-selected electrons that are identified as pions by the neural network. The same exercise is repeated for the four different possibilities. Figure 6.7 shows the acollinearity distribution of electrons identified as pions and muons identified as pions for Monte Carlo and kinematically-selected data. A discrepancy has been found only for the probability to identify electrons as pions. For those misidentified events, this discrepancy also shows up in the energy distribution. With

the present statistics a discrepancy is not confirmed for muons identified as pions. For this reason an *ad hoc* correction has been applied to the Bhabha background before fitting the polarization. This correction is varied in the fit in order to estimate the systematic error coming from this misidentification problem, which is shown in table 6.4.

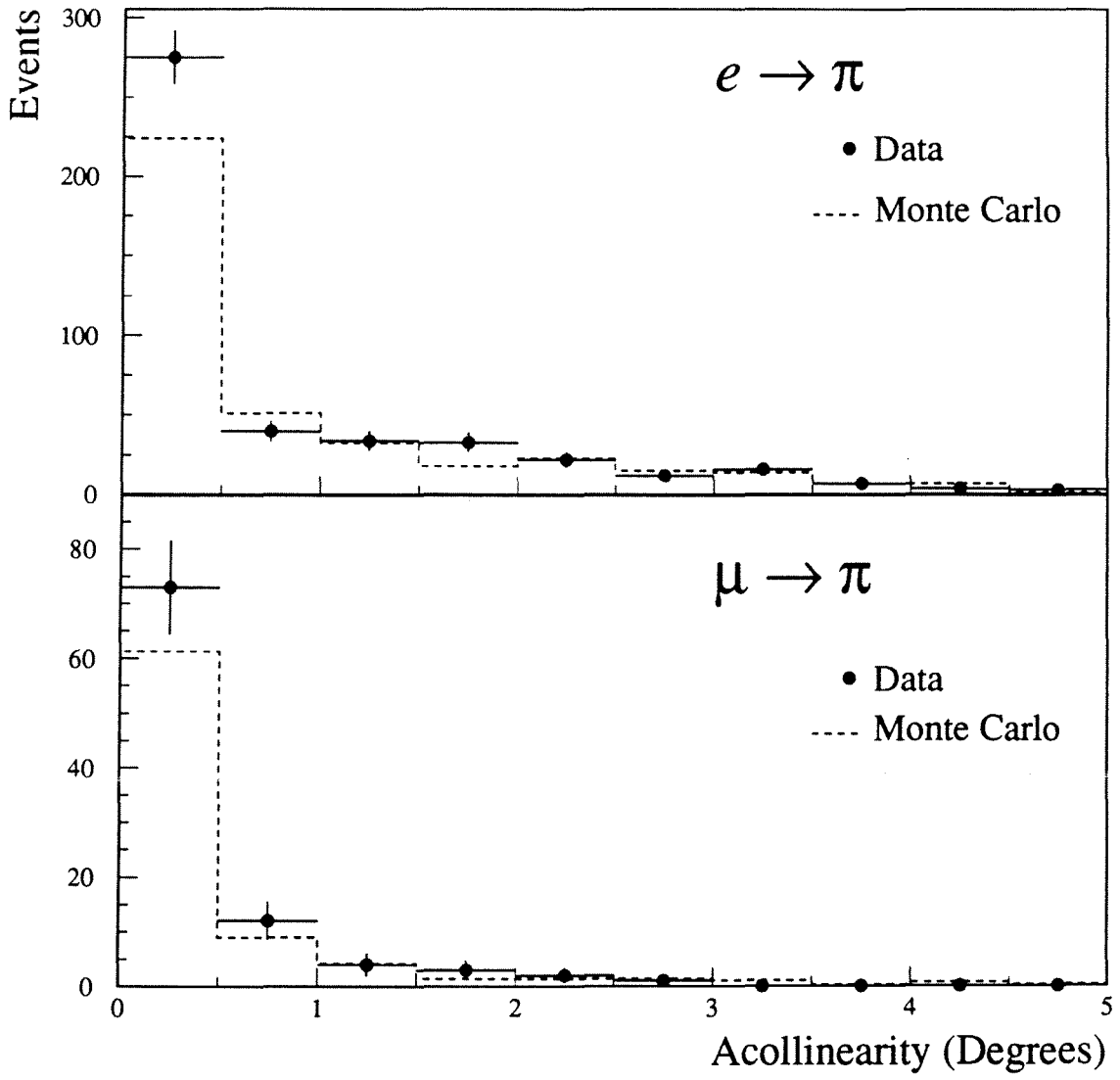

Figure 6.7: *Acollinearity distributions of electrons identified as pions and muons identified as pions for Monte Carlo and data.*

6.3 Tracking Uncertainties

The acollinearity angle distribution is measured exclusively from track angles. Therefore, detector effects in the acollinearity are largely independent from those of the single-tau measurement which relies mainly on energy measurements.

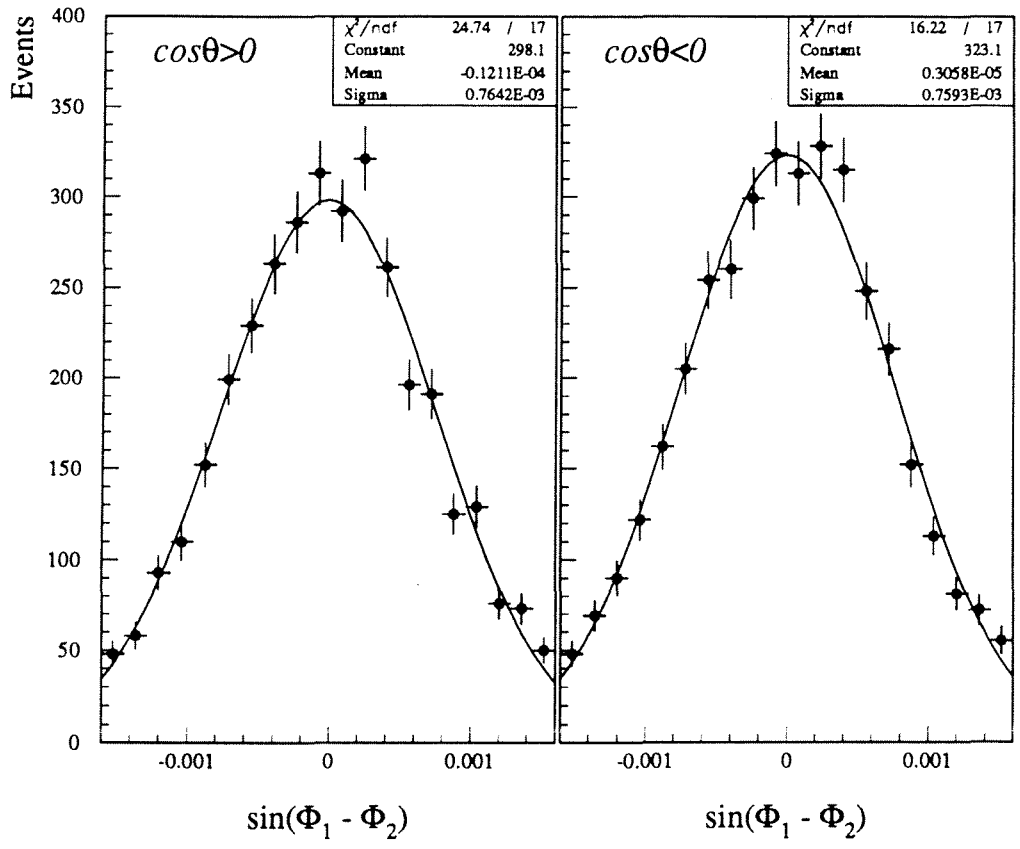

Figure 6.8: *Projection of the difference of the azimuthal angles* $\sin(\Delta\phi)$ *for muon pairs in the forward and backward hemispheres.*

The acollinearity angle, as defined previously, depends on the measurement of the polar and azimuthal angles of the two charged tracks. A possible rotation of the TPC endplates, leading to shifts in the azimuthal angles (ϕ_+ for the positive muon track and ϕ_- for the negative one), is studied using $Z^0 \to \mu^+\mu^-$ events and is found to be smaller than 0.04 mrad. Figure 6.8 shows the $\sin(\Delta\phi)$ for muons pairs

	$d\sigma/d\varepsilon$		$A_{FB}(\varepsilon)$	
source	$\pi - X$	$l - X$	$\pi - X$	$l - X$
tracking	0.001	0.003	0.006	0.003

Table 6.5: *Systematic errors on polarization from tracking. "$d\sigma/d\varepsilon$" gives the errors on $\mathcal{A}_{e-\tau}$ from the acollinearity dependence of the cross section, and "$A_{FB}(\varepsilon)$" gives the errors on $\mathcal{A}_{e-\tau}$ from the forward-backward asymmetry.*

selected from the data, where $\Delta\phi = \phi_+ - \phi_-$. The systematic uncertainty from such a rotation of the TPC endplates has been computed by applying a rotation of 0.04 mrad to the transverse momentum of one track and reevaluating the acollinearity angle. The shift observed on the value of the polarization after refitting is considered as the systematic error, which is found to be negligible.

The TPC drift velocity v_{drift}, which enters directly into the determination of the polar angle θ,

$$\tan\theta \;\propto\; \frac{1}{v_{drift}}\,, \tag{6.5}$$

is known to an accuracy of 3.5×10^{-4}, by comparing the θ of the track measured by the vertex detector with the θ measured for the TPC track. This implies a relative uncertainty in the component of the track momentum along the drift direction of the same size and can affect the acollinearity. Therefore, the momentum component along the z axis has been shifted according to

$$p_z \rightarrow\; p_z \left(\, 1 + \frac{\Delta v_{drift}}{v_{drift}} \,\right). \tag{6.6}$$

The acollinearity is computed again with the shifted p_z component, and the polarization is refitted. The changes of the polarization are listed in table 6.5.

Beyond the angular range $|\cos\theta| < 0.8$ however, the data manifest a discrepancy between positive and negative muons such that the mean momentum for positive muons exceeds that of the beam by 1 GeV, and the opposite for negative muons. This behaviour cannot be corrected as in this the angular range there are no laser measurement to correct the transverse drift velocity. The effect can be written as

$$\frac{1}{p} \rightarrow \frac{1}{p} - \frac{Q}{|\beta|}\,, \tag{6.7}$$

source	$d\sigma/d\varepsilon$		$A_{FB}(\varepsilon)$	
	$\pi - X$	$l - X$	$\pi - X$	$l - X$
C_i^{Rad}	0.007	0.004	0.007	0.004
Branching Ratios	0.008	0.014	0.001	0.001
theoretical	0.001	0.001	0.001	0.001

Table 6.6: *Systematic errors on polarization from the theoretical uncertainties.*

where Q is the electric charge of the particle and β is a constant equal to 2000 GeV/c. While this is a momentum effect, it causes a distortion of the azimuthal angles. Fortunately, as it has opposite effects for positive and negative tracks, the effects on the azimuthal angles produces a global shift that does not affect $\Delta\phi$. A study of the effect on the acollinearity, using muon pairs, shows that these distortions cause a negligible effect.

6.4 Branching Ratios and Theoretical Uncertainties

One main source of uncertainty arises from the slight dependence on P_τ observed in the determination of the C_i^{rad} coefficients used in the fitting procedure. For this purpose a large sample of events (1.4×10^7 tau pairs) is produced at the generator level to determine these coefficients, thus reducing the Monte Carlo statistical fluctuation to an insignificant level. The systematic uncertainty quoted in table 6.6 is derived by varying the value of P_τ to obtain the coefficients, by the statistical error of the measurement. Other effects on C_i^{rad}, such as variations in the branching ratios, have been found to be negligible.

As the event samples used are inclusive, uncertainties in the branching ratios, needed to compute the theoretical acollinearity distributions as described in equation 5.5, lead to systematic uncertainties in the theoretical predictions. These branching ratios are taken from the ALEPH measurements with their overall errors [75]. Allowing these branching ratios to fluctuate simultaneously inside the quoted errors gives an estimation of this systematic error, as shown in table 6.6.

Finally, the uncertainties in the input masses in the Q functions, which are not negligible for the a_1 case, lead to theoretical uncertainties in the computation of equations 5.1 and 5.2. Refitting the data with Q functions computed with shifted inputs masses by their uncertainties contributes less than 0.001 to the systematic errors.

6.5 Summary of Main Systematic Errors

The major contributions to the systematic errors on the polarization measured from the acollinearity distributions appear in table 6.7 concerning the parameter $\mathcal{A}_{e-\tau}$ and in table 6.8 for those entering in $\mathcal{A}_e$ and $\mathcal{A}_\tau$. They come from the determination of the selection efficiencies, the correction coefficients, the detector effects and branching ratios. In addition, on these tables the Monte Carlo statistical errors are shown, which have been computed by fitting the data with and without the propagation of the Monte Carlo statistical precision in the coefficients appearing in equation 6.2. The quadratic difference of the errors of the fits represents the Monte Carlo statistical error.

The final computation of the systematic errors on the parameters $\mathcal{A}_e$, $\mathcal{A}_\tau$ and $\mathcal{A}_{e-\tau}$, for the simultaneous fit to the acollinearity distribution of the cross section and its forward-backward asymmetry was done assuming that in a given inclusive sample the systematic error from the cross section was fully correlated with the one coming from its asymmetry; but completely uncorrelated with the other inclusive sample. The final systematic errors are shown in table 6.9, which do not include the contribution of the Monte Carlo statistics because it was already included in the statistical part of the error in the corresponding tables given in chapter 5.

A similar procedure has been followed to determine the systematic error of the measurement of the polarization in the forward and backward hemispheres independently. It has been assumed that the systematic error in the acollinearity distribution of the cross section (integrated over $\cos\theta$) is the same in the forward and backward hemispheres; but uncorrelated from one inclusive sample to the other. Then a fit minimizing a χ^2 which includes a full correlation matrix of the two points entering in the fit,

$$\chi^2 = \sum_{ij} \left(P_\tau(\cos\theta)_i - A_i\right) V_{ij}^{-1} \left(P_\tau(\cos\theta)_j - A_j\right) , \qquad (6.8)$$

source	$d\sigma/d\varepsilon$		$A_{FB}(\varepsilon)$	
	$\pi - X$	$l - X$	$\pi - X$	$l - X$
$C^{rad}(P_\tau)$	0.007	0.004	0.007	0.004
selection	0.008	0.008	0.001	0.001
backgrounds	0.009	0.005	0.006	0.008
branching ratios	0.008	0.014	0.001	0.001
tracking	0.001	0.003	0.006	0.003
subtotal	0.016	0.018	0.011	0.009
MC statistics	0.017	0.023	0.015	0.012
total	0.023	0.029	0.019	0.015

Table 6.7: *Summary of systematic errors on polarization from the acollinearity method. Here the column labelled "$d\sigma/d\varepsilon$" gives the errors on $\mathcal{A}_{e-\tau}$ obtained from the acollinearity dependence of the cross section, and the column labelled "$A_{FB}(\varepsilon)$" gives the errors on $\mathcal{A}_{e-\tau}$ obtained from the asymmetry $A_{FB}(\varepsilon)$.*

where $P_\tau(\cos\theta)_i$ is the measured polarization in bin i of $\cos\theta$ shown in table 5.4, A_i is the predicted polarization in bin i of $\cos\theta$ given by equation 5.4 and V_{ij} is the covariance matrix

$$V_{ij} = \rho_{ij}^{stat}\sigma_i^{stat}\sigma_j^{stat} + \rho_{ij}^{sys}\sigma_i^{sys}\sigma_j^{sys} \ , \tag{6.9}$$

where

$$\rho_{ij}^{sys} = 1, \ \ \forall\, ij; \qquad \rho_{ij}^{stat} = \begin{cases} 1 & \text{if } i = j, \\ 0 & \text{if } i \neq j. \end{cases} \tag{6.10}$$

The off-diagonal elements elements simply reflect the non-random systematic errors, assumed to be fully correlated. The quadratic difference between the total error on the fit parameter A and the statistical part of that error is taken as the systematic error on the parameter. The results obtained were the same that those of table 6.9.

source	$A_{FB}(\varepsilon)$			
	$\pi - X$		$l - X$	
	$\mathcal{A}_e$	$\mathcal{A}_\tau$	$\mathcal{A}_e$	$\mathcal{A}_\tau$
$C^{rad}(P_\tau)$	0.001	0.007	0.002	0.005
selection	0.001	0.001	0.001	0.001
backgrounds	0.001	0.008	0.005	0.009
branching ratios	0.001	0.002	0.001	0.001
tracking	0.001	0.005	0.001	0.003
subtotal	0.003	0.012	0.005	0.011
MC statistics	0.014	0.086	0.028	0.031
total	0.014	0.087	0.029	0.033

Table 6.8: *Summary of systematic errors on polarization from the forward-backward asymmetry as a function of the acollinearity. Here the column labelled "$A_{FB}(\varepsilon)$" gives the errors on $\mathcal{A}_e$ and $\mathcal{A}_\tau$ obtained from the asymmetry $A_{FB}(\varepsilon)$.*

parameter	systematic error
$\mathcal{A}_\tau$	0.011
$\mathcal{A}_e$	0.002
$\mathcal{A}_{e-\tau}$	0.009

Table 6.9: *Final systematic errors on polarization parameters from combined analysis.*

Chapter 7

Electroweak Parameter Results

7.1 Including Single-Tau Method Results

The measurement of the tau polarization through the energy spectra and other kinematic variables describing the decay of a single tau is called single-tau method as in reference [77]. Its correlation with the acollinearity method is described in this section.

7.1.1 Results from Single-Tau Method

Two other measurements of the tau polarization have been done in ALEPH using the kinematic variables of the decay, without correlations [77]. Five different channels have been analyzed: electron, muon, pion, rho and a_1. For the lepton and pion decay channels only the energy spectra are used. For the rho and a_1 channels, all the kinematic variables describing their decay are exploited through an optimal ω variable which has been defined in [10]. In addition to the average polarization over $\cos\theta$ for those channels, the forward backward polarization asymmetry is measured. Tables 7.1 and 7.2 show the results obtained for the corrected parameters $\mathcal{A}_e$, $\mathcal{A}_\tau$ and $\mathcal{A}_{e-\tau}$ and the derived systematic errors for the different channels.

It is interesting to point out that for the single-tau method, the channels that have the largest weights in the combination, mainly the rho and pion channels, have essentially reached the systematic limit.

parameter	method CC	method NN
$\mathcal{A}_e$	$0.117 \pm 0.026 \pm 0.008$	$0.122 \pm 0.026 \pm 0.008$
$\mathcal{A}_\tau$	$0.141 \pm 0.019 \pm 0.014$	$0.145 \pm 0.019 \pm 0.014$
$\mathcal{A}_{e-\tau}$	$0.130 \pm 0.016 \pm 0.009$	$0.137 \pm 0.016 \pm 0.009$

Table 7.1: *Corrected polarization parameters extracted from polar angle fit single-tau methods with their statistical and systematic errors. The label CC stands for the classical cut method identifying particles, whereas the label NN refers to neural network approach.*

error	$e\nu\overline{\nu}$	$\mu\nu\overline{\nu}$	$\pi\nu$	$\rho\nu$	$a_1\nu$
acceptance	0.011	0.012	0.016	0.024	0.014
tau background	0.016	0.012	0.010	0.007	0.010
other background	0.012	0.008	0.002	0.003	-
energy calibration	0.032	0.014	0.001	0.012	0.001
model dependence	-	-	-	-	0.012
Monte Carlo statistics	0.021	0.017	0.008	0.010	0.020
total systematic error	0.045	0.029	0.018	0.030	0.029

Table 7.2: *Summary of systematic errors on $\mathcal{A}_\tau$ for each decay channel, for the single-tau method.*

7.1.2 Correlation between Single-Tau and Acollinearity Results

An important point in the measurement of P_τ from the spin angular correlations is that it is not independent from the value of P_τ from the energy spectra. This is due to the fact that the acollinearity angle and the energy of the decay products are correlated. This correlation is stronger when the tau decay is two-body.

To combine both measurements the BLUE technique (Best Linear Unbiased Estimate) is used, which requires the calculation of the correlation coefficient [76].

Given several estimates P_{τ_i} of the same physical quantity P_τ, and the corresponding error matrix E_{ij}, the desired estimator $\hat{P}_\tau$ is such that:

- is a linear combination of the different estimators ($\hat{P}_\tau = \sum_i \alpha_i \cdot P_{\tau_i}$),
- is an unbiased estimate of P_τ, and
- its variance is the minimum possible.

The problem can be solved by finding the N values of α_i which minimize the variance subject to the constraint $\sum_i \alpha_i = 1$. Using Lagrangian multipliers is possible to derive

$$\vec{\alpha} = \frac{E^{-1}\vec{u}}{\vec{u}^T E^{-1}\vec{u}}, \tag{7.1}$$

where $u_i = 1$ for every i. The values of $\hat{P}_\tau$ and σ^2 can be determined from $\vec{\alpha}$. When there is no correlation between measurements, this method is equivalent to the standard method of combining results with weights equal to the reciprocal of the variances.

To estimate the correlation a series of 100 hypothetical experiments are created by means of Monte Carlo generation of 100 independent samples of events. The events at the generator level were analyzed to obtain values of P_τ from the combination of the analysis based on energy spectra of electrons, muons, pions and rhos and from acollinearity distributions of inclusive samples.[4]

Then, the elements of the error matrix E are given by

$$E_{ij} = \frac{1}{100}\sum_{k=1}^{100}\left(P_{ik} - \bar{P}_i\right)\left(P_{jk} - \bar{P}_j\right), \tag{7.2}$$

where i and j refer to the method used to determine the average polarization, k denotes the Monte Carlo experiment and

$$\bar{P}_i = \frac{1}{100}\sum_{k=1}^{100} P_{ik}. \tag{7.3}$$

The correlation coefficient relating the errors on the acollinearity and single-tau measurements is calculated to be 0.5 when the measurements are performed on

[4]The a_1 channel was not included because of the exclusivity of events used in the single-τ method (3-prong a_1 decay) and the acollinearity method (1-prong a_1 decay).

the same sample. The actual correlation coefficient between the single-tau and the acollinearity results is 0.3, since the acollinearity measurement is made only for data collected at the peak of the Z^0 resonance.

7.1.3 Combined Results

The values of $\mathcal{A}_e$, $\mathcal{A}_\tau$, and $\mathcal{A}_{e-\tau}$ from the single-tau and acollinearity methods can be combined in a weighted average, taking into account the correlations between them [76]. These combined values will in turn be combined with other ALEPH measurements, in particular the forward-backward charge asymmetry, to obtain electroweak parameters. It is for this reason that only the values of $\mathcal{A}_e$, $\mathcal{A}_\tau$, and $\mathcal{A}_{e-\tau}$ from the acollinearity distributions in the forward and backward hemispheres (given in section 5.3.4), which are almost uncorrelated with the forward-backward charge asymmetry, are used in the averaging. These are the values chosen for publication by the ALEPH collaboration in reference [77].

The correlation of the single-tau and acollinearity systematic errors is negligible. The following C_{stat} and C_{sys} matrices summarize the correlations between statistical and systematic errors among the single-tau and acollinearity method results. The first row denotes the single-tau energy method using a neural net identification, the second row the single-tau method using conventional cuts, and the third row the acollinearity method.

$$C_{stat} = \begin{pmatrix} 1. & 0.81 & 0.3 \\ 0.81 & 1. & 0.24 \\ 0.3 & 0.24 & 1. \end{pmatrix}, \qquad C_{sys} = \begin{pmatrix} 1. & 1. & 0. \\ 1. & 1. & 0. \\ 0. & 0. & 1. \end{pmatrix}.$$

The final combined results appear in Table 7.3, where the statistical errors of table 7.1 have been increased by 2.3% since the helicity correlations have been ignored in the single-tau method, which leads to a systematic underestimation of the statistical error on $\mathcal{A}_e$, $\mathcal{A}_\tau$, and $\mathcal{A}_{e-\tau}$.

With the present statistical and systematic errors the acollinearity method carries little weight in the final number. However, the method uses independent observables and thus has independent systematics. Those systematics, which come

parameter	combined result
$\mathcal{A}_e$	$0.121 \pm 0.025 \pm 0.008$
$\mathcal{A}_\tau$	$0.143 \pm 0.019 \pm 0.013$
$\mathcal{A}_{e-\tau}$	$0.134 \pm 0.015 \pm 0.009$

Table 7.3: *Polarization parameters extracted from polar angle dependence, combining the single-tau method results with that of the acollinearity method. The first error is statistical and the second is systematic.*

mainly from measurements of angles, are similar in size to those of the energy method. Therefore the value of including the acollinearity information increases with the increasing statistical power of the data.

7.2 Electroweak Parameters

The results presented so far are the basic physical quantities measured in this analysis of the polarization of taus in Z^0 decay. They are compatible with and improve the previous published ALEPH results [71] as well as the results from other LEP experiments [3]. The comparison of $\mathcal{A}_e$ and $\mathcal{A}_\tau$ shows that universality between the electron and the tau in neutral currents holds well.

7.2.1 Electroweak Parameters from Acollinearity

Combining in quadrature the statistical error from table 5.3 and the systematic errors from table 6.9 from the acollinearity distributions and from the forward-backward asymmetry measurements, one gets:

$$\mathcal{A}_e = 0.130 \pm 0.063 \,, \tag{7.4}$$

$$\mathcal{A}_\tau = 0.162 \pm 0.053 \,, \tag{7.5}$$

$$\mathcal{A}_{e-\tau} = 0.148 \pm 0.036 \,. \tag{7.6}$$

From those values one can infer [5] the ratios of the vector and axial-vector cou-

[5]The sign ambiguity in g_V and g_A is resolved on the basis of low energy data [78].

plings of the Z^0 to leptons by using the relation

$$\mathcal{A}_l \equiv 2\frac{g_V^l g_A^l}{(g_V^l)^2 + (g_A^l)^2} \ . \tag{7.7}$$

The results obtained are

$$\frac{g_V^e}{g_A^e} = +0.065 \pm 0.032 \ , \tag{7.8}$$

$$\frac{g_V^\tau}{g_A^\tau} = +0.082 \pm 0.027 \ , \tag{7.9}$$

$$\frac{g_V^{e-\tau}}{g_A^{e-\tau}} = +0.074 \pm 0.018 \ . \tag{7.10}$$

Using the relation

$$\sin^2\theta_W^{\rm eff} = \frac{1}{4}\left(1 - \frac{g_V^{e-\tau}(M_Z^2)}{g_A^{e-\tau}(M_Z^2)}\right), \tag{7.11}$$

and the result of equation 7.10, the effective weak mixing angle at the Z^0 mass can be inferred as

$$\sin^2\theta_W^{\rm eff} = 0.2314 \pm 0.0046 \ . \tag{7.12}$$

Notice that in equation 7.11, $\sin^2\theta_W^{\rm eff}$ is such that it includes all deviations from the tree-level couplings. This definition has been used on reference [4], and it causes the value of $\sin^2\theta_W^{\rm eff}$ to differ from $\sin^2\theta_W(M_Z^2)$ by -0.0007. The definition of $\sin^2\theta_W(M_Z^2)$ is in principle flavour dependent due to electroweak vertex corrections, but the flavour dependent corrections are small enough to be ignored here.

7.2.2 Electroweak Parameters from Combined Results

Combining the statistical and systematic errors in quadrature from table 7.3 for the combined measurements from the acollinearity method and the single-tau method, one gets:

$$\mathcal{A}_e = 0.121 \pm 0.026 \ , \tag{7.13}$$

$$\mathcal{A}_\tau = 0.143 \pm 0.023 \ , \tag{7.14}$$

$$\mathcal{A}_{e-\tau} = 0.134 \pm 0.018 \ . \tag{7.15}$$

From those values one can infer the ratios of the vector and axial-vector couplings of the Z^0 to leptons by using the relation of equation 7.7, with the results

$$\frac{g_V^e}{g_A^e} = +0.060 \pm 0.013 , \tag{7.16}$$

$$\frac{g_V^\tau}{g_A^\tau} = +0.072 \pm 0.012 , \tag{7.17}$$

$$\frac{g_V^{e-\tau}}{g_A^{e-\tau}} = +0.067 \pm 0.009 . \tag{7.18}$$

The electron-tau universality in the neutral currents is at the level of

$$\frac{g_V^e/g_A^e}{g_V^\tau/g_A^\tau} = 0.85 \pm 0.27. \tag{7.19}$$

The ambiguity in magnitude between $g_V^{e-\tau}$ and $g_A^{e-\tau}$ can be removed using the partial width for leptons, given by

$$\Gamma_l = \frac{G_F M_Z^3}{6\sqrt{2}\pi} (g_V^l + g_A^l)(1 + \frac{3\alpha}{4\pi}) . \tag{7.20}$$

The ALEPH values for the lepton partial widths, which have been published in reference [73],

$$\Gamma_e = 84.43 \pm 0.60 \text{ MeV} , \tag{7.21}$$

$$\Gamma_\tau = 84.09 \pm 1.10 \text{ MeV} , \tag{7.22}$$

yield the solutions for the electron couplings using Γ_e and equation 7.16 and similarly for the τ couplings using Γ_τ and equation 7.17

$$g_V^e = +0.030 \pm 0.0067 , \tag{7.23}$$

$$g_A^e = +0.503 \pm 0.0062 , \tag{7.24}$$

$$g_V^\tau = +0.036 \pm 0.0059 , \tag{7.25}$$

$$g_A^\tau = +0.502 \pm 0.011 . \tag{7.26}$$

The Z^0 axial couplings are known to verify universality to high precision [4, 73] through measurement of the Z^0 partial decay widths. This result extends the information to the vector couplings. Assuming universality the partial width $\Gamma_{e-\tau}$

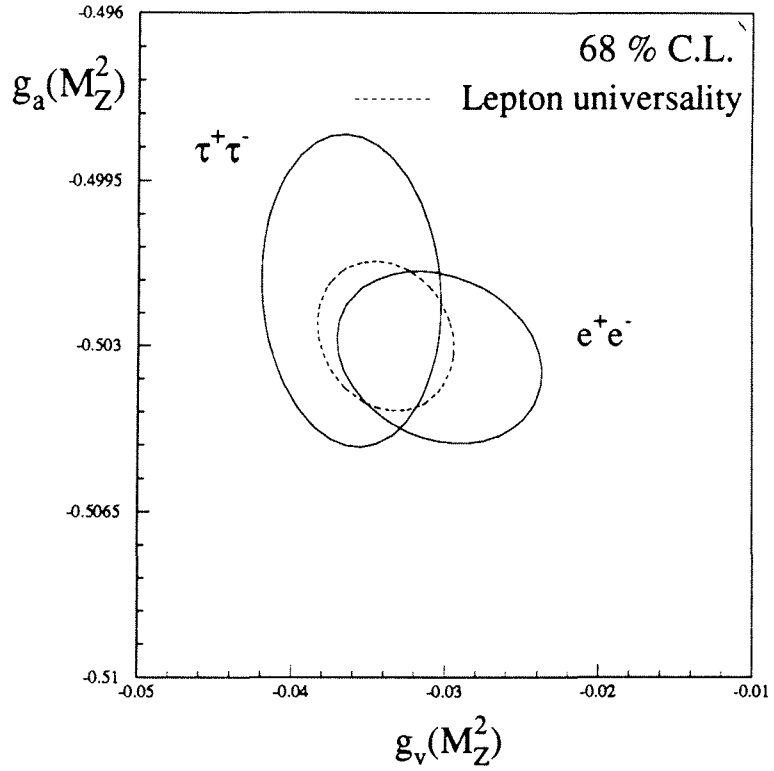

Figure 7.1: *Contours of constant χ^2 for $g_V(M_Z^2)$ and $g_A(M_Z^2)$ from the tau polarization and the partial widths.*

is computed as the independent average of the values of 7.21 and 7.22. [6] Combining with $\mathcal{A}_{e-\tau}$ from expression 7.15 yields

$$g_V^{e-\tau} = +0.034 \pm 0.0045 \ , \tag{7.27}$$

$$g_A^{e-\tau} = +0.503 \pm 0.0054 \ . \tag{7.28}$$

The probability contours at 68% confidence level for $g_V(M_Z^2)$ and $g_A(M_Z^2)$ for each lepton species are shown in figure 7.1. The results assuming lepton universality are also plotted.

Using the relation given by equation 7.11 and the result of equation 7.18, the effective weak mixing angle at the Z^0 mass can be inferred as

[6] The correlation between these both measurements, Γ_e and Γ_τ, is found to be negligible (1%) for the data sample considered in this analysis.

$$\sin^2\theta_W^{\rm eff} = 0.2332 \pm 0.0022 \ . \tag{7.29}$$

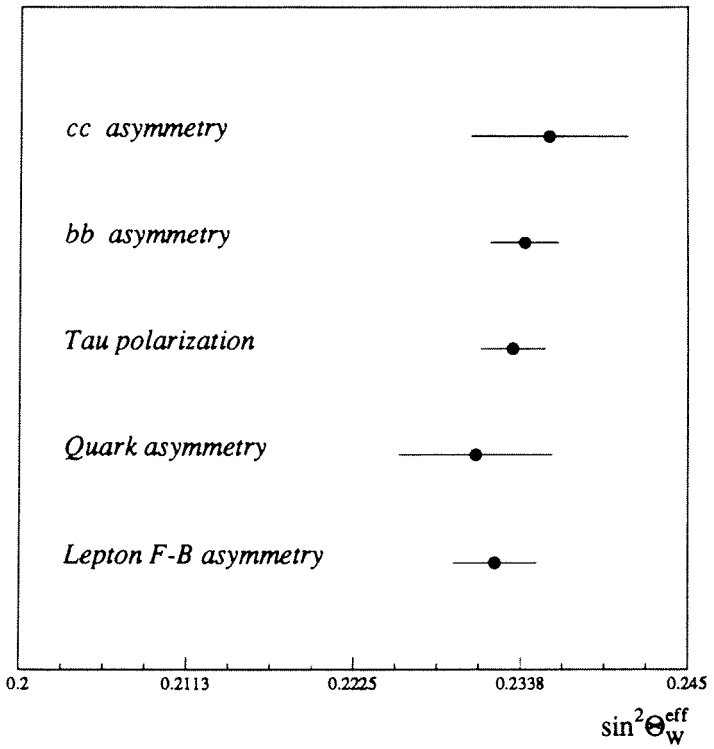

Figure 7.2: *Results of ALEPH measurements of* $\sin^2\theta_W^{\rm eff}$ *from asymmetries and tau polarization.*

Finally, the different measurements in ALEPH sensitive to $\sin^2\theta_W^{\rm eff}$ are shown in figure 7.2. They correspond to the lepton forward-backward charge asymmetry, the quark charge asymmetry, the $b\bar{b}$ and $c\bar{c}$ forward-backward asymmetry. It can be noted that the precision on $\sin^2\theta_W^{\rm eff}$ brought by the tau polarization measurements compares favorably with the other determinations.

Chapter 8

Conclusions

A new method is developed to measure the tau and electron electroweak couplings from the angular correlations in tau pair events. Its theoretical formulation, assuming the V-A structure in the tau decay, is developed as a function of the acollinearity angle of the tau decay products. The observables of main interest to extract a measurement of the electroweak couplings are presented. The most relevant ALEPH subdetectors for the angular measurements and for the event selection are described. The channel classification and inclusive categories selected are also given. The corrections of the acollinearity distributions for the instrumental and selection effects and the fitting procedures employed in this analysis have been described as well.

Several sets of observables from the acollinearity distributions are analyzed and their correlations discussed. The experimental and theoretical systematic uncertainties affecting the acollinearity distributions are presented. The combined results for $\mathcal{A}_l = 2g_V^l g_A^l/[(g_V^l)^2 + (g_A^l)^2]$ from the acollinearity distributions and the forward-backward asymmetry of the acollinearity distributions, using 11.2 pb^{-1} of data collected in 1990 and 1991 in the ALEPH detector at the Z^0 peak, are

$$\begin{aligned} \mathcal{A}_e &= 0.130 \pm 0.063 \pm 0.002 \ , \\ \mathcal{A}_\tau &= 0.162 \pm 0.052 \pm 0.014 \ , \end{aligned}$$

where the first error is statistical and the second systematic. From these measurements it can be inferred that the universality assumption in neutral currents holds well.

Under the universality assumption, the fit yields

$$\mathcal{A}_{e-\tau} = 0.148 \pm 0.035 \pm 0.009 \ .$$

The corresponding values for the electron and tau couplings are

$$\begin{aligned} \frac{g_V^e}{g_A^e} &= +0.065 \pm 0.032 \ , \\ \frac{g_V^\tau}{g_A^\tau} &= +0.082 \pm 0.027 \ , \\ \frac{g_V^{e-\tau}}{g_A^{e-\tau}} &= +0.074 \pm 0.018 \ . \end{aligned}$$

The value of $\sin^2\theta_W^{\rm eff}$ extracted from $\mathcal{A}_{e-\tau}$ is

$$\sin^2\theta_W^{\rm eff} = 0.2314 \pm 0.0046 \ .$$

These are the first measurements of correlated tau decay product distributions at LEP. It has been proved that this method measures some additional information relative to the single-tau method from the independent set of defined observables. This method is clearly not systematics limited, and its weight in the average with other tau polarization measurements from energy spectra, which will soon be systematics limited, is expected to become higher.

From the forward-backward asymmetry of the acollinearity distribution an additional test of the Standard Model is presented. Furthermore, this observable provides an alternative way to measure simultaneously the information of the forward-backward charge asymmetry and the forward-backward polarization asymmetry, thus allowing to take into account the correlation in a simple way.

Because of the correlation of the forward-backward asymmetry as a function of the acollinearity with the forward-backward charge asymmetry, another analysis is performed using the acollinearity distribution in the forward and backward hemispheres independently. These results are nearly uncorrelated with the forward backward charge asymmetry.

The values obtained are

$$\begin{aligned} \mathcal{A}_e &= 0.154 \pm 0.079 \pm 0.002 \ , \\ \mathcal{A}_\tau &= 0.147 \pm 0.056 \pm 0.011 \ , \\ \mathcal{A}_{e-\tau} &= 0.149 \pm 0.047 \pm 0.009. \end{aligned}$$

All these measurements are in good agreement with the Standard Model predictions and other experimental results.

Appendix A

Phase Space Integration in Q Functions

In chapter 2 the functions $F(\varepsilon)$ and $G(\varepsilon)$ were introduced as

$$F(\varepsilon) = Q_{11}(\varepsilon) + \alpha_1\alpha_2 Q_{22}(\varepsilon) \quad (A.1)$$

$$G(\varepsilon) = \alpha_1 Q_{21}(\varepsilon) + \alpha_2 Q_{12}(\varepsilon)\ , \quad (A.2)$$

where the subscripts 1 and 2 in the α coefficients refer to the analyzing power of the decays in the two hemispheres. For the Q_{ij} functions, the subscripts stands for the scalar(1) or spin-dependent(2) part of the decay distribution functions, which also depend on the combination of the two tau decay modes. The $F(\varepsilon)$ and $G(\varepsilon)$ functions have the following properties derived from 2.62

$$\int F(\varepsilon)\, d\varepsilon = 1 \quad (A.3)$$

$$\int G(\varepsilon)\, d\varepsilon = 0\ . \quad (A.4)$$

The functions $Q_{ij}(\varepsilon)$ are defined as in [25]

$$Q_{ij}(\varepsilon) \equiv 4\pi \sin\varepsilon \int \frac{E_1^* E_2^*}{Q}\, q_1\ q_2 dE_1 d\cos\theta_1 dE_2 d\cos\theta_2$$
$$A_i^1 \cdot (q_1^* \cos\theta_1^*)^{i-1} A_j^2 \cdot (q_2^* \cos\theta_2^*)^{j-1}\ . \quad (A.5)$$

The A_m^n are the "distribution functions" [7], where n refers to the decay mode and m refers to first or second term of the tau partial width for that decay mode, and q_i, θ_i and E_i are the momentum, direction and energy respectively of the τ

decay products in hemisphere i in the laboratory frame respectively. The label * refers to the quantities the τ rest frames.

This can be rewritten as

$$Q_{ij}(\varepsilon) = \frac{\sin\varepsilon}{4\pi}\int F_j(E_2,\cos\theta_2)dE_2 d\cos\theta_2 \int \frac{F_i(E_1,\cos\theta_1)}{Q}\, dE_1 d\cos\theta_1 \ , \quad \text{(A.6)}$$

where

$$F_j(E_2,\cos\theta_2) = 4\pi E_2^* q_2 A_j^{(2)} (q_2^*\cos\theta_2^*)^{j-1} \quad \text{(A.7)}$$

$$F_i(E_1,\cos\theta_1) = 4\pi E_1^* q_1 A_i^{(1)} (q_1^*\cos\theta_1^*)^{i-1} \ . \quad \text{(A.8)}$$

The description of the functions F_i is given as follows [13, 20]

Leptons

The functions A_m^n in equations A.7 and A.8 are given for leptons by

$$A_1^{(i)} = \frac{a_1^{(i)}}{4\pi\lambda_i E_i^*} = \frac{1}{4\pi\lambda_i E_i^*}\{v_0^{(i)} + v_1^{(i)} E_i^* + v_2^{(i)} E_i^{*2}\} \quad \text{(A.9)}$$

$$A_2^{(i)} = \frac{a_2^{(i)}}{4\pi\lambda_i E_i^*} = \frac{1}{4\pi\lambda_i E_i^*}\{b_0^{(i)} + b_1^{(i)} E_i^*\} \ . \quad \text{(A.10)}$$

Conserving the dependence with the Michel parameters, v_0, v_1,v_2, b_0 and b_1 are given by

$$v_0^{(i)} = -\frac{2}{9}\rho_i m_i^2 + \eta_i m_i W_i \qquad b_0^{(i)} = \frac{1}{3}(3-8\delta_i)\, W_i + \frac{2}{9}\delta_i P_i$$

$$v_1^{(i)} = (1-\frac{2}{3}\rho_i)\, W_i - \eta_i m_i \qquad b_1^{(i)} = \frac{1}{3}(8\delta_i - 3)$$

$$v_2^{(i)} = (\frac{8}{9}\rho_i - 1) \ . \quad \text{(A.11)}$$

In terms of the variables in the laboratory frame (using 2.52), the functions $F_j^{(l)}$ for the leptons are

$$F_1^{(l)}(E_i,\cos\theta_i) = \frac{q_i}{\lambda_i}\sum_{\mu=0}^{2} V_\mu^{(i)}\cos^\mu\theta_i \quad \text{(A.12)}$$

$$F_2^{(l)}(E_i,\cos\theta_i) = \frac{q_i}{\lambda_i}\sum_{\mu=0}^{2} B_\mu^{(i)}\cos^\mu\theta_i \ . \quad \text{(A.13)}$$

The $V_\mu^{(i)}$ and $B_\mu^{(i)}$ came from a rewritten version of $a_1^{(i)}$ and $a_2^{(i)}$, which when expressed in the laboratory frame takes the following form

$$a_1^{(i)} = V_0^{(i)} + V_1^{(i)} \cos\theta_i + V_2^{(i)} \cos^2\theta_i \ . \tag{A.14}$$

For the sake of simplicity $a_2^{(i)}$ is written in the following way

$$a_2^{(i)}(q_i^* \cos\theta_i^*) = B_0^{(i)} + B_1^{(i)} \cos\theta_i + B_2^{(i)} \cos^2\theta_i \ , \tag{A.15}$$

where

$$\begin{aligned} V_0^{(i)} &= v_0^{(i)} + v_1^{(i)}\gamma E_i + v_2^{(i)}\ (\gamma E_i)^2 \\ V_1^{(i)} &= -\beta\gamma q_i\ (v_1^{(i)} + 2v_2^{(i)}\gamma E_i) \\ V_2^{(i)} &= (\beta\gamma q_i)^2\ v_2^{(i)} \end{aligned} \tag{A.16}$$

$$\begin{aligned} B_0^{(i)} &= -\beta\gamma E_i\ (b_0^{(i)} + b_1^{(i)}\gamma E_i) \\ B_1^{(i)} &= \beta q_i\ [b_0^{(i)} + b_1^{(i)}\gamma E_i\ (1+\beta^2)] \\ B_2^{(i)} &= -\beta\ (\gamma q_i)^2\ b_1^{(i)} \ . \end{aligned}$$

Hadrons

The functions $F_j^{(m)}$ for mesons can be directly computed from equations 2.45 and 2.54

$$F_1^{(m)} = \frac{1}{\beta\gamma P_i} \tag{A.17}$$

$$F_2^{(m)}(E_i) = \frac{E_i - \gamma W_i}{(\beta\gamma P_i)^2} \ . \tag{A.18}$$

In order to perform these integrals for the cases where the correlated distributions are for either a lepton-lepton or a lepton-hadron, it is necessary to point out that when measuring the acollinearity as an observable it introduces a constraint among θ_1, θ_2 and the relative azimuthal angle that is given by the equation

$$\cos\varepsilon = \cos\theta_1 \cos\theta_2 - \sin\theta_1 \sin\theta_2 \cos\phi \ . \tag{A.19}$$

The allowed region in (θ_1, θ_2)-space is a rectangle as defined by equation A.19. At the same time this rectangle defines an allowed region in (E_1, E_2)-space where

the integration over θ_1, θ_2 is constrained to its interior. The specified area for the (E_1, E_2)-space depends on the decay channel, to be either a lepton or a hadron. In the cases of the hadrons, they are emitted with an energy E, so the angle of emission θ is fixed then and denoted as ζ, as defined in equation 2.54. For this reason the defined area will consists of a rectangle for the lepton-lepton case, whereas for the lepton-hadron will be reduced to a line and for the hadron-hadron to a single point in the (E_1, E_2)-space. Figure A.1 illustrates the constraints from equation A.19 and the maxima angle emissions.

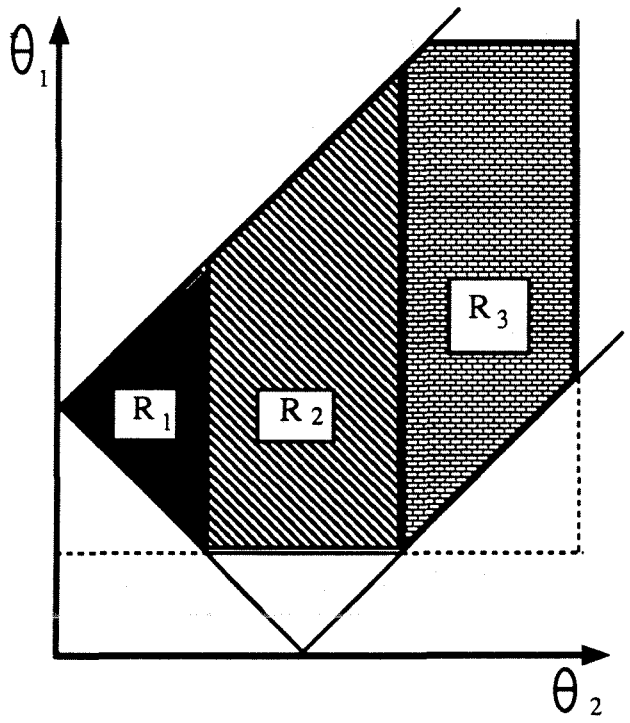

Figure A.1: *Allowed angular region for a given acollinearity angle.*

Figure A.1 shows also the three regions that can be defined for convenience in order to perform the integration over θ_1 angle when the most general case, the lepton-lepton, is presented. The different limits of integration for every region in the lepton-lepton case are given in table A. In this table, the lepton-hadron case can be obtained too, just by fixing $\theta_2 = \zeta_2$ for the hadron.

From equations A.6, A.12 and A.13 it can be seen that the general form of those

R_i	$\cos\theta_2$ region	$\Gamma_1(\theta_2)$	$\Gamma_2(\theta_2)$
R_3	$-1 \leq \cos\theta_2 \leq \cos(\varepsilon+\zeta_1)$	$\cos(\varepsilon+\theta_2)$	$\cos(\varepsilon-\theta_2)$
R_2	$\cos(\varepsilon+\zeta_1) \leq \cos\theta_2 \leq \cos(\varepsilon-\zeta_1)$	$\cos\zeta_1$	$\cos(\varepsilon-\theta_2)$
R_1	$\cos(\varepsilon-\zeta_1) \leq \cos\theta_2 \leq 1$	$\cos(\varepsilon+\theta_2)$	$\cos(\varepsilon-\theta_2)$

Table A.1: Limits of integration for $\cos\theta_1$.

integrals is

$$K_\mu(\theta_2) = \int_{\Gamma_1(\theta_2)}^{\Gamma_2(\theta_2)} \frac{\cos^\mu\theta_1}{Q} \qquad \mu = 0,1,2 \tag{A.20}$$

In the regions R_1 y R_3 the following integral are obtained

$$K_0(\theta_2) = \pi \tag{A.21}$$

$$K_1(\theta_2) = \pi\cos\theta_2\cos\varepsilon \tag{A.22}$$

$$K_2(\theta_2) = \frac{\pi}{2}[(3\cos^2\varepsilon-1)\cos^2\theta_2+\sin^2\varepsilon]\,. \tag{A.23}$$

Whereas the results for the R_2 region are

$$K_0(\theta_2) = \frac{\pi}{2} - X(\theta_2) \tag{A.24}$$

$$K_1(\theta_2) = W(\theta_2) + \cos\theta_2\cos\varepsilon\left[\frac{\pi}{2} - X(\theta_2)\right] \tag{A.25}$$

$$\begin{aligned} K_2(\theta_2) &= \frac{1}{2}(\cos\zeta_1 + 3\cos\theta_2\cos\varepsilon)W(\theta_2) \\ &+ \frac{1}{2}[(3\cos^2\varepsilon-1)\cos^2\theta_2+\sin^2\varepsilon]\left[\frac{\pi}{2} - X(\theta_2)\right]\,, \end{aligned} \tag{A.26}$$

with

$$X(\theta_2) = \arcsin\frac{\cos\zeta_1 - \cos\theta_2\cos\varepsilon}{\sin\theta_2\sin\varepsilon} \tag{A.27}$$

$$W(\theta_2) = \sqrt{\sin^2\zeta_1\sin^2\theta_2 - (\cos\varepsilon - \cos\theta_2\cos\zeta_1)^2}\,. \tag{A.28}$$

For the case of lepton-hadron the functions $K_\mu(\theta_2 = \zeta_2)$ must be evaluated. The integration over the energies of both particles, in the case of lepton-hadron, and

over both energies and the second angle of emission, in the lepton-lepton case, have been done numerically.

Finally, for the hadron-hadron case the angles of emission θ_i are determined by equation 2.54 when the energy E_i is fixed. Then, only the integration over E_1 and E_2 is required. From equation 2.54, the two possible solutions for the energy for every angle of emission θ_i can be derived, and are given by the following equation

$$E_i^{\pm} = \frac{m_i}{\gamma\,[1-(\beta\cos\theta_i)^2]}\left\{\gamma_i^* \pm \gamma\beta^2\cos\theta_i\sqrt{\frac{P_i^2}{(m_i\gamma\beta)^2}-\sin^2\theta_i}\right\}. \quad \text{(A.29)}$$

The limits of the integration over E_1 depend on E_2. The approach described in figure A.1 can be followed to integrated out E_1, where the limits of integration are given by equation A.29 when substituting $\theta_1 = |\theta_2 - \varepsilon|$ and $\theta_1 = (\theta_2 + \varepsilon)$. The integrations over E_1 and E_2 have also been done numerically.

Appendix B

Covariance Matrix for the Forward-Backward Asymmetry

The forward and backward acollinearity distributions are similarly corrected, as described in equation 5.8, according to:

$$N_i^{cor\ F} = C_i^{rad\ F} \frac{1}{\eta_i} \sum_j A_{ij} N_j^{obs\ F} (1 - B_j) \tag{B.1}$$

$$N_i^{cor\ B} = C_i^{rad\ B} \frac{1}{\eta_i} \sum_j A_{ij} N_j^{obs\ B} (1 - B_j)\ . \tag{B.2}$$

From equations B.1 and B.2, the covariance submatrix is derived for the forward and backward hemispheres, C_{ij}^F and C_{ij}^B, respectively given by

$$C_{ij}^F = A_{ik}\ E_{km}^F\ A_{mj}^T \tag{B.3}$$

$$C_{ij}^B = A_{ik}\ E_{km}^B\ A_{mj}^T\ , \tag{B.4}$$

where the matrix A_{ij} is the resolution matrix introduced in equation 5.8, E_{km}^F and E_{km}^B are the error matrixes which contains the statistical error for the forward and backward acollinearity distributions. Then, the matrix $C_{N_{ij}}$ is constructed as

$$C_{N_{ij}} = \begin{pmatrix} C_{ij}^F & 0 \\ 0 & C_{ij}^B \end{pmatrix}\ , \tag{B.5}$$

assuming that the forward and backward hemispheres do not have any correlation. This matrix will play the role of the error matrix for the next transformation.

The forward-backward asymmetry is given in a bin i of acollinearity by

$$A_{FB_i}(\varepsilon) = \frac{N_i^F - N_i^B}{N_i^F + N_i^B} , \tag{B.6}$$

where N_i^F and N_i^B is the corrected number of events in this bin i for the forward and backward acollinearity distributions, respectively.

So, the matrix T'_{ij} that contains the propagation of the errors due to the transformation expressed in equation B.6 is defined as

$$T'_{ij} = \frac{\partial A_{FBi}}{\partial N_j} , \tag{B.7}$$

where N_j is identified to $N_1^F, \cdots, N_i^F, N_1^B, \cdots, N_i^B$ according to the j index.

Finally, the covariance matrix $C_{A_{FB}}$ for the least square fit for the asymmetry is given by [79]

$$C_{A_{FB}} = T' \, C_N \, T'^{\,T} . \tag{B.8}$$

Bibliography

[1] D. Decamp *et al.* ALEPH Collaboration, *Zeit. fur Physik* **C53** (1992) 1;
P. Abreu *et al.* DELPHI Collaboration, *Nucl. Phys.* **B367** (1991) 511;
B. Adeva *et al.* L3 Collaboration, *Zeit. fur Physik* **C51** (1991) 179;
G. Alexander *et al.* OPAL Collaboration, *Zeit. fur Physik* **C52** (1992) 175.

[2] H.J. Behrend *et al.*, CELLO Collaboration, *Phys. Lett.* **B127** (1983) 270;
W.T. Ford *et al.*, MAC Collaboration, *Phys. Rev.* **D36** (1987) 1971;
M.H. Lee *et al.*, AMY Collaboration, KEK Preprint 90-70 (1990).

[3] P. Abreu *et al.* DELPHI Collaboration, *Zeit. fur Physik* **C55** (1992) 555;
O. Adriani *et al.* L3 Collaboration, *Phys. Lett.* **B249** (1992) 466;
G. Alexander *et al.* OPAL Collaboration, *Phys. Lett.* **B266** (1991) 201.

[4] The LEP Collaborations: ALEPH, DELPHI, L3 and OPAL. *Phys. Lett.* **B276** (1992) 247.

[5] "Z Physics at LEP 1", CERN 89-08, eds. G. Altarelli, R. Kleiss and C. Verzegnassi.

[6] S.Y. Pi and A.I. Sanda, *Ann. Phys. (NY)* **106** (1977) 171;
H. Kühn and F. Wagner, *Nucl. Phys.* **B236** (1984) 16;
J. E Augustin, ECFA/LEP report 29, CERN 79-01 (1979) 499.

[7] Y.S. Tsai, *Phys. Rev.* **D4** (1971) 2821;
S. Kawasaki, T. Shirafuji and Y.S. Tsai, *Prog. Theor. Phys.* **49** (1973) 1656.

[8] A. Rougé, *Zeit. fur Physik* **C48** (1990) 75;
A. Rougé, "Proceedings of the Workshop on Tau Lepton Physics", eds. M. Davier and B. Jean-Marie, Ed. Frontières, 1991.

[9] K. Hagiwara, A.D. Martin and D. Zeppenfeld, *Phys. Lett.* **B235** (1990) 198.

[10] M. Davier, L. Duflot, F. Le Diberder and A. Rougé, "The optimal method for the measurement of tau polarisation". Preprint LAL 92-73 or X-LPNHE 92-22.

[11] J. Bernabéu, A. Pich and N. Rius, *Phys. Lett.* **B257** (1991) 219.

[12] C.A. Nelson, *Phys. Rev.* **D43** (1991) 1465.

[13] N. Rius, "Análisis de la polarización del tau y correlaciones de espín a las energías de LEP", Ph.D. Tesis, Univ. Valencia (1991).

[14] C.A. Nelson, *Phys. Rev.* **D40** (1989) 123.

[15] M. Consoli, W. Hollik and F. Jegerlehner, "Z Physics at LEP 1", CERN 89-08, eds. G. Altarelli, R. Kleiss and C. Verzegnassi, Vol. 1, p. 7.

[16] J. Bernabéu and N. Rius, *Phys. Lett.* **B232** (1989) 127.

[17] T. Hagiwara, S.Y. Pi, A.I. Sanda, *Ann. Phys. (NY)* **106** (1977) 134.

[18] J. Babson and E. Ma, *Zeit. fur Physik* **C20** (1983) 5.

[19] J.J. Gómez-Cadenas, Proceedings of the Tau-Charm Factory Workshop, SLAC-Report 343 (1989).

[20] W. Fetscher, *Phys. Rev.* **D42** (1990) 1544.

[21] A. Pich, "Tau Physics", Heavy flavours, eds. A.J. Buras and M. Lindner. Advanced Series on Directions in High Energy Physics. World Scientific, 1991.

[22] Particle Data Group, "Review of Particle Properties", *Phys. Rev.* **D45** (1992) .

[23] S. Kawasaki, T. Shirafuji and Y.S. Tsai, *Prog. Theor. Phys.* **49** (1973) 1656.

[24] S.Y. Pi, A.I. Sanda, *Ann. Phys. (NY)* **106** (1977) 171.

[25] R. Alemany, N. Rius, J. Bernabéu, J.J. Gómez-Cadenas, A. Pich, *Nucl. Phys.* **B379** (1992) 3.

[26] S. Jadach and Z. Was, "Z Physics at LEP 1", CERN 89-08, eds. G. Altarelli, R. Kleiss and C. Verzegnassi, Vol. 1, p. 235.

[27] "LEP Design Report", CERN-LEP/84-01 (1984).

[28] D. Decamp *et al.*, ALEPH Collaboration, "A Detector for Electron-Positron Anihilations at LEP", *Nucl. Inst. and Meth.* **A294** (1990) 121.

[29] D. Decamp *et al.*, ALEPH Collaboration, "The ALEPH Handbook", ALEPH internal report, ALEPH 89-77, NOTE 89-03 (1989).

[30] G.J. Barber *et al.*, "Performance of the Three-Dimensional Readout of the ALEPH Inner Tracking Chamber", *Nucl. Inst. and Meth.* **A279** (1989) 212.

[31] P. Némethy *et al.*, "Gated Time Projection Chamber", *Nucl. Inst. and Meth.* **A297** (1983) 273.

[32] S.R. Amendolia *et al.*, "Influence of the magnetic field on the gating of a time projection chamber", *Nucl. Inst. and Meth.* **A234** (1985) 47.

[33] W. Witzeling *et al.*, "dE/dx - Recent Results from TPC", Contribution to the V. Internat. Conference on Colliding Beam Detector, Novosibirsk (1990).

[34] S.R. Amendolia *et al.*, "The spatial resolution of the ALEPH TPC", *Nucl. Inst. and Meth.* **A283** (1989) 573.

[35] W.B. Atwood *et al.*, "Performance of the ALEPH Time Projection Chamber", *Nucl. Inst. and Meth.* **A306** (1991) 446.

[36] G. Batignani *et al.*, "The ALEPH Silicon Vertex Detector", *Nucl. Phys.* **23A** (1991) 291 (B Proc. Suppl).

[37] H. Videau, "The ALEPH Pictorial Electromagnetic Calorimeter - A High Granularity Gaseous Calorimeter Operated in a High Magnetic Field", Invited talk at the 2nd Pisa Meeting on advanced detectors, Castiglione, Italy, June 1983.

[38] G. Bagliesi *et al.*, "The combined response of the ALEPH electromagnetic and hadronic calorimeter to pions", *Nucl. Inst. and Meth.* **A286** (1990) 61.

[39] R. Baldini *et al.*, "Performance of a Limited Streamer Tube Hadron Calorimeter", *Nucl. Inst. and Meth.* **A247** (1986) 438.

[40] G. Bagliesi *et al.*, "Operation of limited streamer tubes with the gas misture Ar + CO2 + n-pentane", *Nucl. Inst. and Meth.* **A268** (1988) 144.

[41] D. Decamp *et al.*, ALEPH Collaboration" A proposal for a low-angle solid-state luminosity calorimeter for ALEPH: SICAL ", CERN/LEPC/90-3.

[42] M. Martínez and H. Meinhard, Status of 1992 electroweak results. ALEPH 93-56.

[43] E. Fernández *et al.*, "A Very Forward Luminosity Monitor for the ALEPH Detector at LEP", *Nucl. Inst. and Meth.* **A297** (1990) 153.

[44] A. Belk *et al.*, "DAQ software architecture for ALEPH, a large HEP experiment", *IEEE Trans. Nucl. Sci.* NS-36 (1989) 1534.

[45] W. von Ruden, "The ALEPH data adquisition system", *IEEE Trans. Nucl. Sci.* NS-36 (1989) 1444.

[46] P. Mató, "Data Processing for Large e^+e^- Experiments", Ph. D. Thesis, Universitat de Barcelona (1990).

[47] B. Jost *et al.*, "A Multi-Function FASTBUS Front-End for VAXBI computers", *IEEE Trans. Nucl. Sci.* NS-36 (1989) 1452.

[48] K. Einsweiler *et al.*, "The ALEPH Event Builder. A Multi-User Fastbus Master", *IEEE Trans. Nucl. Sci.* NS-35 (1988) 316.

[49] M. Delfino *et al.*, "The ALEPH Event Reconstruction Facility: Parallel Processing using Workstations", *Comp. Phys. Comm.* **57** (1989) 401.

[50] GALEPH, ALEPH internal report, ALEPH 86-119 (1986).

[51] S. Jadach *et al.*, "Z Physics at LEP I", CERN Report CERN-89-08, Vol.3 (1989) 69.

[52] B. Bloch-Devaux *et al.*, " KINGAL User's Guide", ALEPH internal report ALEPH 87-53, SOFTWR 87-7 (1988).

[53] M. Böhm *et al.*, "Radiative Corrections to Bhabha Scattering at High Energies I. Virtual and Soft Photon Corrections", *Nucl. Phys.* **B304** (1988) 687.

[54] F.A. Berends *et al.*, " Radiative Corrections to Bhabha Scattering at High Energies II. Hard Photon Corrections and Monte Carlo Treatment", *Nucl. Phys.* **B304** (1988) 712.

[55] T. Sjostrand, "The Lund Monte Carlo for Jet Fragmentation and e^+e^- Physics", LU TP 85-10.

[56] F.A. Berends *et al.*, "Total and Visible Cross Sections for Multilepton Events in e^+e^- collisions", *Phys. Lett.* **B148** (1984) 489.

[57] F.A. Berends *et al.*, "Radiative Corrections to the Process $e^+e^- \to e^+e^-\mu^+\mu^-$", *Nucl. Phys.* **B253** (1985) 421.

[58] R. Brun *et al.*, "GEANT3 User's Guide", CERN DD/EE/84-1 (1987).

[59] H. Fesefeldt, "GHEISHA", Aachen 3rd Inst.

[60] W. Wiedenmann, "Alignment of the ALEPH tracking devices", CERN-PPE/92-90.

[61] W. Wiedenmann, "Tracking with the ALEPH Time Projection Chamber", Paper presented at the *IEEE Nucl. Sci. Symp.*, Arlington, VA, (1990).

[62] J. Knobloch and P. Norton, "Status of Reconstruction Algorithms for ALEPH. Version 3", ALEPH internal report, ALEPH 91, (1991).

[63] D. Decamp *et al.* ALEPH Collaboration, *Zeit. fur Physik* **C48** (1990) 365.

[64] H. Videau, private communication. February, 1992.

[65] B. Humpert, *Comp. Phys. Comm.* **56**(1990) 299.

[66] L. Lonnblad *et al.*, "Pattern recognition in high energy physics with artificial neural networks- JETNET 2.0", Lund University Report LU-TP 91-18.

[67] J. Conway *et al.*, "Particle identification for tau physics in ALEPH using a Neural Network", ALEPH 92-56, (1992).

[68] J. Conway *et al.*, "Improved Neural Network for particle identification in tau physics in ALEPH ", ALEPH 92-111, (1992).

[69] A. Rougé *et al.*, "GAMPEK algorithm ", ALEPH note, in preparation.

[70] E. Blucher *et al.*, ALPHA user's guide, ALEPH 93-1, (1992).

[71] D. Decamp *et al.* ALEPH Collaboration, *Phys. Lett.* **B265** (1991) 430.

[72] S.Jadach, 3.F.L. Ward, and Z. Was, "The Monte-Carlo program KORALZ, version 3.8, for the lepton or quark pair production at LEP/SLC energies", CERN preprint, CERN TH-5994/91.

[73] D. Buskulic *et al.* ALEPH Collaboration, CERN-PPE/93-40 (March 1993).

[74] ASYM program. Courtesy of M. Martínez (1992).

[75] D. Decamp *et al.* ALEPH Collaboration, *Zeit. fur Physik* **C54** (1992) 211.

[76] L. Lyons *et al.*, "How to Combine Correlated Estimators of a Single Physical Quantity", *Nucl. Inst. and Meth.* **A270** (1988) 110.

[77] D. Buskulic *et al.* ALEPH Collaboration, CERN-PPE/93-39 (March 1993). Submitted to Zeitsch. für Physik C.

[78] L. A. Ahrens *et al.*, *Phys. Rev.* **D41** (1990) 3291;
D. Geiregat *et al.*, (CHARM-II Collaboration), *Phys. Lett.* **B259** (1991) 499;
R. C. Allen *et al.*, Phys. Rev. Lett. **55** 2401 (1985);
H.-J. Behrend *et al.*, (CELLO Collaboration),
Zeit. fur Physik **C16** (1983) 301.

[79] W.T. Eadie *et al.*, "Statistical Methods in Experimental Physics", Ed. North-Holland (1982).